Title
The Rise and Fall of Stellar Disks in Massive Galaxies

Author
Davari, Roozbeh

Publication Date
2015

UNIVERSITY OF CALIFORNIA
RIVERSIDE

Tracing the Formation and Evolution of Massive Elliptical Galaxies

A Dissertation submitted in partial satisfaction
of the requirements for the degree of

Doctor of Philosophy

in

Physics

by

Roozbeh Davari

December 2015

Dissertation Committee:
Dr. Gabriela Canalizo, Chairperson
Dr. Luis Ho
Dr. Bahram Mobasher

The Dissertation of Roozbeh Davari is approved:

Committee Chairperson

University of California, Riverside

Acknowledgements

I am grateful to everyone who made this Ph.D. dissertation possible. A complete list of people who played an essential role in the process is not feasible, however, a few people immediately come to mind.

I would like to thank Prof. Luis Ho, the best mentor I could have asked for. Luis's intelligence, hard work, and unique perspective never ceased to inspire me to do my best and be a better scientist. I am very grateful to my graduate advisor, Prof. Gabriela Canalizo, who made sure I am making sensible decisions. Gaby was alway available to help me with anything that needed to be done. She also encouraged me to apply for different awards, which were extremely beneficial.

I thank my dear wife, Heather, for lovingly supporting me through all the years of my dissertation research. She has been very understanding, flexible, and encouraging through the intense periods of work, including numerous hours spent editing my thesis. I thank my soon-to-be-born daughter for providing me with extra motivation and brightening the final months of my research. Without the support and encouragement of my family in Iran, especially my father, I would not have been able to pursue an advanced degree.

Additionally, I deeply thank my Iranian friends at UCR who were there for me when I moved to US and helped me to get settled. The same goes to my ECK community which are like my extended family. Last but not the least, I thank Dr. Derek Beving, UCR Physics Department Student Academic Affairs, for being alway generous with his time and resources.

I received funding by a graduate student fellowship awarded by Carnegie Observatories. A special thank you to Wendy Freedman for her support.

The text of this dissertation, in part, is a reprint of the material as it appears in a journal article entitled *How Robust are the Size Measurements of High-redshift Compact Galaxies?*, which appeared in volume 787 (page 69) of The Astrophysical Journal, May 5th, 2014. The co-author (Luis C. Ho) listed in that publication directed and supervised the research which forms the basis for this dissertation.

ABSTRACT OF THE DISSERTATION

Tracing the Formation and Evolution of Massive Elliptical Galaxies

by

Roozbeh Davari

Doctor of Philosophy, Graduate Program in Physics
University of California, Riverside, December 2015
Dr. Gabriela Canalizo, Chairperson

Massive galaxies at higher redshift, $z > 2$, show different characteristics than their local counterparts. They are compact and most likely have a disk. Understanding the evolutionary path of these massive galaxies can give us some clues on how the universe has been behaving in the last 10 billion years. How well can we measure the bulge and disk properties of these systems? We perform two sets of comprehensive simulations in order to systematically quantify the effects of non-homology in structures and the methods employed.

For the first set of simulations, by accurately capturing the detailed substructures of nearby elliptical galaxies and then rescaling their sizes and signal-to-noise to mimic galaxies at different redshifts, we confirm that the massive quiescent galaxies at $z \approx 2$ are significantly more compact intrinsically than their local counterparts. Their observed compactness is not a result of missing faint outer light due to systematic errors in modeling.

For the second set of simulations, we employ empirical scaling relations to produce realistic-looking two-component local galaxies with a uniform and wide range of bulge-to-total ratios (B/T), and then rescale them to mimic the signal-to-noise ratios and sizes of observed galaxies at $z \approx 2$. This provides the first set of simulations for which we can examine the robustness of two-component decomposition of compact disk galaxies at different B/T. We can measure

B/T accurately without imposing any constraints on the light profile shape of the bulge, but, due to the small angular sizes of bulges at high redshift, their detailed properties can only be recovered for galaxies with $B/T \gtrsim 0.2$. The disk component, by contrast, can be measured with little difficulty.

Next, we trace back the evolution of local massive galaxies but performing detailed morphological analysis: namely, single Sérsic fitting and bulge+disk decomposition. CANDELS images and catalogues offer an ideal dataset for this study. We analyze about 250 massive galaxies selected from all available CANDELS fields (COSMOS, UDS, EGS, GOODS-South and GOODS-North). We confirm that both star-forming and quiescent galaxies have increased their sizes significantly between $0 < z < 2.5$. The Sérsic index of quiescent galaxies have increased over time (from $n \approx 2.5$ to $n > 4$) while for star-forming galaxies, it stays almost the intact ($n \approx 2.5$). The quiescent galaxie have become rounder. The bulge+disk decompositions reveal that massive galaxies at higher redshift are more disk dominated and by $z \approx 0.5$, massive quiescent galaxies begin to resemble local elliptical galaxies. Star-forming galaxies have lower B/T at each redshift bin and their fraction decreases at lower redshifts. Bulges of star-forming and quiescent galaxies follow different evolutionary trajectories, while their disks evolve similarly. I show that major mergers, along with minor mergers, have played a crucial role in the significant size increase of high-z galaxies and the destruction of their massive and large-scale disks.

Contents

List of Figures

List of Tables

Chapter 1

Introduction

Galaxy morphology has always been an important observable for understanding the formation and evolution of galaxies. Recent imaging studies using the *Hubble Space Telescope (HST)*/Wide Field Camera 3 (WFC3) and Advanced Camera for Surveys (ACS) have broadened our understanding of the formation and evolution of galaxies. The advent of WFC3 has given access to the rest-frame optical light of galaxies at $z \approx 2$. Morphological studies of these galaxies show that quiescent systems make up a high fraction of the massive galaxy population at $z \approx 2$. Their structural evolution has been the subject of considerable interest, focusing in particular on their extremely compact nature compared to low-z galaxies of similar mass. The sizes of these "red nuggets," less than ~ 1 kpc, seem comparable to and sometimes even smaller than the point-spread function (PSF). The early formation and subsequent size growth of these massive, compact objects present a challenge to current models of galaxy formation and evolution. It is not clear via what pathways they become the massive galaxies of today. The rarity of these massive, compact galaxies at low redshift implies considerable size evolution between $z = 2$ and $z = 0$. On average, from $z \approx 2$, these objects would have to increase their size by 3–5 times while doubling their stellar mass. However, efforts to accurately quantify this evolution are hindered by potential uncertainties in measurement techniques: the mass densities may simply be systematically overestimated due to modeling uncertainties of photometric masses, and/or the sizes may be underestimated due to a lack of imaging depth or other measurement issues.

In addition to the basic question of how these high-z galaxies evolve in size, there is also still much debate about how these systems evolve in terms of their fundamental morphological type. Number of studies have revealed the presence of the disk in these high redshift massive galaxies. This may come as a surprise as at the local universe, almost all the massive galaxies are ellipticals. But considering the fact that at the early universe the gas content of the galaxies were higher and therefore gas rich mergers were more common, it is plausible to observe rotationally supported massive galaxies at those redshift. Therefore, besides the observational evidence, tracing back the formation history of local massive ellipticals can give us a clue on why the red, massive, compact galaxies, the so-called "red nuggets", at $z \approx 2$ may commonly have a disk component.

Many factors complicate the image analysis of galaxies, including determination of the sky background, the brightness of the galaxy [signal-to-noise ratio (S/N)], the resolution of the images, $(1+z)^4$ surface brightness dimming, finding the best PSF, the method employed for modeling the galaxy, and the potential biases of the fitting pipeline. Galaxy simulations are invaluable tools for understanding the performance of quantitative fitting pipelines because they provide control over the aforementioned factors.

We devise simulations with increasing realism to systematically disentangle effects due to the technique (specifically using `GALFIT`) and the intrinsic structures of the galaxies. We aim at answering the following key questions:

1) Do the quiescent massive galaxies at $z = 2$ have sizes comparable with the quiescent massive local galaxies and therefore their observed compactness is not intrinsic but an artifact of inappropriate and insufficient morphological modeling?

2) How well can single-component fitting of bulge+disk galaxies measure the global size and total luminosity of these galaxies?

3) What are the true uncertainties of the size and total luminosity measurements, using single Sérsic fitting, at different S/N levels due to structural complexities?

4) Can we recover the properties of both the bulge and disk components, and if so, how well?

5) What are the best methods for measuring the B/T of composite galaxies? And what are the potential biases of different bulge-disk fitting methods?

We do so by performing three types of detailed simulations. Model galaxies with a single Sérsic component with parameter ranges that cover the *HST*/WFC3 observations of the red nuggets are the first set of simulations we perform. These idealized simulations can determine the robustness of fitting pipelines at different noise levels. Therefore, the uncertainties and systematic errors measured from these simulated galaxies can be considered as lower limits. More informative analysis is done by simulating multi-component galaxies with the properties obtained from Huang et al. 2013. By artificially scaling modern-day galaxies to sizes and luminosities comparable to those found in galaxies at $z \approx 2$, we can fit them with single-component Sérsic models to understand the systematics caused by complexities in galaxy structures. The differences between the input and output parameters shed light on possible uncertainties and biases in size and total luminosity measurements of the high-z galaxies. Finally, we simulate two-component model galaxies in order to systematically quantify the effects of non-homology in structures and the methods employed. We employ empirical scaling relations to produce realistic-looking local galaxies with a uniform and wide range of bulge-to-total ratios (B/T), and then rescale them to mimic the signal-to-noise ratios and sizes of observed galaxies at $z \approx 2$. This provides the first set of simulations for which we can examine the robustness of two-component decomposition of compact disk galaxies at different B/T.

Now the question remains: how have these red, compact, massive, and most likely disk-dominated galaxies at $z \approx 2$ have turn into local ginats like M87? We aim at tracing this morphological transition and fill in the blank. We do so by reliable 2D modeling of the light distributions of massive galaxies between $0.5 < z < 2.5$. Besides performing simple single Sérsic fitting, bulge+disk decomposition of these massive galaxies is executed, when possible. Examining the bulge and disk properties, plus the luminosity bulge-to-total ratio (B/T), provides key indicators that can be missed out by by studying a bulge+disk galaxy as a single system.

The Cosmic Assembly Near-infrared Deep Extragalactic Legacy Survey (CANDELS), one of the largest project in the history of Hubble, have provided an unprecedented chance of this type of morphological evolution studies. We take advantage of all wide and deep images taken in the infamous five widely separated fields; GOODS-South & GOODS-North, UDS, COSMOS, and EGS. This yields a statistically uniform and robust sample which furthermore mitigates the cosmic variance.

Using these measurement address three key questions:

1) How does the size and the shape of light distribution (Sérsic index) of star-forming and quiescent massive galaxies evolve?

2) Do the high redshift massive galaxies have a disk component? If yes, how significant is their B/T evolution in the last 10 billion years?

3) What can we learned from the evolution of bulges and disks about the evolutionary passage of massive galaxies?

Our findings show that the massive galaxies were compact and indeed more disk-dominated at higher redshifts and became more bulge-dominated over time. Their local counterparts, massive elliptical galaxies, don't have a large-scale disk. Therefore, major mergers, besides the minor mergers, have played an important role in the significant size increase of high-z galaxies and the destruction of their massive and large-scale disks.

Chapter 2

How Robust Are the Size Measurements of High-redshift Compact Galaxies?

Abstract

Massive quiescent galaxies at $z \approx 2$ are apparently much more compact than galaxies of comparable mass today. How robust are these size measurements? We perform comprehensive simulations to determine possible biases and uncertainties in fitting single-component light distributions to real galaxies. In particular, we examine the robustness of the measurements of the luminosity, size, and other structural parameters. We devise simulations with increasing realism to systematically disentangle effects due to the technique (specifically using `GALFIT`) and the intrinsic structures of the galaxies. By accurately capturing the detailed substructures of nearby elliptical galaxies and then rescaling their sizes and signal-to-noise to mimic galaxies at different redshifts, we confirm that the massive quiescent galaxies at $z \approx 2$ are significantly more compact intrinsically than their local counterparts. Their observed compactness is not a result of missing faint outer light due to systematic errors in modeling. In fact, we find that fitting multi-component galaxies with a single Sérsic profile, the procedure most commonly

adopted in the literature, biases the inferred sizes higher by up to 10%–20%, which accentuates the amount of size evolution required. If the sky estimation has been done robustly and the model for the point-spread function is fairly accurate, `GALFIT` can retrieve the properties of single-component galaxies over a wide range of signal-to-noise ratios without introducing any systematic errors.

2.1 Introduction

Galaxy morphology has always been an important observable for understanding the formation and evolution of galaxies. Recent imaging studies using the *Hubble Space Telescope (HST)*/Wide Field Camera 3 (WFC3) and Advanced Camera for Surveys (ACS) have broadened our understanding of the formation and evolution of galaxies. The advent of WFC3 has given access to the rest-frame optical light of galaxies at $z \approx 2$. Morphological studies of these galaxies show that quiescent systems make up a considerable fraction of the massive galaxy population at $z \approx 2$ (e.g., Franx et al. 2003; Daddi et al. 2005; Kriek et al. 2006). Their structural evolution has been the subject of considerable interest, focusing in particular on their extremely compact nature compared to low-redshift galaxies of similar mass (e.g., Daddi et al. 2005; Toft et al. 2007; Trujillo et al. 2007; Buitrago et al. 2008; Cimatti et al. 2008; Franx et al. 2008; van der Wel et al. 2008; van Dokkum et al. 2008; Damjanov et al. 2009; Hopkins et al. 2009; Cassata et al. 2010, 2011; Mancini et al. 2010; Newman et al. 2012; Szomoru et al. 2012). The sizes of these "red nuggets," less than ~ 1 kpc, seem comparable to and sometimes even smaller than the point-spread function (PSF). The early formation and subsequent size growth of these massive, compact objects present a challenge to current models of galaxy formation and evolution (e.g., Wuyts et al. 2010; Oser et al. 2012). It is not clear via what pathways they become the massive galaxies of today. The rarity of these massive, compact galaxies at low redshift implies considerable size evolution between $z = 2$ and $z = 0$ (van Dokkum et al. 2008; Trujillo et al. 2009; Taylor et al. 2010; but see Saracco et al. 2010; Valentinuzzi et al. 2010; Poggianti et al. 2013). On average, from $z \approx 2$, these objects would have to increase their size by 3–4 times while doubling their stellar mass (van Dokkum & Brammer 2010; see also Ichikawa et al. 2012). However, efforts to accurately quantify this evolution are hindered by potential uncertainties in measurement techniques: the mass densities may simply be systematically overestimated due to modeling uncertainties of photometric masses, and/or the sizes may be underestimated due to a lack of imaging depth or other measurement issues (Hopkins et al. 2009; Muzzin et al. 2009).

In addition to the basic question of how these high-z galaxies evolve in size, there is also still much debate about how these systems evolve in terms of their fundamental morphological type. By performing `GALFIT` fitting on a sample of 14 compact, massive galaxies at $z = 2$, van der Wel et al. (2011) find that a significant subset of their sample appears highly flattened in projection, which, considering viewing angle statistics, implies those galaxies have pronounced disks. They claim that 65%±15% of the population of massive quiescent at $z > 2$ galaxies are disk-dominated. Bruce et al. (2012) find that a considerable fraction (25%±6% using a definition of bulge-to-total ratio $B/T < 0.5$ and 40%±7% using a definition of $n < 2.5$ for disk-dominated) of the most quiescent galaxies, with specific star formation rates $< 10^{-10}$ yr^{-1}, have disk-dominated morphologies, including a small number of essentially pure disk galaxies (with $B/T < 0.1$). They claim that these passive disks appear to be normal disks in the sense that they show an axial-ratio distribution comparable to that displayed by present-day disks. This implies that while the massive galaxy population is undergoing dramatic changes at this crucial epoch, the physical mechanisms that quench star formation activity are not obviously connected to those responsible for transforming the morphologies of massive $z \approx 2$ galaxies into present-day giant ellipticals.

A recent morphological study of nearby elliptical galaxies has opened a new window to understanding the formation and assembly of early-type galaxies. Huang et al. (2013a, hereafter H13) present a detailed, comprehensive structural analysis of about 100 representative, nearby elliptical galaxies spanning a range of environments and stellar masses ($M_* \approx 10^{10.2} - 10^{12.4}$ $M_\odot$). They use `GALFIT 3.0` (Peng et al. 2002, 2010) to perform two-dimensional, multi-component decomposition of relatively deep, moderately high-resolution V-band images acquired as a part of the Carnegie-Irvine Galaxy Survey[1] (CGS; Ho et al. 2011). H13 challenge the conventional notion that the main body of giant ellipticals follows a single structure described by a high Sérsic (1968) index (e.g., $n \geq 3-4$). They propose that the global light distribution of the majority (>75%) of ellipticals are best described by three Sérsic components: a compact, inner core with typical effective radius $R_e < 1$ kpc and luminosity fraction $f \approx 0.1-0.15$; an intermediate-scale, middle component with $R_e \approx 2.5$ kpc and $f \approx 0.2-0.25$; and an extended, outer envelope with $R_e \approx 10$ kpc and $f \approx 0.6$. The subcomponents have relatively low Sérsic indices, in the range $n \approx 1-2$. They also find that the ellipticity of the isophotes systematically increases toward large radii. They believe that the combination of their model's inner and middle components for high-luminosity ellipticals resembles the compact, massive galaxies at high-z (Huang et al. 2013).

Despite there being codes that can automate the measurement of galaxy properties (e.g., Simard et al. 2002, 2011; Barden et al. 2012), there are still many disagreements over the analysis techniques, because they are often viewed as being too simple, and what the measurements mean. Even stepping up the sophistication, however, makes interpretation non-trivial unless one has physical motivations for doing so (H13). These disagreements inspire other techniques (Conselice 1997; Lotz et al. 2004) to measure galaxies non-parametrically, although each one has its own benefits and shortcomings. In addition to galaxy shapes being difficult to quantify, many other factors complicate the image analysis of galaxies, including determination of the sky background, the brightness of the galaxy [signal-to-noise ratio (S/N)], the resolution of the images, $(1+z)^4$ surface brightness dimming, finding the best PSF, the method employed for modeling the galaxy, and the potential biases of the fitting pipeline. Galaxy simulations are invaluable tools for understanding the performance of quantitative fitting pipelines because they provide control over the aforementioned factors (e.g., Trujillo et al. 2007; Cimatti et al. 2008; Mancini et al. 2010; Szomoru et al. 2010, 2012; van Dokkum & Brammer 2010; Williams et al. 2010; Papovich et al. 2012; and van der Wel et al. 2012 for high-z galaxies and Häussler et al. 2007 and Meert et al. 2013 for low-z galaxies).

[1] `http://cgs.obs.carnegiescience.edu/CGS/Home.html`

By taking advantage of existing observations, detailed analysis, and the multi-component picture of the local elliptical galaxies from H13, we address two key questions:

1) Do the quiescent massive galaxies at $z = 2$ have sizes comparable with the quiescent massive local galaxies and therefore their observed compactness is not intrinsic but an artifact of inappropriate and insufficient morphological modeling?

2) What are the true uncertainties of the size and total luminosity measurements at different S/N levels due to structural complexities?

Two sets of simulations are performed to address these questions. Model galaxies with a single Sérsic component with parameter ranges that cover the *HST*/WFC3 observations of the red nuggets are the first set of simulations we perform. These idealized simulations can determine the robustness of fitting pipelines at different noise levels (Häussler et al. 2007). Therefore, the uncertainties and systematic errors measured from these simulated galaxies can be considered as lower limits. More informative analysis is done by simulating multi-component galaxies with the properties obtained from H13. By artificially scaling modern-day galaxies to sizes and luminosities comparable to those found in galaxies at $z \approx 2$, we can fit them with single-component Sérsic models to understand the systematics caused by complexities in galaxy structures. The differences between the input and output parameters shed light on possible uncertainties and biases in size and total luminosity measurements of the high-z galaxies.

This paper is organized as follows. Section 2 gives the details of the galaxy simulations used throughout this study. In Section 3, we present the main results of our `GALFIT` models. In Section 4, we compare our results with similar studies in the literature. Implications for red nuggets are discussed in Section 5, ending with a summary in Section 6.

All the results assume a standard cosmology ($H_0 = 71$ km^{-1} s^{-1} Mpc^{-1}, $\Omega_m = 0.27$, and Ω_Λ = 0.73) and AB magnitudes.

2.2 Simulations

Simulations can determine the robustness of fitting pipelines like `GALFIT`[2]. In this section, we describe the different sets of simulations in detail.

Two sets of objects are simulated in order to address different issues. The first, using a single-component Sérsic profile, is to establish the baseline capability due only to S/N, under the most idealized situations, and in the absence of any complexities. This sets the fundamental limits of the technique. The second set of simulations, by rescaling models of nearby elliptical galaxies and all their sub-components to comparable sizes and S/N found at high z and fitting them using a single-component Sérsic model, directly tests the null hypothesis that early-type galaxies have not evolved in size since $z \approx 2$. We use Ned Wright's cosmology calculator[3] to compute redshift-dependent quantities.

2.2.1 Method

We use `GALFIT 3.0` for the simulations. `GALFIT` is an image analysis algorithm that can model profiles of galaxies, stars, and other astronomical objects in digital images. If successful, the features of interest are summarized into a small set of numbers, such as size, luminosity, profile central concentration, and geometrical parameters. `GALFIT` uses several common functions in the astronomical literature, including: exponential, Sérsic/de Vaucouleurs, Nuker, Gaussian, King, and Moffat. Out of all the functions, we exploit only the Sérsic (1968) profile and the sky background component. The sky component fits the background with a plane with a constant slope and therefore can correct for any non-flatness to first order. The Sérsic component describes the radial surface brightness profile of a galaxy as

$$\Sigma(R) = \Sigma_e \; exp\left\{-\kappa\left[\left(\frac{R}{R_e}\right)^{1/n} - 1\right]\right\}, \tag{2.1}$$

[2] `http://users.obs.carnegiescience.edu/peng/work/galfit/galfit.html`
[3] `http://www.astro.ucla.edu/~wright/CosmoCalc.html`

where R_e is the effective radius of the galaxy (equivalent to r_{50}, the half-light radius), Σ_e is the surface brightness at R_e, the Sérsic index n describes the profile shape, and the parameter κ is closely connected to n (Ciotti 1991). Together with position (x and y), axis ratio b/a, and position angle, this profile has seven free parameters. The Sérsic profile represents a more general form of the exponential light profile seen in galactic disks ($n = 1$; Freeman 1970) and the $R^{1/4}$-law (de Vaucouleurs law; de Vaucouleurs 1948) typical of luminous early-type galaxies ($n = 4$). Modeling with this profile has been explored in detail in several works (e.g., Simard & Pritchet 1998; Simard et al. 2002; Graham et al. 2005). Many authors have used a constant value of $n = 2.0$ or 2.5 to crudely distinguish early-type (bulge-dominated) from late-type (disk-dominated) galaxies (e.g., Blanton et al. 2003; Shen et al. 2003; Bell et al. 2004; Hogg et al. 2004; Ravindranath et al. 2004; Barden et al. 2005; McIntosh et al. 2005; Fisher & Drory 2008). Sérsic profiles with higher Sérsic indices have longer tails that make the analysis of these galaxies more challenging due to greater sensitivity to neighboring objects, to profile mismatch, and to accurate knowledge of the sky background (see Figure 3 of Peng et al. 2010). We will compare our results for different ranges of Sérsic indices.

Sky background and noise are added to all the images in two different ways: (1) adding an artificial background level with Poisson noise using `IRAF/mknoise`[4] (Tody 1986, 1993); (2) putting the simulated galaxy on an actually observed background. Although the main focus of this study is galaxies at $z = 2$, our simulations are more generally applicable. The simulations explore a range of fundamental measurables, i.e. sizes, Sérsic indices, axis ratio, and S/N. As the simulations extend down to instrumental limits, they apply to galaxies at any redshifts provided that one first converts apparent magnitude into S/N. As illustration, we compare galaxies at $z = 0.5$, 1.5, and 2, to our simulations. The simulated observed backgrounds are taken from CANDELS[5] (Grogin et al. 2011; Koekemoer et al. 2011) UDS (UKIDSS Ultra-Deep Survey; Lawrence et al. 2007) I_{814}, J_{125}, and H_{160} mosaic images, respectively (Figure 2.1). Therefore, when local galaxies are rescaled to specifically match in size and S/N of observed

[4] `IRAF` is distributed by the National Optical Astronomy Observatories, which are operated by the Association of Universities for Research in Astronomy, Inc., under cooperative agreement with the National Science Foundation.

[5] `http://candels.ucolick.org/`

galaxies in those filters, K-correction is not required. The simulated backgrounds resemble the observed backgrounds as they have identical gain, pixel scale, and magnitude zero point (*magzpt*) as in the UDS mosaic images. Furthermore, the background root-mean-square (RMS; the standard deviation from the median sky value) of the simulated and observed backgrounds are comparable.

All artificially generated galaxies are convolved with a CANDELS UDS hybrid PSF (van der Wel et al. 2012) of the filter that corresponds to the redshift of interest. An important factor in obtaining a best-fit model is the accuracy of the PSF. The effective radii of the red nuggets are comparable to and in some cases smaller than the PSF full-width at half maximum (FWHM). Therefore, one may expect some offset in `GALFIT` measurements when an inaccurate PSF is used. This issue is studied in the Appendix, where we show that the effects of using slightly different PSFs are not more than 5% on the final model.

One of the most important factors in morphology analysis is S/N. There are several ways to define S/N because galaxies are extended. One way, which is somewhat analogous to total S/N, is given by

$$S/N = \frac{f_{\text{galaxy}}}{\sqrt{f_{\text{galaxy}} + A\sigma^2}}, \tag{2.2}$$

where three different parameters determine the S/N: the area A of the aperture in which the S/N is measured, the galaxy total flux f_{galaxy} within A, and the background RMS σ. The RMS here is the sum of all possible sources of noise, including shot noise from the sky, readout noise, and shot noise in dark current. In this paper, A includes every pixel within R_e. Note that this is different from measuring S/N within an aperture with a constant size because the aperture size here is different for each galaxy. Equation 3.5, however, may not be the most informative. For various technical reasons, it is harder to measure structural properties of low-surface brightness galaxies. Thus, another useful definition is analogous to an average surface brightness, defined as $\langle S/N \rangle = \frac{S/N}{\sqrt{\pi R_e{}^2(1-e)}}$. Here, the ellipticity $e = 1 - b/a$. Figure 2.2 shows a set of galaxies and the corresponding S/N definitions.

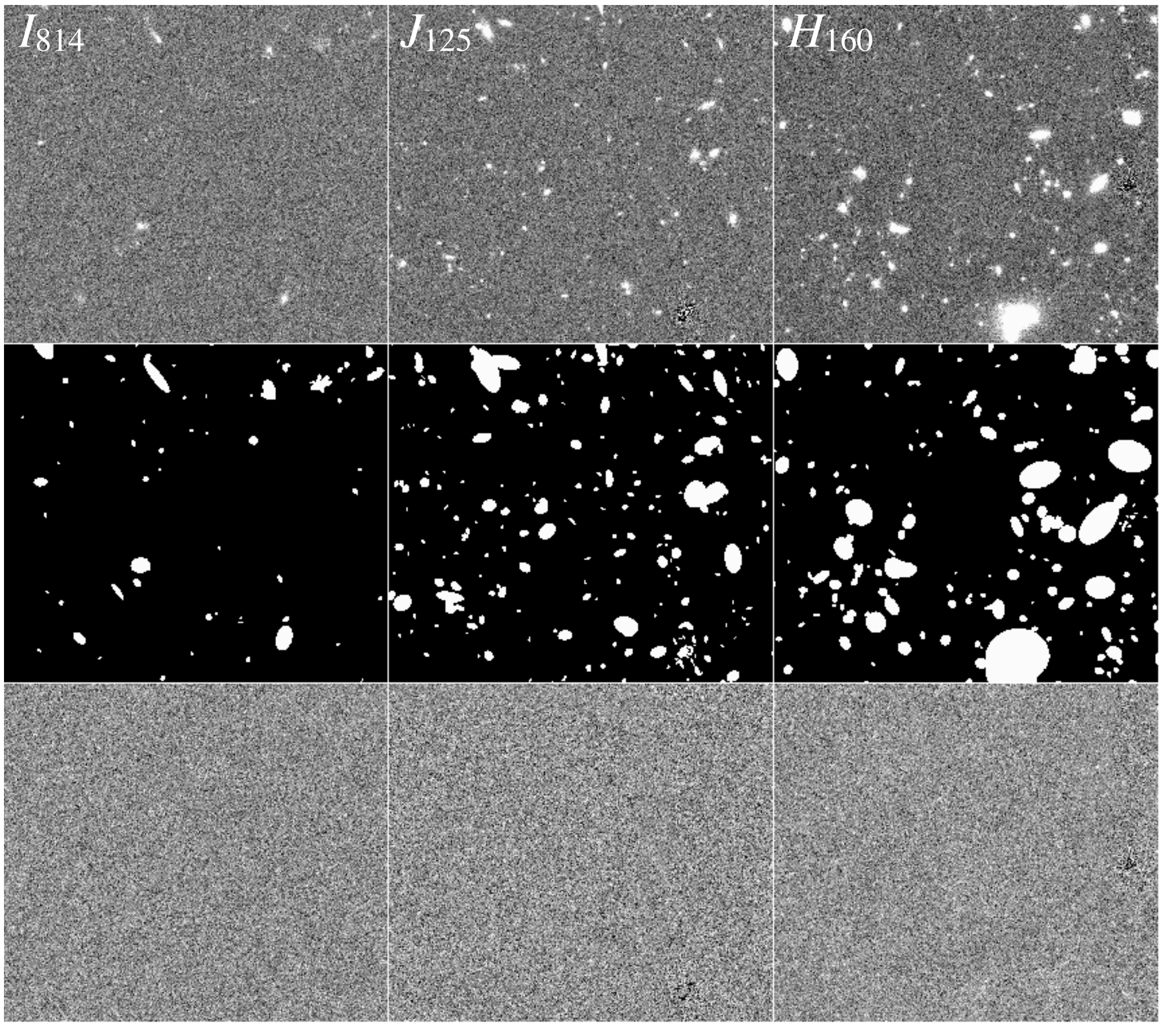

Figure 2.1: Sky backgrounds drawn from CANDELS UDS mosaic images in I_{814}, J_{125}, and H_{160}. The simulated galaxies are put at random positions on these backgrounds. The regions are 1021 × 1021 pixels (i.e., $\sim 30''$in I_{814} and $\sim 60''$in J_{125} and H_{160}), which is the size of the *HST*/ACS and *HST*/WFC3 CCDs. The middle panels show the bad pixel mask images of each sky background; the bottom panels are the backgrounds after removing the undesired objects. In the bottom panels, the masked pixels are replaced by randomly chosen background pixels. The bad pixel masks are used for `GALFIT` modeling.

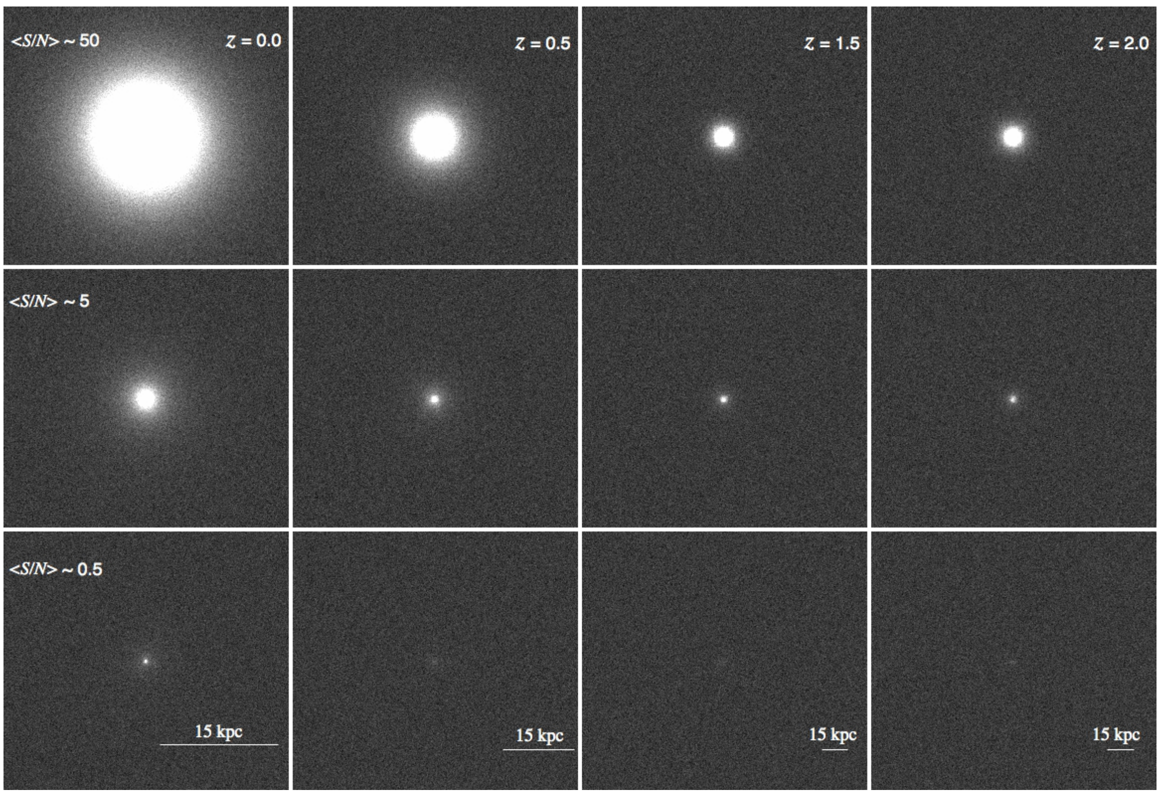

Figure 2.2: Simulated multi-component galaxies at four different redshifts and three averaged signal-to-noise ratios ($\langle S/N \rangle$). The model is based on the best-fit model for NGC 1379 from H13. The simulated galaxy at $z = 2.0$ (right columns) has $R_e = 6$ pixels and $e = 0$ and therefore this galaxy is shown at $S/N \approx 5$, 50, and 500.

By adding galaxies to an observed background, one can study the effect of faint undetected objects or being in the vicinity of bright and/or extended objects. One way to minimize the effects of neighboring objects is to mask them out. We accomplish this by running SExtractor[6] (Bertin & Arnouts 1996) with the parameter *Detection_threshold* set to 1.5. Instead of using the SExtractor segmentation map, the location (`XPEAK_IMAGE, YPEAK_IMAGE`), ellipticity, position angle, and the area of the objects from the SExtractor output catalog are used to create a bad pixel mask image. First, the semi-major axis of each galaxy is calculated by using the measured area and ellipticity of the object. Bad pixel regions are constructed by assigning the center, the semi-major axis, the semi-minor axis, and the position angle of each object. We double the calculated semi-major and semi-minor axes (i.e., quadruple the area) in order to mask out most of the faint outer parts of the objects. Figure 2.1 shows the observed backgrounds and bad pixel masks. These masks are used for `GALFIT` modeling. While masking does not fully eliminate the possibility of neighboring contamination (see Häussler et al. 2007), this method is analogous to that of some studies in the literature and is thus informative. Together with analysis on idealized backgrounds, these two scenarios give an idea of the different levels of systematics.

2.2.2 Single-component Galaxies

Simulating single-component galaxies is one of the most basic, yet important ways of testing the robustness of fitting pipelines (Häussler et al. 2007). We simulate more than 10,000 single-component galaxies. The Sérsic component parameters are randomly chosen from the following ranges: $0.8 < R_e < 35$ pixels ($\sim$0.05–2.0$''$in WFC3/H_{160}), $0.5 < n < 5$, and $0 < e < 0.8$. For one *HST* orbit, a S/N range between 1 and 1000 within the effective radius of the simulated galaxies roughly corresponds to a magnitude range of $20 < m_H < 27$.

Once the galaxies are simulated, we fit each with a single Sérsic component plus a sky component. For the galaxy component, the initial parameter guesses include the position of

[6] `http://www.astromatic.net/software/sextractor`

the galaxy (physical x and y), Sérsic index, magnitude, effective radius, ellipticity, and position angle.

2.2.3 Multi-component Galaxies

Real galaxies have structures that complicate the analysis. Several recent studies looked into this issue by creating bulge + disk models, and then fitting single-component Sérsic models to them (Meert et al. 2013; Mosleh et al. 2013). The question was whether the disk components were missed by the analysis technique, therefore leading to underestimation of the sizes. They found that single-component models were able to recover the magnitude and sizes, with only small systematic errors (0%–20%), and that the multi-component analysis performed better.

While those studies are informative in their own right, there is another complementary approach. Our simulations are designed to more directly test the null hypothesis that elliptical galaxies today are the direct descendants of $z \approx 2$ galaxies that have undergone no morphological changes in structure or size. To do so, we start with 100 nearby elliptical galaxies with multi-component decomposition models from H13 that capture the detailed structures down to very low surface brightnesses, accounting for the PSF. We then rescaled the composite (sum of the multiple components) as a single unit to span a range of sizes and signal-to-noise similar to galaxies at $z \approx 2$. We convolve the composite model with a PSF and then perform single-component Sérsic fits to it. The rationale for this approach is to be agnostic about the structural nature of high-z systems (e.g., whether they are disks or bulges) because that judgment may itself be entangled with the technique as well as other more subtle technical nuances.

We rescale the sizes and luminosities of the H13 multi-component models to generate about 300 multi-component galaxies with $R_e \approx 1-70$ pixels and S/N from a few to 1000. This range is relevant for studying massive early type galaxies down to the resolution and S/N limits of *HST* observations, regardless of redshift. Images of galaxies analogous to being at $z = 0.5$, 1.5, and 2.0 are simulated based on the S/N properties of I_{814}, J_{125} , and H_{160} (equivalent to the rest-frame optical) CANDELS UDS images, respectively.

As in the single-component simulations, we add either a simulated background or an observed background. By using 300 multi-component galaxies as templates, more than 6000 galaxies with $5 < S/N < 1000$ (uniformly distributed in logarithmic space) are simulated.

We analyze the multi-component galaxies in a manner similar to that used to treat the single-component galaxies. To replicate the most commonly adopted analysis method, we fit every galaxy with a single Sérsic and sky component. However, because of the mixture of different components, another method is needed to determine the intrinsic size and other parameters of the galaxy. To establish the baseline for comparison of sizes and other parameters, we employ `IRAF/ellipse` (Jedrzejewski 1987), a task that fits elliptical isophotes to images, to create a curve of growth (CoG) of the cumulative radial flux distribution of the model galaxy. This is generated with an ellipticity and position angle fixed to the radially average value. No noise is added, and PSF convolution is not applied. As the total flux of the galaxy is known, the CoG allows us to obtain a non-parametric estimate of the effective radius, the radius at which half of the total flux is enclosed.

To examine the robustness of our CoG analysis, we employ this method to measure the sizes of 1250 single-component galaxies with a large range of sizes (1–500 pixels). Figure 2.3 shows that there is no bias in size measurements for the larger galaxies but the finite size of the pixels makes size determination of the smallest galaxies slightly uncertain. Sizes with $1 < R_e < 2$ pixels can be overestimated by 5% and with 10% uncertainty. For galaxies with $2 < R_e < 5$ pixels, the sizes can be measured without any bias and with 5% uncertainty. And for larger galaxies the uncertainties are less than 1% with no bias. We take these effects into consideration when analyzing the multi-component galaxies. However, fewer than 2% of the simulated galaxies have $R_e < 3$ pixels.

Lastly, we note that because the CoG technique averages over all elliptical annuli to measure the effective radius, the comparison between CoG and single-component Sérsic fits in principle is imperfect for multi-component galaxies whose isophotes often change in ellipticity with radius. Nevertheless, the general agreement in the size measurements between the two methods is reassuring.

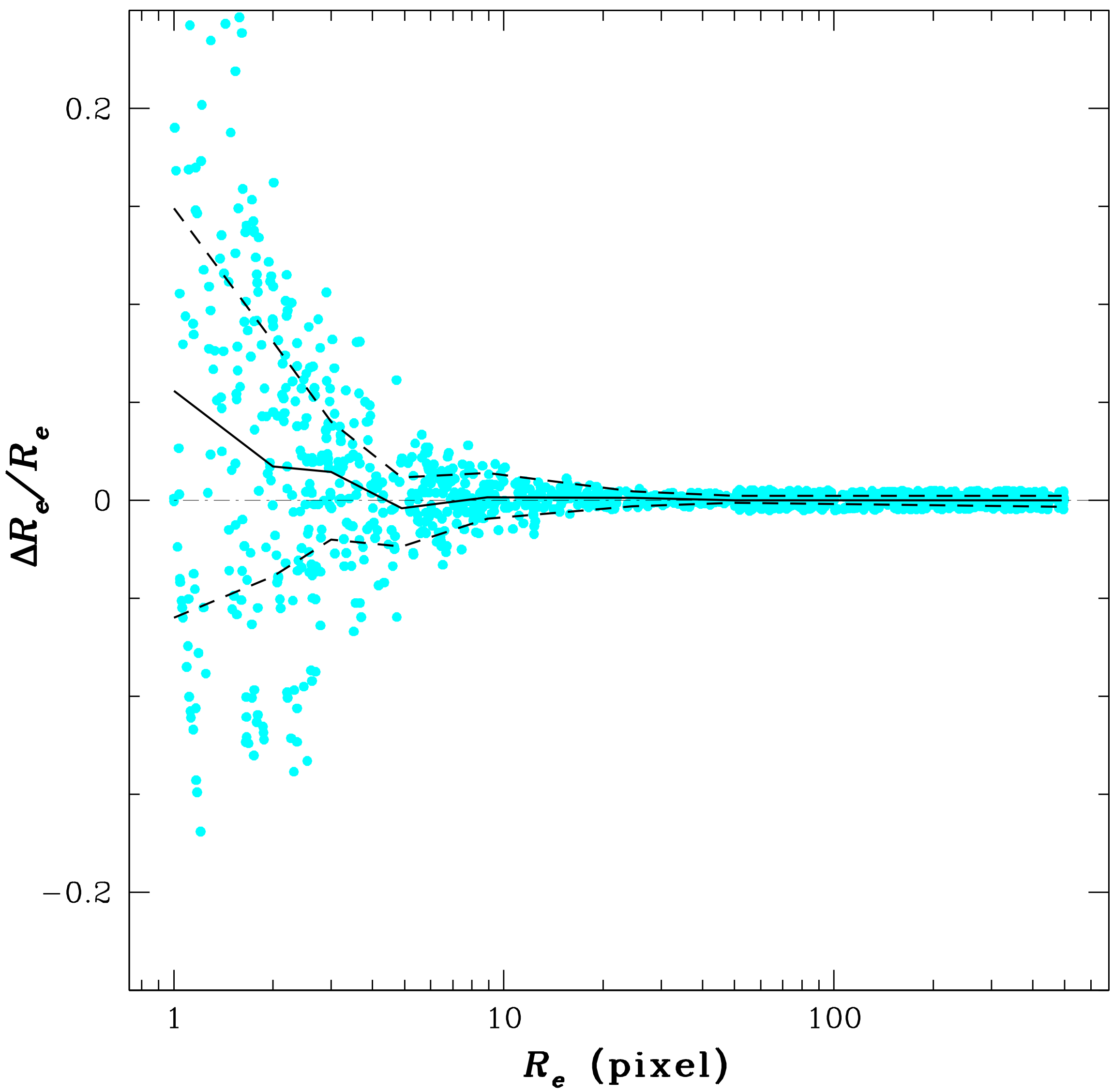

Figure 2.3: Testing the reliability of size measurements using curve of growth (CoG) analysis. The x-axis shows the effective radius of 1250 single-component galaxies, and the y-axis shows the difference between the actual size and the size measured by CoG. Black solid and dashed lines indicate the median and 1σ uncertainties. The dot-dash line shows zero offset. The size of galaxies with $1 < R_e < 2$ pixels can be overestimated by 5% and with 10% uncertainties. For galaxies with $2 < R_e < 5$ pixels, the sizes can be measured without any bias and with 5% uncertainties. And for larger galaxies the uncertainties are less than 1% with no bias.

2.3 Results

2.3.1 Single-component Galaxies

Figure 2.4 and Table 1 summarize the results of single-component galaxies with a simulated background; these are the most idealized simulations to establish the baseline behavior of the analysis technique for the S/N range of interest. Black solid and dashed lines in the scatter plots indicate the median and 1σ uncertainties of different measurements. Cyan points and cyan solid lines show the results of galaxies with input $n < 2.5$, and red points and red dotted lines are for galaxies with $n \geq 2.5$.

To be consistent with the multi-component models later on, where effective radius is more ambiguous to define, the analyzed effective radii are circularized effective radii, $R_{e,\mathrm{circularized}} \equiv R_{e,\mathrm{GALFIT}} \times \sqrt{1-e}$.

We see no systematic errors in size, total luminosity, Sérsic index, or ellipticity measurements down to $m_H = 26$. And even at $26 < m_H < 27$ the systematic errors are less than $\sim$10%. As expected, the uncertainties increase rapidly with decreasing S/N and particularly for $m_H >$ 26. The Sérsic index is most vulnerable to large uncertainties. The simulated images resemble single-orbit *HST*/WFC3 H_{160} observations; a galaxy with $R_e = 5$ pixels (i.e., 0.3$''$or 2.5 kpc at z = 2), $e = 0$, and $m_H = 26$ has $S/N \approx 15$ within R_e.

The uncertainties are, on average, higher for galaxies with larger Sérsic indices but the systematic offsets are comparable at different n (note that all the simulated single-component galaxies have $n < 5$). Most of the galaxies with the largest scatter within a magnitude range are ones with the largest sizes, as they have lower mean surface brightness compared to the smaller galaxies.

Figure 2.5 and Table 2 summarize the results of single-component galaxies with an observed background, derived from real images. The scatter is larger but systematic errors are still absent down to $m_H \approx 25$. One of the main sources of the increased scatter is the presence of bright and/or extended objects in the actual images of the observed background (Figure 2.1).

It is worth pointing out that masking out objects (using a bad pixel mask for `GALFIT` fitting)

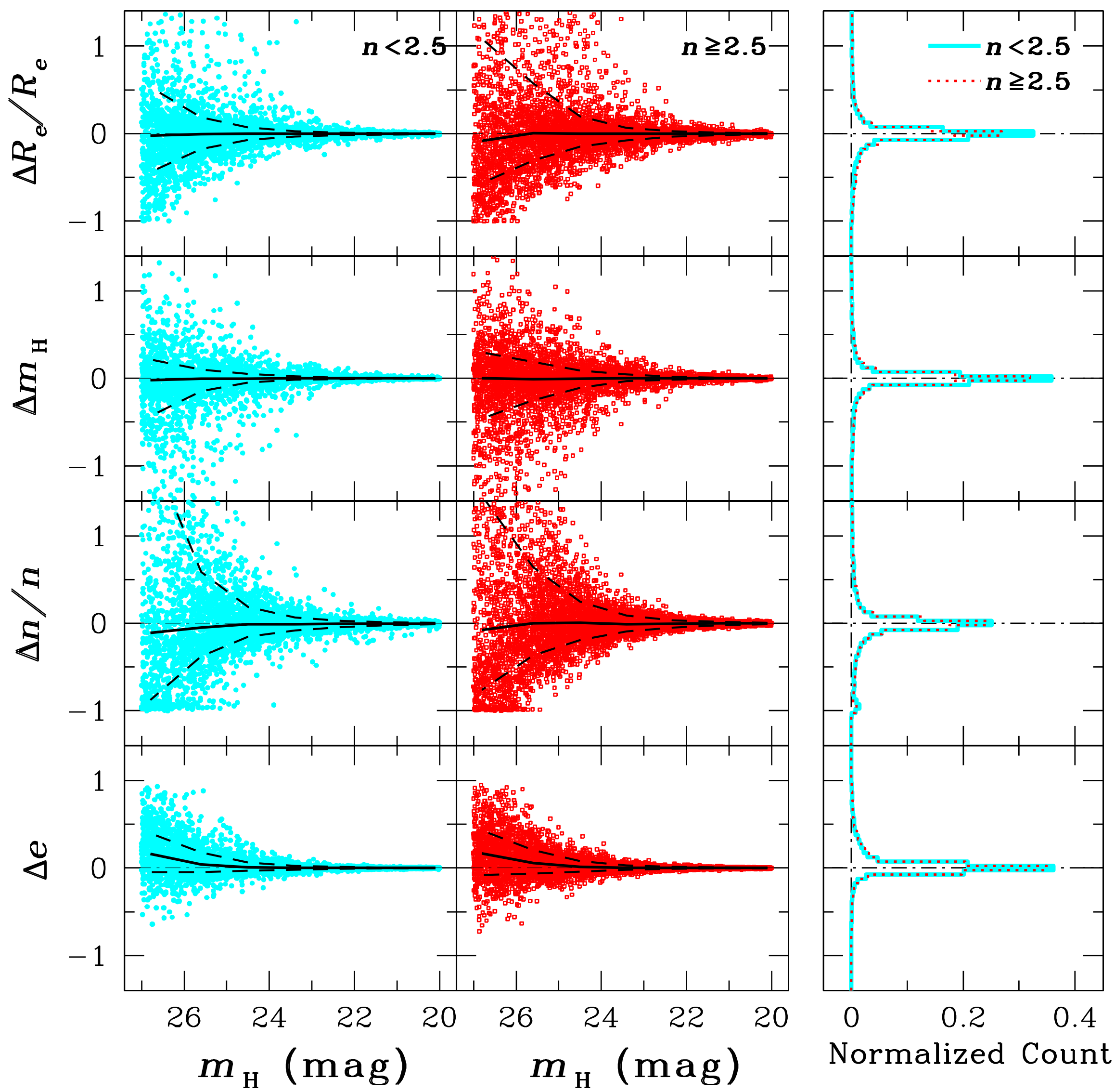

Figure 2.4: The results of more than 10,000 single-component model galaxies with a simulated background. From top to bottom, panels show the offsets between the measured and the actual effective radius R_e, magnitude m_H (in one *HST* orbit), Sérsic index n, and ellipticity e, respectively. Black solid and dashed lines in the scatter plots indicate the median and 1σ uncertainties of different measurements. The dot-dash lines show the zero offset. Cyan points and cyan solid lines show the results of galaxies with input $n < 2.5$, and red points and red dotted lines are for galaxies with $n \geq 2.5$. The median offsets are zero down to $m_H \approx 26$, but the scatter rises steeply in the magnitude range between 25 and 26.

Table 2.1: Single-Component Galaxies with Simulated Background

	$\Delta R_e/R_e$		Δm_H		$\Delta n/n$		Δe	
m_H	n<2.5	n≥2.5	n<2.5	n≥2.5	n<2.5	n≥2.5	n<2.5	n≥2.5
(1)	(2)	(3)	(4)	(5)	(6)	(7)	(8)	(9)
20 – 21	$-0.00^{+0.01}_{-0.01}$	$-0.00^{+0.01}_{-0.01}$	$0.00^{+<0.01}_{-<0.01}$	$0.00^{+0.01}_{-<0.01}$	$-0.0^{+<0.1}_{-<0.1}$	$-0.0^{+<0.1}_{-<0.1}$	$0.00^{+<0.01}_{-<0.01}$	$0.00^{+<0.01}_{-<0.01}$
21 – 22	$-0.00^{+0.01}_{-0.01}$	$-0.00^{+0.01}_{-0.02}$	$0.00^{+0.01}_{-<0.01}$	$0.00^{+0.01}_{-0.01}$	$-0.0^{+<0.1}_{-<0.1}$	$-0.0^{+<0.1}_{-<0.1}$	$-0.00^{+0.01}_{-0.01}$	$0.00^{+0.01}_{-0.01}$
22 – 23	$-0.00^{+0.01}_{-0.01}$	$-0.00^{+0.03}_{-0.03}$	$0.00^{+0.01}_{-0.01}$	$0.00^{+0.02}_{-0.01}$	$-0.0^{+<0.1}_{-<0.1}$	$-0.0^{+<0.1}_{-<0.1}$	$0.00^{+0.01}_{-0.01}$	$0.00^{+0.01}_{-0.01}$
23 – 24	$-0.00^{+0.03}_{-0.03}$	$-0.00^{+0.07}_{-0.07}$	$0.00^{+0.02}_{-0.02}$	$0.00^{+0.04}_{-0.03}$	$-0.0^{+0.1}_{-0.1}$	$-0.0^{+0.1}_{-0.1}$	$0.00^{+0.02}_{-0.02}$	$0.00^{+0.03}_{-0.02}$
24 – 25	$-0.00^{+0.07}_{-0.07}$	$-0.00^{+0.20}_{-0.15}$	$-0.00^{+0.05}_{-0.05}$	$-0.00^{+0.09}_{-0.11}$	$-0.0^{+0.2}_{-0.1}$	$0.0^{+0.2}_{-0.2}$	$0.01^{+0.06}_{-0.04}$	$0.02^{+0.06}_{-0.06}$
25 – 26	$-0.01^{+0.19}_{-0.17}$	$0.00^{+0.57}_{-0.31}$	$-0.01^{+0.10}_{-0.14}$	$-0.01^{+0.19}_{-0.25}$	$-0.1^{+0.6}_{-0.3}$	$-0.0^{+0.6}_{-0.4}$	$0.04^{+0.13}_{-0.09}$	$0.06^{+0.15}_{-0.12}$
26 – 27	$-0.02^{+0.55}_{-0.42}$	$-0.08^{+1.17}_{-0.48}$	$-0.02^{+0.24}_{-0.41}$	$0.00^{+0.30}_{-0.43}$	$-0.1^{+2.1}_{-0.8}$	$-0.1^{+1.5}_{-0.7}$	$0.16^{+0.24}_{-0.21}$	$0.17^{+0.26}_{-0.25}$

All the offsets are shown for Sérsic indices smaller and larger than 2.5.

Col. (1) H_{160} magnitude.
Col. (2-3) The effective radius offset.
Col. (4-5) The magnitude offset.
Col. (6-7) The Sérsic index offset.
Col. (8-9) The ellipticity offset.

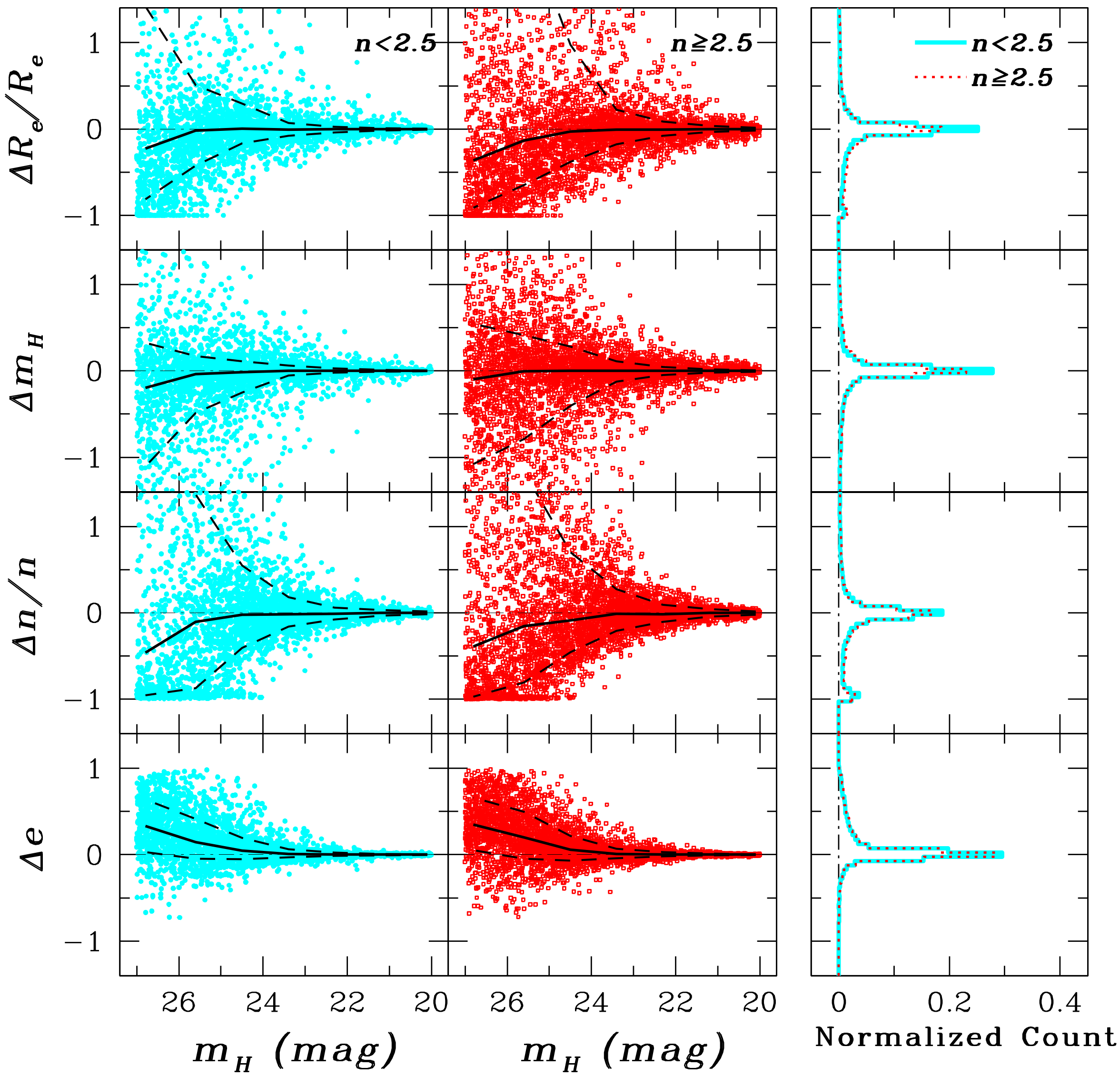

Figure 2.5: The results of more than 10,000 single-component model galaxies with an observed background. From top to bottom, panels show the offsets between the measured and the actual effective radius R_e, magnitude m_H (in one *HST* orbit), Sérsic index n, and ellipticity e, respectively. Black solid and dashed lines in the scatter plots indicate the median and 1σ uncertainties of different measurements. The dot-dash lines show the zero offset. Cyan points and cyan solid lines show the results of galaxies with input $n < 2.5$, and red points and red dotted lines are for galaxies with $n \geq 2.5$. The median offsets are zero down to $m_H \approx 25$, but the scatter rises steeply in the magnitude range between 24 and 25.

Table 2.2: Single-Component Galaxies with Observed Background

	$\Delta R_e/R_e$		Δm_H		$\Delta n/n$		Δe	
m_H (1)	n<2.5 (2)	n≥2.5 (3)	n<2.5 (4)	n≥2.5 (5)	n<2.5 (6)	n≥2.5 (7)	n<2.5 (8)	n≥2.5 (9)
20 – 21	$-0.00^{+0.01}_{-0.01}$	$-0.00^{+0.01}_{-0.01}$	$0.00^{+<0.01}_{-<0.01}$	$0.00^{+0.01}_{-0.01}$	$-0.0^{+<0.1}_{-<0.1}$	$-0.0^{+<0.1}_{-<0.1}$	$0.00^{+<0.01}_{-<0.01}$	$0.00^{+<0.01}_{-<0.01}$
21 – 22	$-0.00^{+0.01}_{-0.02}$	$-0.00^{+0.04}_{-0.04}$	$-0.00^{+0.01}_{-0.01}$	$0.00^{+0.02}_{-0.02}$	$-0.0^{+<0.1}_{-<0.1}$	$-0.0^{+<0.1}_{-<0.1}$	$0.00^{+0.01}_{-0.01}$	$0.00^{+0.01}_{-0.01}$
22 – 23	$-0.00^{+0.03}_{-0.04}$	$-0.01^{+0.10}_{-0.07}$	$0.00^{+0.03}_{-0.02}$	$0.00^{+0.04}_{-0.05}$	$-0.0^{+0.1}_{-0.1}$	$-0.0^{+0.1}_{-0.1}$	$0.00^{+0.02}_{-0.02}$	$0.00^{+0.03}_{-0.02}$
23 – 24	$-0.01^{+0.08}_{-0.07}$	$-0.01^{+0.23}_{-0.17}$	$0.00^{+0.06}_{-0.05}$	$0.00^{+0.11}_{-0.13}$	$-0.0^{+0.2}_{-0.1}$	$-0.0^{+0.3}_{-0.2}$	$0.01^{+0.05}_{-0.04}$	$0.01^{+0.06}_{-0.05}$
24 – 25	$0.01^{+0.29}_{-0.17}$	$-0.03^{+1.00}_{-0.35}$	$-0.01^{+0.12}_{-0.24}$	$0.00^{+0.28}_{-0.39}$	$-0.0^{+0.6}_{-0.4}$	$-0.1^{+0.8}_{-0.4}$	$0.04^{+0.15}_{-0.10}$	$0.06^{+0.16}_{-0.13}$
25 – 26	$-0.02^{+0.53}_{-0.41}$	$-0.13^{+2.54}_{-0.52}$	$-0.04^{+0.21}_{-0.45}$	$-0.00^{+0.41}_{-0.75}$	$-0.1^{+1.5}_{-0.8}$	$-0.2^{+1.8}_{-0.7}$	$0.15^{+0.27}_{-0.19}$	$0.20^{+0.30}_{-0.24}$
26 – 27	$-0.22^{+1.65}_{-0.59}$	$-0.36^{+1.93}_{-0.55}$	$-0.20^{+0.52}_{-0.91}$	$-0.10^{+0.64}_{-0.88}$	$-0.5^{+3.9}_{-0.5}$	$-0.4^{+2.7}_{-0.6}$	$0.33^{+0.30}_{-0.30}$	$0.35^{+0.31}_{-0.29}$

All the offsets are shown for Sérsic indices smaller and larger than 2.5.

Col. (1) H_{160} magnitude.
Col. (2-3) The effective radius offset.
Col. (4-5) The magnitude offset.
Col. (6-7) The Sérsic index offset.
Col. (8-9) The ellipticity offset.

is not the most effective way to mitigate the effects of neighboring objects. Instead, one needs to fit the target galaxy and its neighboring objects simultaneously (e.g., Häussler et al. 2007; Barden et al. 2012). The properties (e.g., magnitude, size, and Sérsic index) of the neighboring objects can affect the fit of the target object. In particular, neighbors with the largest $n \times R_e$ have the largest effects.

Another important factor to consider is that we do not provide an input sigma image (i.e., noise map) for `GALFIT`; instead, we allow `GALFIT` to calculate it. CANDELS images are generated through an extensive process from raw, single exposures to final, drizzled mosaics. The noise tends to be correlated after the `multidrizzle` procedure, which may lead to underestimating the noise in actual data (Fruchter et al. 2009). The sigma image generated by `GALFIT` may not include all the necessary information about the image characteristics required for a faithful noise map. van der Wel et al. (2012) have analyzed the CANDELS UDS H_{160} image and note that the total flux of objects with $m_H \approx 22 - 23$ and the size of typical objects in their sample (i.e., $\sim$0.3$''$or $\sim$5 pixels) correspond to the typical background flux level measured within the effective radius. Although our images with simulated backgrounds have similar RMS to CANDELS UDS H_{160} image, the galaxy flux and the background flux are comparable at $m_H \approx 23.5$ for images with simulated backgrounds. This can explain some of the discrepancies between Figure 2.4 and Figure 2.5, even at the bright end.

2.3.2 Multi-component Galaxies

Simulated galaxies with multiple components, where the subcomponents are taken from accurate decompositions of nearby galaxies of H13, provide a better description of the observed galaxy structures than idealized single-component models. We examine the reliability of measuring the size and total luminosity of multi-component galaxies by single-component fitting.

Figure 2.6 and Tables 3 and 4 show the difference between actual and measured effective radii at different S/N ranges for about 7,000 model galaxies in images with simulated (i.e. idealized) backgrounds. The upper, middle, and lower panels give the results at different intervals of size, mean surface brightness, and Sérsic index, respectively. Black solid and dashed lines

Table 2.3: $\Delta R_e/R_e$ for Multi-Component Galaxies with Simulated Background

		S/N							
	Subsample	5 – 10	10 – 20	20 – 35	35 – 70	70 – 135	135 – 265	265 – 515	515 – 1000
(1)	(2)	(3)	(4)	(5)	(6)	(7)	(8)	(9)	(10)
R_e	1 – 5	$-0.24^{+2.39}_{-0.49}$	$-0.21^{+1.68}_{-0.31}$	$-0.06^{+0.64}_{-0.34}$	$-0.01^{+0.31}_{-0.32}$	$0.03^{+0.19}_{-0.49}$	$0.04^{+0.09}_{-0.49}$	$0.04^{+0.06}_{-0.49}$	$0.03^{+0.06}_{-0.13}$
	5 – 20	$0.02^{+3.24}_{-0.62}$	$0.14^{+1.45}_{-0.50}$	$0.17^{+0.79}_{-0.35}$	$0.21^{+0.42}_{-0.27}$	$0.18^{+0.37}_{-0.18}$	$0.19^{+0.26}_{-0.15}$	$0.15^{+0.22}_{-0.12}$	$0.12^{+0.16}_{-0.08}$
	20 – 70	$0.13^{+2.09}_{-0.69}$	$0.09^{+1.13}_{-0.48}$	$0.19^{+0.86}_{-0.41}$	$0.18^{+0.95}_{-0.26}$	$0.23^{+0.43}_{-0.24}$	$0.19^{+0.43}_{-0.18}$	$0.25^{+0.36}_{-0.21}$	$0.27^{+0.26}_{-0.22}$
$\langle\mu\rangle$	16 – 21	...	...	...	...	$-0.48^{+0.05}_{-0.17}$	$-0.03^{+0.19}_{-0.45}$	$0.07^{+0.14}_{-0.16}$	$0.11^{+0.17}_{-0.09}$
	21 – 24	$-0.53^{+1.45}_{-0.40}$	$-0.21^{+0.98}_{-0.46}$	$0.05^{+0.49}_{-0.35}$	$0.11^{+0.37}_{-0.23}$	$0.17^{+0.37}_{-0.18}$	$0.18^{+0.32}_{-0.15}$	$0.23^{+0.38}_{-0.16}$	$0.32^{+0.28}_{-0.26}$
	24 – 27	$0.04^{+2.75}_{-0.63}$	$0.09^{+1.44}_{-0.47}$	$0.19^{+0.86}_{-0.37}$	$0.26^{+0.72}_{-0.29}$	$0.23^{+0.33}_{-0.23}$	...	...	...
n	0 – 2.5	$-0.55^{+0.32}_{-0.19}$	$-0.37^{+0.25}_{-0.24}$	$-0.27^{+0.22}_{-0.23}$	$-0.29^{+0.24}_{-0.21}$	$-0.21^{+0.12}_{-0.26}$	$-0.19^{+0.12}_{-0.26}$	$-0.17^{+0.06}_{-0.32}$	$-0.12^{+0.10}_{-0.36}$
	2.5 – 6	$-0.12^{+0.58}_{-0.43}$	$-0.03^{+0.49}_{-0.35}$	$0.05^{+0.37}_{-0.26}$	$0.09^{+0.24}_{-0.19}$	$0.13^{+0.17}_{-0.14}$	$0.13^{+0.15}_{-0.10}$	$0.13^{+0.17}_{-0.09}$	$0.11^{+0.12}_{-0.08}$
	6 – 20	$1.93^{+4.44}_{-1.99}$	$1.47^{+1.98}_{-1.32}$	$1.05^{+1.23}_{-0.69}$	$0.74^{+0.98}_{-0.47}$	$0.60^{+0.53}_{-0.36}$	$0.62^{+0.51}_{-0.40}$	$0.63^{+0.34}_{-0.49}$	$0.50^{+0.38}_{-0.35}$

The difference between the actual and measured magnitude m for model galaxies rescaled to $z = 2$. Single Sérsic fits with $n > 6$ are refitted by fixing the Sérsic index to $n = 6$.

Col. (1) Parameter.
Col. (2) The subsamples selected based on different ranges of effective radius (R_e), surface brightness ($\langle\mu\rangle$), and Sérsic index (n).
Col. (3-10) Equally (in logarithmic space) spaced intervals of S/N. See text in Section 3.2 regarding the offsets in different Sérsic index.

in the scatter plots indicate the median and 1σ uncertainties of different measurements. The downward-pointing arrows on the top of each subpanel indicate the S/N of a galaxy with $R_e =$ 5 pixels, $e = 0$, and $m_H = 20$ or 25 (one orbit). Typical red nugget galaxies in CANDELS have $m_H \approx 20 - 23$.

A notable feature in Figure 2.6 are the results for galaxies with $6 < n < 20$. Note that we do not impose an upper limit on the Sérsic index; $n = 20$ is an internal upper limit set by GALFIT. It is clear that the fits with $n > 6$ are generally unreliable. Sérsic profiles with $n > 4$ have long tails. In a regime where the surface brightness of the galaxy is close to the sky level, the flux in the long tail can be overestimated due to the inherent degeneracy

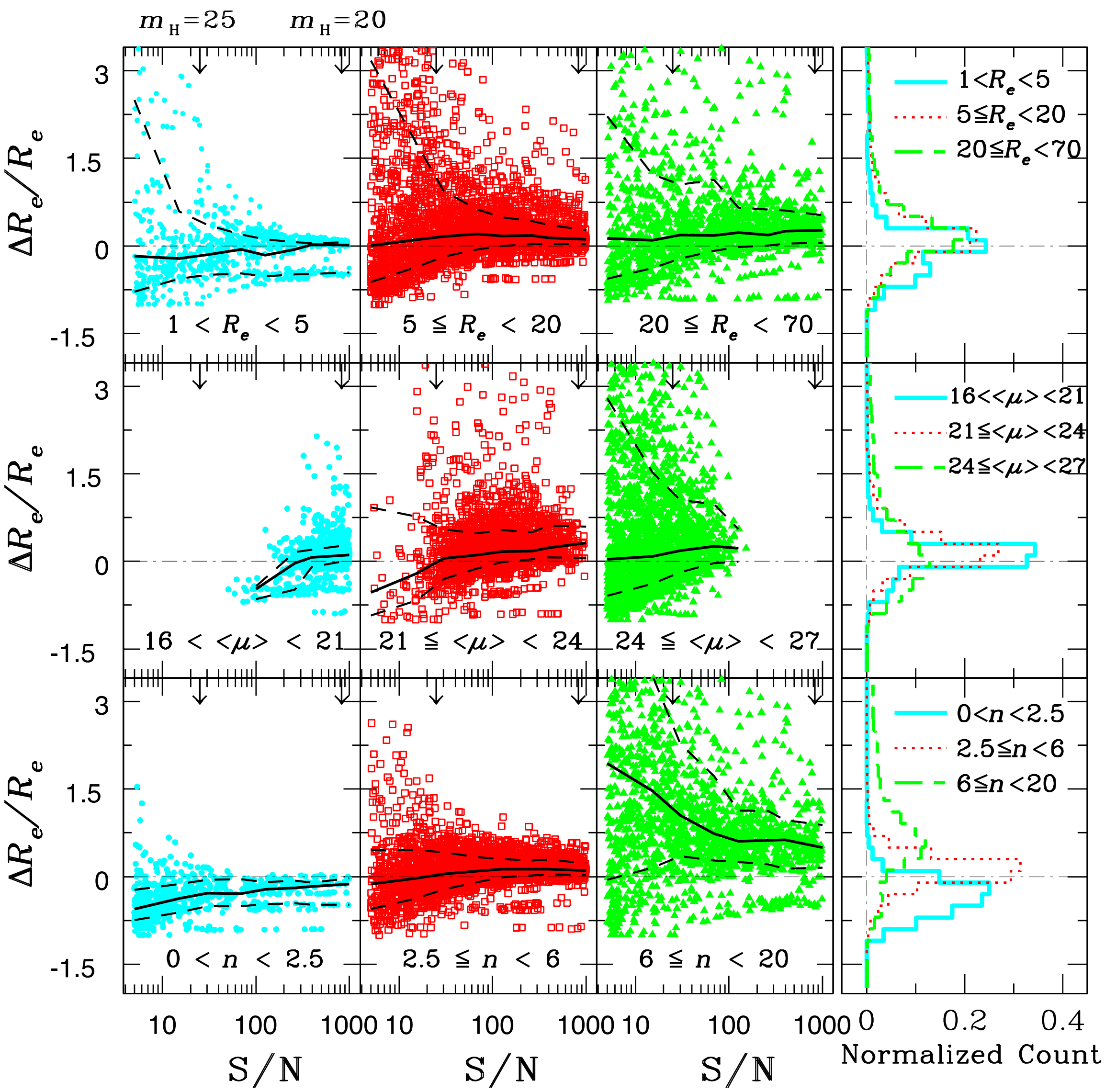

Figure 2.6: Results of more than 7,000 multi-component galaxies with simulated backgrounds. The upper, middle, and lower panels show the results at different intervals of size R_e (pixel), mean surface brightness $\langle\mu\rangle$ (m_H arcsec^{-2}), and Sérsic index n, respectively. Black solid and dashed lines in the scatter plots indicate the median and 1σ uncertainties of different measurements. The dot-dash lines show the zero offset. The downward-pointing arrows in the scatter plots indicate the S/N of a galaxy with $R_e = 5$ pixels, $e = 0$, and $m_H = 20$ and 25. Note the significant size and total luminosity overestimations of GALFIT models with $n > 6$; see text in Section 3.2 regarding the offsets in different bin internals of Sérsic index.

Table 2.4: Δm_H for Multi-Component Galaxies with Simulated Background

		S/N							
	Subsample	5 – 10	10 – 20	20 – 35	35 – 70	70 – 135	135 – 265	265 – 515	515 – 1000
(1)	(2)	(3)	(4)	(5)	(6)	(7)	(8)	(9)	(10)
R_e	1 – 5	$-0.04^{+0.41}_{-0.65}$	$0.08^{+0.22}_{-0.64}$	$0.02^{+0.30}_{-0.27}$	$-0.01^{+0.20}_{-0.12}$	$-0.05^{+0.31}_{-0.07}$	$-0.03^{+0.22}_{-0.06}$	$-0.01^{+0.18}_{-0.05}$	$-0.02^{+0.07}_{-0.04}$
	5 – 20	$-0.14^{+0.56}_{-0.59}$	$-0.13^{+0.37}_{-0.37}$	$-0.10^{+0.21}_{-0.25}$	$-0.11^{+0.13}_{-0.16}$	$-0.10^{+0.09}_{-0.13}$	$-0.10^{+0.07}_{-0.12}$	$-0.09^{+0.07}_{-0.10}$	$-0.08^{+0.05}_{-0.08}$
	20 – 70	$-0.11^{+0.57}_{-0.62}$	$-0.06^{+0.33}_{-0.35}$	$-0.10^{+0.23}_{-0.25}$	$-0.09^{+0.12}_{-0.29}$	$-0.12^{+0.13}_{-0.14}$	$-0.10^{+0.09}_{-0.15}$	$-0.13^{+0.10}_{-0.12}$	$-0.14^{+0.11}_{-0.09}$
$\langle\mu\rangle$	16 – 21	...	...	...	...	$0.26^{+0.16}_{-0.26}$	$0.02^{+0.37}_{-0.11}$	$-0.05^{+0.09}_{-0.06}$	$-0.07^{+0.06}_{-0.09}$
	21 – 24	$0.14^{+0.45}_{-0.57}$	$0.08^{+0.36}_{-0.48}$	$-0.03^{+0.25}_{-0.23}$	$-0.07^{+0.14}_{-0.15}$	$-0.10^{+0.10}_{-0.14}$	$-0.10^{+0.07}_{-0.13}$	$-0.13^{+0.08}_{-0.13}$	$-0.16^{+0.12}_{-0.09}$
	24 – 27	$-0.14^{+0.55}_{-0.60}$	$-0.09^{+0.35}_{-0.40}$	$-0.12^{+0.24}_{-0.24}$	$-0.14^{+0.16}_{-0.20}$	$-0.12^{+0.10}_{-0.13}$	...	...	...
n	0 – 2.5	$0.40^{+0.35}_{-0.39}$	$0.29^{+0.27}_{-0.25}$	$0.27^{+0.25}_{-0.23}$	$0.27^{+0.33}_{-0.21}$	$0.25^{+0.25}_{-0.18}$	$0.22^{+0.32}_{-0.20}$	$0.20^{+0.37}_{-0.19}$	$0.15^{+0.4}_{-0.14}$
	2.5 – 6	$-0.04^{+0.41}_{-0.35}$	$-0.01^{+0.25}_{-0.24}$	$-0.03^{+0.17}_{-0.18}$	$-0.06^{+0.11}_{-0.11}$	$-0.08^{+0.08}_{-0.08}$	$-0.08^{+0.06}_{-0.07}$	$-0.08^{+0.06}_{-0.07}$	$-0.07^{+0.05}_{-0.06}$
	6 – 20	$-0.42^{+0.41}_{-0.67}$	$-0.45^{+0.34}_{-0.29}$	$-0.35^{+0.19}_{-0.20}$	$-0.28^{+0.15}_{-0.20}$	$-0.25^{+0.12}_{-0.11}$	$-0.25^{+0.14}_{-0.10}$	$-0.25^{+0.17}_{-0.08}$	$-0.21^{+0.14}_{-0.10}$

The difference between the actual and measured magnitude m for model galaxies rescaled to $z = 2$. Single Sérsic fits with $n > 6$ are refitted by fixing the Sérsic index to $n = 6$.

Col. (1) Parameter.
Col. (2) The subsamples selected based on different ranges of effective radius (R_e), surface brightness ($\langle\mu\rangle$), and Sérsic index (n).
Col. (3-10) Equally (in logarithmic space) spaced intervals of S/N. See text in Section 3.2 regarding the offsets in different Sérsic index.

between a Sérsic profile with large n and any residual background flux. This leads not only to overestimating the total flux of the galaxy but also its size. On the other hand, for all practical purposes, on can correct for this effect by refitting the galaxies with $n > 6$ by fixing n to 6. Figure 2.7 demonstrates the significant improvement in the size determination. Comparing Figures 2.6 and 2.7 clarifies that most of the outliers in Figure 2.6 are galaxies with $n > 6$. It is worth noting that because the simulations are based on a finite sample of 100 nearby galaxy "templates," rescaled in luminosity and size, the behavior of the scatter is only pseudo-random, which leads to horizontal striations in the scatter plots of Figure 2.6.

Figures 2.6 and 2.7 (and 2.8) show that when the objects are binned by measured Sérsic index, the scatter does not appear symmetric in the lowest bin in n. One might interpret the result as the fit missing the outer parts of the galaxies. However, that offset is deceptive because the objects are plotted according to their measured Sérsic index rather than intrinsic index; one does not know the Sérsic index for real, multi-component galaxies until after the fit. Because measured Sérsic indices are positively correlated in a fit with measured sizes (Yoon et al. 2011), objects selected to have low measured Sérsic index typically would have smaller measured sizes. This is seen in the extreme, comparing Figures 2.6 and 2.7, for the bin where $n > 6$. In Figure 2.7, the measured sizes become much smaller when $n > 6$ objects are constrained to $n = 6$. The apparent systematic bias is therefore an artifact of the Sérsic index not being an independent variable in the simulation. In contrast, when all the objects are grouped together without regard to Sérsic index, the scatter is more symmetric about the mean (top row).

Tables 5 and 6 summarize the results of the best-fit multi-component models. On average, across the entire S/N range of interest, the size of the galaxies and their total luminosities are slightly underestimated at very low S/N. On the other hand, a small but positive trend is present, as seen in Figure 2.7, at higher S/N values. The multi-component galaxies are drawn from CGS elliptical galaxies and the Sérsic indices of these galaxies should peak around $n = 4$, as seen in our results ($< 15\%$ have $n < 2.5$, and $< 20\%$ have $n > 6$).

There is a weak size dependence in the size determination of the galaxies. The systematic offsets of galaxies with $S/N > 50$ are smaller for smaller galaxies. Figure 2.3 indicates that the

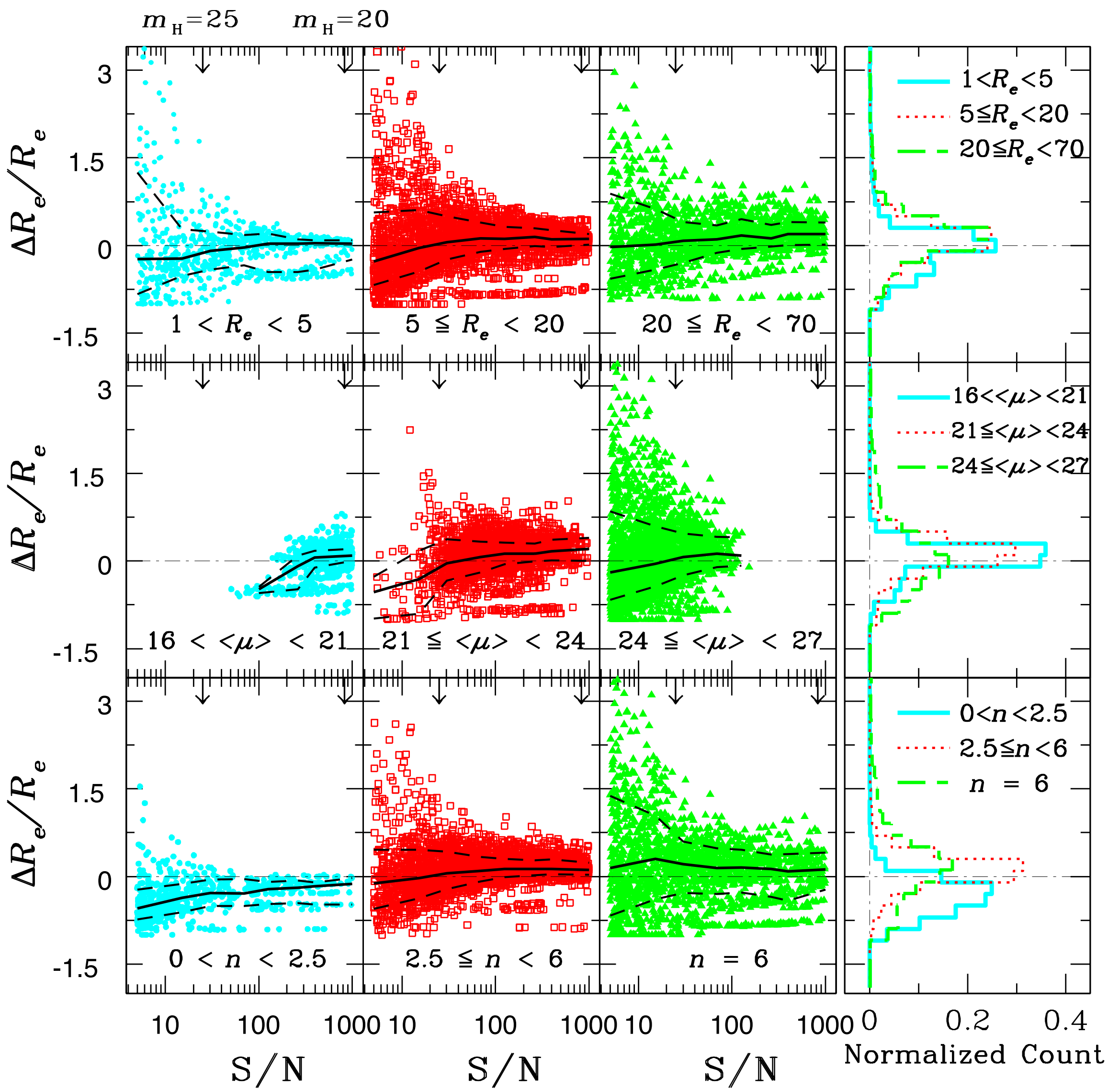

Figure 2.7: Results of more than 7,000 multi-component galaxies with a simulated background. The upper, middle, and lower panels show the results at different intervals of size R_e (pixel), mean surface brightness $\langle\mu\rangle$ (m_H arcsec^{-2}), and Sérsic index n, respectively. Black solid and dashed lines in the scatter plots indicate the median and 1σ uncertainties of different measurements. The dot-dash lines show the zero offset. The downward-pointing arrows in the scatter plots indicate the S/N of a galaxy with $R_e = 5$ pixels, $e = 0$, and $m_H = 20$ and 25. Galaxies with $n > 6$ are refit by fixing the Sérsic index to $n = 6$. Note the significant decrease in scatter and systematic errors (compare with Figure 2.6); see text in Section 3.2 regarding the offsets in different bin internals of Sérsic index.

Table 2.5: $\Delta R_e/R_e$ for Multi-Component Galaxies with Simulated Background – Corrected for Models with n>6

		S/N							
	Subsample	5 – 10	10 – 20	20 – 35	35 – 70	70 – 135	135 – 265	265 – 515	515 – 1000
(1)	(2)	(3)	(4)	(5)	(6)	(7)	(8)	(9)	(10)
R_e	1 – 5	$-0.23^{+1.48}_{-0.60}$	$-0.22^{+0.50}_{-0.30}$	$-0.09^{+0.32}_{-0.32}$	$-0.03^{+0.21}_{-0.30}$	$0.03^{+0.17}_{-0.49}$	$0.03^{+0.08}_{-0.49}$	$0.04^{+0.05}_{-0.45}$	$0.03^{+0.06}_{-0.27}$
	5 – 20	$-0.28^{+0.85}_{-0.40}$	$-0.04^{+0.65}_{-0.40}$	$0.05^{+0.45}_{-0.30}$	$0.12^{+0.27}_{-0.24}$	$0.12^{+0.20}_{-0.17}$	$0.14^{+0.15}_{-0.15}$	$0.11^{+0.15}_{-0.14}$	$0.11^{+0.09}_{-0.10}$
	20 – 70	$-0.03^{+0.91}_{-0.54}$	$0.02^{+0.6}_{-0.43}$	$0.08^{+0.31}_{-0.38}$	$0.11^{+0.23}_{-0.23}$	$0.17^{+0.28}_{-0.23}$	$0.12^{+0.23}_{-0.14}$	$0.20^{+0.21}_{-0.19}$	$0.20^{+0.19}_{-0.19}$
$\langle\mu\rangle$	16 – 21	...	...	...	...	$-0.48^{+0.04}_{-0.07}$	$-0.09^{+0.18}_{-0.40}$	$0.06^{+0.12}_{-0.17}$	$0.09^{+0.11}_{-0.09}$
	21 – 24	$-0.53^{+0.26}_{-0.45}$	$-0.31^{+0.49}_{-0.59}$	$-0.04^{+0.41}_{-0.30}$	$0.07^{+0.26}_{-0.26}$	$0.12^{+0.19}_{-0.18}$	$0.13^{+0.18}_{-0.14}$	$0.17^{+0.20}_{-0.16}$	$0.21^{+0.19}_{-0.21}$
	24– 27	$-0.20^{+1.05}_{-0.46}$	$-0.04^{+0.64}_{-0.39}$	$0.07^{+0.40}_{-0.31}$	$0.13^{+0.28}_{-0.23}$	$0.09^{+0.32}_{-0.17}$	...	...	...
n	0 – 2.5	$-0.55^{+0.32}_{-0.19}$	$-0.37^{+0.25}_{-0.24}$	$-0.27^{+0.22}_{-0.23}$	$-0.29^{+0.24}_{-0.21}$	$-0.21^{+0.12}_{-0.26}$	$-0.19^{+0.12}_{-0.26}$	$-0.17^{+0.06}_{-0.32}$	$-0.12^{+0.10}_{-0.36}$
	2.5 – 6	$-0.12^{+0.58}_{-0.43}$	$-0.03^{+0.49}_{-0.35}$	$0.05^{+0.37}_{-0.26}$	$0.09^{+0.24}_{-0.19}$	$0.13^{+0.17}_{-0.14}$	$0.13^{+0.15}_{-0.10}$	$0.13^{+0.17}_{-0.09}$	$0.11^{+0.12}_{-0.08}$
	6	$0.14^{+1.24}_{-0.81}$	$0.30^{+0.74}_{-0.70}$	$0.21^{+0.38}_{-0.49}$	$0.15^{+0.33}_{-0.45}$	$0.16^{+0.30}_{-0.43}$	$0.13^{+0.25}_{-0.48}$	$0.09^{+0.29}_{-0.50}$	$0.12^{+0.29}_{-0.34}$

The difference between the actual and measured magnitude m for model galaxies rescaled to $z = 2$. Single Sérsic fits with $n > 6$ are refitted by fixing the Sérsic index to $n = 6$.

Col. (1) Parameter.
Col. (2) The subsamples selected based on different ranges of effective radius (R_e), surface brightness ($\langle\mu\rangle$), and Sérsic index (n).
Col. (3-10) Equally (in logarithmic space) spaced intervals of S/N. See text in Section 3.2 regarding the offsets in different Sérsic index.

Table 2.6: Δm_H for Multi-Component Galaxies with Simulated Background – Corrected for Models with n>6

		S/N							
	Subsample	5 – 10	10 – 20	20 – 35	35 – 70	70 – 135	135 – 265	265 – 515	515 – 1000
(1)	(2)	(3)	(4)	(5)	(6)	(7)	(8)	(9)	(10)
R_e	1– 5	$-0.00^{+0.54}_{-0.69}$	$0.10^{+0.32}_{-0.30}$	$0.06^{+0.30}_{-0.20}$	$0.00^{+0.26}_{-0.12}$	$-0.04^{+0.41}_{-0.07}$	$-0.01^{+0.26}_{-0.06}$	$-0.01^{+0.33}_{-0.05}$	$-0.01^{+0.30}_{-0.05}$
	5 – 20	$0.07^{+0.47}_{-0.46}$	$-0.04^{+0.36}_{-0.27}$	$-0.05^{+0.20}_{-0.19}$	$-0.07^{+0.14}_{-0.12}$	$-0.07^{+0.09}_{-0.10}$	$-0.08^{+0.07}_{-0.07}$	$-0.07^{+0.08}_{-0.07}$	$-0.07^{+0.06}_{-0.05}$
	20 – 70	$0.03^{+0.48}_{-0.48}$	$-0.01^{+0.33}_{-0.28}$	$-0.05^{+0.26}_{-0.15}$	$-0.04^{+0.12}_{-0.12}$	$-0.09^{+0.12}_{-0.11}$	$-0.07^{+0.08}_{-0.10}$	$-0.10^{+0.09}_{-0.09}$	$-0.11^{+0.09}_{-0.07}$
$\langle\mu\rangle$	16 – 21	...	...	...	...	$0.38^{+0.07}_{-0.13}$	$0.06^{+0.33}_{-0.13}$	$-0.05^{+0.12}_{-0.05}$	$-0.06^{+0.07}_{-0.06}$
	21 – 24	$0.27^{+0.43}_{-0.28}$	$0.24^{+0.30}_{-0.40}$	$0.02^{+0.27}_{-0.20}$	$-0.05^{+0.16}_{-0.11}$	$-0.07^{+0.10}_{-0.09}$	$-0.08^{+0.07}_{-0.07}$	$-0.09^{+0.08}_{-0.09}$	$-0.11^{+0.10}_{-0.08}$
	24 – 27	$0.04^{+0.48}_{-0.49}$	$-0.02^{+0.33}_{-0.27}$	$-0.05^{+0.22}_{-0.18}$	$-0.07^{+0.13}_{-0.13}$	$-0.07^{+0.10}_{-0.13}$	...	...	...
n	0 – 2.5	$0.40^{+0.35}_{-0.40}$	$0.28^{+0.29}_{-0.25}$	$0.28^{+0.24}_{-0.23}$	$0.28^{+0.32}_{-0.22}$	$0.24^{+0.26}_{-0.17}$	$0.22^{+0.32}_{-0.20}$	$0.20^{+0.37}_{-0.19}$	$0.18^{+0.38}_{-0.17}$
	2.5 – 6	$-0.04^{+0.41}_{-0.34}$	$-0.01^{+0.25}_{-0.24}$	$-0.04^{+0.17}_{-0.18}$	$-0.06^{+0.11}_{-0.11}$	$-0.08^{+0.08}_{-0.08}$	$-0.08^{+0.06}_{-0.07}$	$-0.08^{+0.06}_{-0.07}$	$-0.07^{+0.05}_{-0.06}$
	6	$-0.07^{+0.48}_{-0.57}$	$-0.15^{+0.38}_{-0.28}$	$-0.10^{+0.25}_{-0.16}$	$-0.07^{+0.22}_{-0.13}$	$-0.09^{+0.21}_{-0.12}$	$-0.08^{+0.23}_{-0.09}$	$-0.06^{+0.39}_{-0.12}$	$-0.09^{+0.29}_{-0.08}$

The difference between the actual and measured magnitude m for model galaxies rescaled to $z = 2$. Single Sérsic fits with $n > 6$ are refitted by fixing the Sérsic index to $n = 6$.

Col. (1) Parameter.
Col. (2) The subsamples selected based on different ranges of effective radius (R_e), surface brightness ($\langle\mu\rangle$), and Sérsic index (n).
Col. (3-10) Equally (in logarithmic space) spaced intervals of S/N. See text in Section 3.2 regarding the offsets in different Sérsic index.

CoG technique to measure sizes can produce systematics even in idealized galaxies when $R_e <$ 2 pixels. Even after correcting for this effect, the systematic offsets for galaxies with $1 < R_e <$ 5 pixels are still slightly less than what we find for galaxies with larger sizes. The slight trend and scatter compared to idealized simulations therefore illustrate the fundamental differences due to structural complexities.

Figure 2.8 and Tables 7 and 8 summarize the results of multi-component models with an observed sky background taken from CANDELS UDS H_{160} images. The trends are similar between images with simulated and observed backgrounds. As expected, the uncertainties are higher for images with the observed background, especially at lower S/N.

Under-subtraction or over-subtraction of the sky value can introduce spurious curvature into the brightness profile, especially in the faint, outer regions of the galaxy (e.g., MacArthur et al. 2003; Erwin et al. 2008; Bernardi et al. 2010; Yoon et al. 2011). Figure 2.9 shows the accuracy of `GALFIT` sky determination. It shows that in our simulations `GALFIT` measures the sky value with accuracy better than few 0.01%. Therefore, the systematic errors of single-component fits of multi-component galaxies are not caused by overestimating or underestimating the sky value, but rather merely reflects the limitations of single-component modeling. In fact, even when we fix the sky value to the actual value during the fits, the outcomes do not change.

The provided tables can be used by future observers to quantify potential systematic offsets and uncertainties in their measurements of structural parameters in high-z galaxies. Although the main purpose of the simulations is to determine the robustness of the `GALFIT` modeling of high-z, compact galaxies, our simulations would be appropriate for galaxies of all redshifts, as long as they fall within our S/N, size, Sersic index, and parameter space. Note, however, that the multi-component simulated galaxies mimic the morphology of only early-type galaxies. A forthcoming work (R. Davari et al., in preparation) will address a broader range of morphological types.

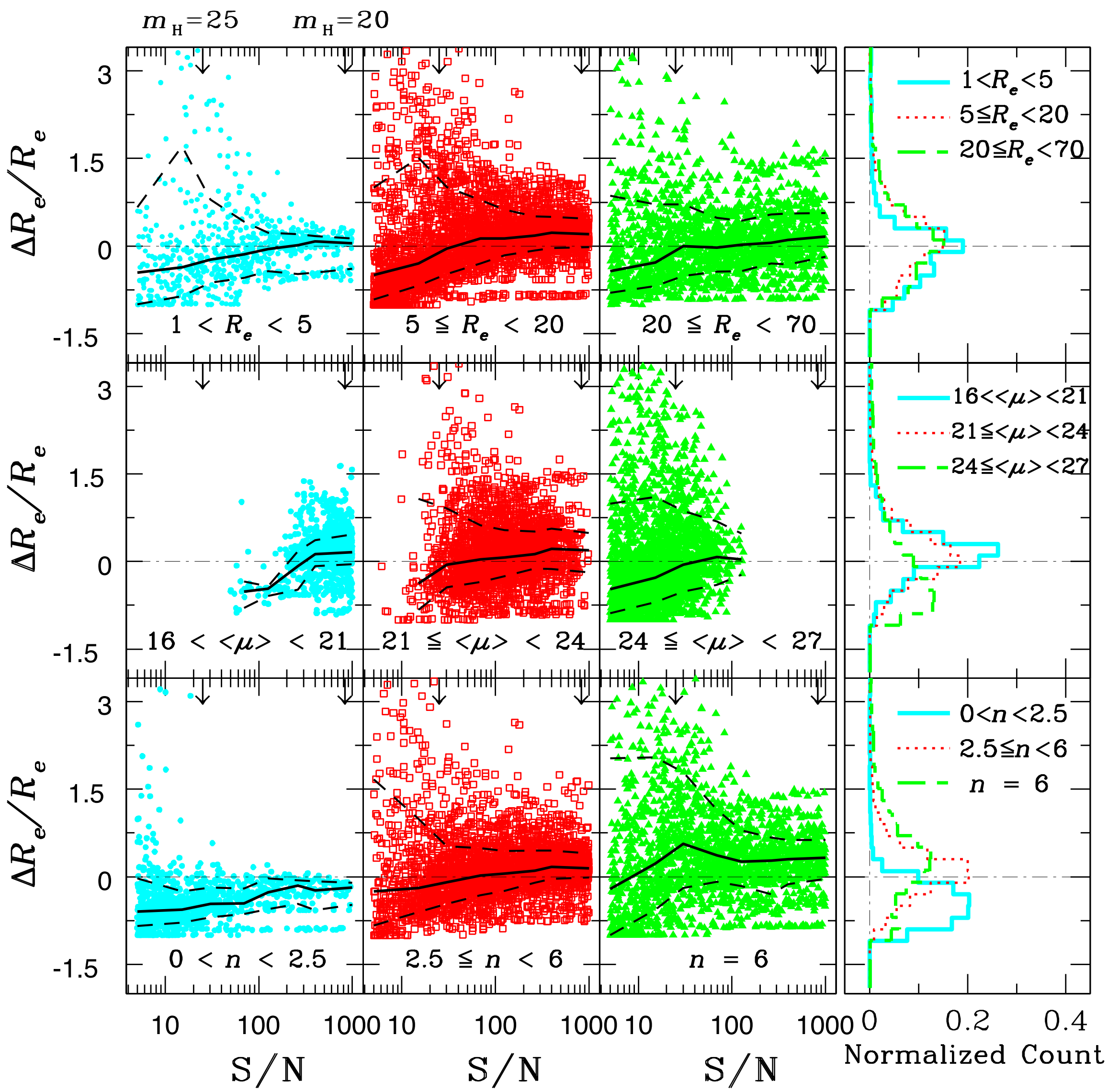

Figure 2.8: Results of more than 7,000 multi-component galaxies with an observed background. The upper, middle, and lower panels show the results at different intervals of size R_e (pixel), mean surface brightness $\langle\mu\rangle$ (m_H arcsec^{-2}), and Sérsic index n, respectively. Black solid and dashed lines in the scatter plots indicate the median and 1σ uncertainties of different measurements. The dot-dash lines show zero offset. The downward-pointing arrows in the scatter plots indicate the S/N of a galaxy with $R_e = 5$ pixels, $e = 0$, and $m_H = 20$ and 25. Galaxies with $n > 6$ are refit by fixing the Sérsic index to $n = 6$. The trends are similar to the results for simulated backgrounds, although the scatter is larger; see text in Section 3.2 regarding the offsets in different bin intervals of Sérsic index.

Table 2.7: $\Delta R_e/R_e$ for Multi-Component Galaxies with Observed Background – Corrected for Models with n>6

		S/N							
	Subsample	5 – 10	10 – 20	20 – 35	35 – 70	70 – 135	135 – 265	265 – 515	515 – 1000
(1)	(2)	(3)	(4)	(5)	(6)	(7)	(8)	(9)	(10)
R_e	1 – 5	$-0.46^{+1.12}_{-0.54}$	$-0.36^{+2.07}_{-0.49}$	$-0.23^{+1.03}_{-0.39}$	$-0.14^{+0.56}_{-0.40}$	$-0.05^{+0.28}_{-0.37}$	$0.02^{+0.19}_{-0.49}$	$0.08^{+0.09}_{-0.53}$	$0.05^{+0.08}_{-0.44}$
	5 – 20	$-0.49^{+1.49}_{-0.42}$	$-0.30^{+1.81}_{-0.38}$	$-0.04^{+1.05}_{-0.44}$	$0.13^{+0.66}_{-0.43}$	$0.13^{+0.49}_{-0.28}$	$0.18^{+0.33}_{-0.25}$	$0.23^{+0.27}_{-0.27}$	$0.21^{+0.26}_{-0.23}$
	20 – 70	$-0.43^{+1.30}_{-0.37}$	$-0.28^{+0.99}_{-0.41}$	$-0.00^{+0.72}_{-0.51}$	$-0.02^{+0.50}_{-0.42}$	$0.03^{+0.41}_{-0.45}$	$0.06^{+0.49}_{-0.35}$	$0.10^{+0.45}_{-0.42}$	$0.16^{+0.41}_{-0.35}$
$\langle\mu\rangle$	16 – 21	...	...	...	$-0.51^{+0.17}_{-0.29}$	$-0.47^{+0.04}_{-0.12}$	$-0.08^{+0.26}_{-0.40}$	$0.13^{+0.23}_{-0.21}$	$0.15^{+0.31}_{-0.20}$
	21 – 24	$-0.86^{+0.77}_{-0.14}$	$-0.38^{+1.45}_{-0.45}$	$-0.05^{+0.96}_{-0.39}$	$0.03^{+0.58}_{-0.39}$	$0.07^{+0.47}_{-0.33}$	$0.12^{+0.39}_{-0.25}$	$0.22^{+0.34}_{-0.35}$	$0.19^{+0.30}_{-0.38}$
	24 – 27	$-0.47^{+1.46}_{-0.41}$	$-0.28^{+1.38}_{-0.42}$	$-0.05^{+0.92}_{-0.46}$	$0.07^{+0.61}_{-0.47}$	$0.04^{+0.44}_{-0.27}$	...	...	...
n	0 – 2.5	$-0.60^{+0.57}_{-0.24}$	$-0.57^{+0.31}_{-0.22}$	$-0.47^{+0.28}_{-0.22}$	$-0.45^{+0.25}_{-0.18}$	$-0.27^{+0.24}_{-0.29}$	$-0.15^{+0.09}_{-0.31}$	$-0.24^{+0.16}_{-0.34}$	$-0.19^{+0.09}_{-0.29}$
	2.5 – 6	$-0.25^{+1.92}_{-0.58}$	$-0.19^{+1.18}_{-0.42}$	$-0.09^{+0.62}_{-0.37}$	$0.02^{+0.47}_{-0.34}$	$0.05^{+0.39}_{-0.29}$	$0.11^{+0.35}_{-0.21}$	$0.17^{+0.28}_{-0.20}$	$0.15^{+0.25}_{-0.16}$
	6	$-0.21^{+2.24}_{-0.79}$	$0.22^{+1.82}_{-0.79}$	$0.56^{+1.23}_{-0.75}$	$0.37^{+0.78}_{-0.45}$	$0.26^{+0.54}_{-0.42}$	$0.27^{+0.40}_{-0.57}$	$0.30^{+0.33}_{-0.43}$	$0.33^{+0.30}_{-0.36}$

The difference between the actual and measured magnitude m for model galaxies rescaled to $z = 2$. Single Sérsic fits with $n > 6$ are refitted by fixing the Sérsic index to $n = 6$.

Col. (1) Parameter.

Col. (2) The subsamples selected based on different ranges of effective radius (R_e), surface brightness ($\langle\mu\rangle$), and Sérsic index (n).

Col. (3-10) Equally (in logarithmic space) spaced intervals of S/N. See text in Section 3.2 regarding the offsets in different Sérsic index.

Table 2.8: Δm_H for Multi-Component Galaxies with Observed Background – Corrected for Models with n>6

		S/N							
	Subsample	5 – 10	10 – 20	20 – 35	35 – 70	70 – 135	135 – 265	265 – 515	515 – 1000
(1)	(2)	(3)	(4)	(5)	(6)	(7)	(8)	(9)	(10)
R_e	1 – 5	$0.04^{+0.78}_{-1.32}$	$0.07^{+0.44}_{-0.96}$	$0.14^{+0.37}_{-0.53}$	$0.05^{+0.37}_{-0.26}$	$0.07^{+0.22}_{-0.22}$	$-0.01^{+0.40}_{-0.11}$	$-0.05^{+0.29}_{-0.06}$	$-0.03^{+0.25}_{-0.06}$
	5 – 20	$0.11^{+0.76}_{-1.09}$	$0.10^{+0.56}_{-0.73}$	$-0.01^{+0.38}_{-0.45}$	$-0.08^{+0.30}_{-0.27}$	$-0.07^{+0.17}_{-0.20}$	$-0.10^{+0.12}_{-0.14}$	$-0.12^{+0.12}_{-0.11}$	$-0.11^{+0.12}_{-0.11}$
	20 – 70	$0.41^{+0.68}_{-0.94}$	$0.23^{+0.55}_{-0.55}$	$0.03^{+0.45}_{-0.35}$	$0.04^{+0.36}_{-0.24}$	$0.01^{+0.37}_{-0.20}$	$-0.02^{+0.23}_{-0.24}$	$-0.04^{+0.27}_{-0.21}$	$-0.09^{+0.23}_{-0.17}$
$\langle\mu\rangle$	16 – 21	...	...	...	$0.39^{+0.19}_{-0.22}$	$0.40^{+0.14}_{-0.15}$	$0.04^{+0.38}_{-0.14}$	$-0.08^{+0.14}_{-0.10}$	$-0.09^{+0.13}_{-0.12}$
	21 – 24	$0.51^{+5.43}_{-0.21}$	$0.28^{+0.38}_{-0.89}$	$-0.00^{+0.38}_{-0.38}$	$-0.02^{+0.29}_{-0.28}$	$-0.03^{+0.23}_{-0.21}$	$-0.07^{+0.15}_{-0.16}$	$-0.11^{+0.18}_{-0.14}$	$-0.10^{+0.26}_{-0.14}$
	24 – 27	$0.16^{+0.76}_{-1.03}$	$0.13^{+0.53}_{-0.69}$	$0.02^{+0.41}_{-0.44}$	$-0.04^{+0.37}_{-0.28}$	$-0.02^{+0.20}_{-0.24}$	...	...	...
n	0 – 2.5	$0.34^{+0.62}_{-0.83}$	$0.48^{+0.42}_{-0.43}$	$0.40^{+0.31}_{-0.31}$	$0.41^{+0.22}_{-0.30}$	$0.24^{+0.33}_{-0.23}$	$0.16^{+0.30}_{-0.14}$	$0.27^{+0.33}_{-0.26}$	$0.22^{+0.36}_{-0.17}$
	2.5 – 6	$-0.02^{+0.79}_{-1.03}$	$0.06^{+0.43}_{-0.60}$	$0.03^{+0.36}_{-0.30}$	$-0.01^{+0.25}_{-0.24}$	$-0.03^{+0.20}_{-0.18}$	$-0.07^{+0.13}_{-0.15}$	$-0.10^{+0.12}_{-0.12}$	$-0.09^{+0.1}_{-0.11}$
	6	$0.02^{+1.00}_{-1.12}$	$-0.16^{+0.54}_{-0.65}$	$-0.24^{+0.41}_{-0.42}$	$-0.17^{+0.22}_{-0.27}$	$-0.12^{+0.20}_{-0.23}$	$-0.11^{+0.23}_{-0.18}$	$-0.13^{+0.18}_{-0.14}$	$-0.15^{+0.16}_{-0.12}$

The difference between the actual and measured magnitude m for model galaxies rescaled to $z = 2$. Single Sérsic fits with $n > 6$ are refitted by fixing the Sérsic index to $n = 6$.

Col. (1) Parameter.

Col. (2) The subsamples selected based on different ranges of effective radius (R_e), surface brightness ($\langle\mu\rangle$), and Sérsic index (n).

Col. (3-10) Equally (in logarithmic space) spaced intervals of S/N. See text in Section 3.2 regarding the offsets in different Sérsic index.

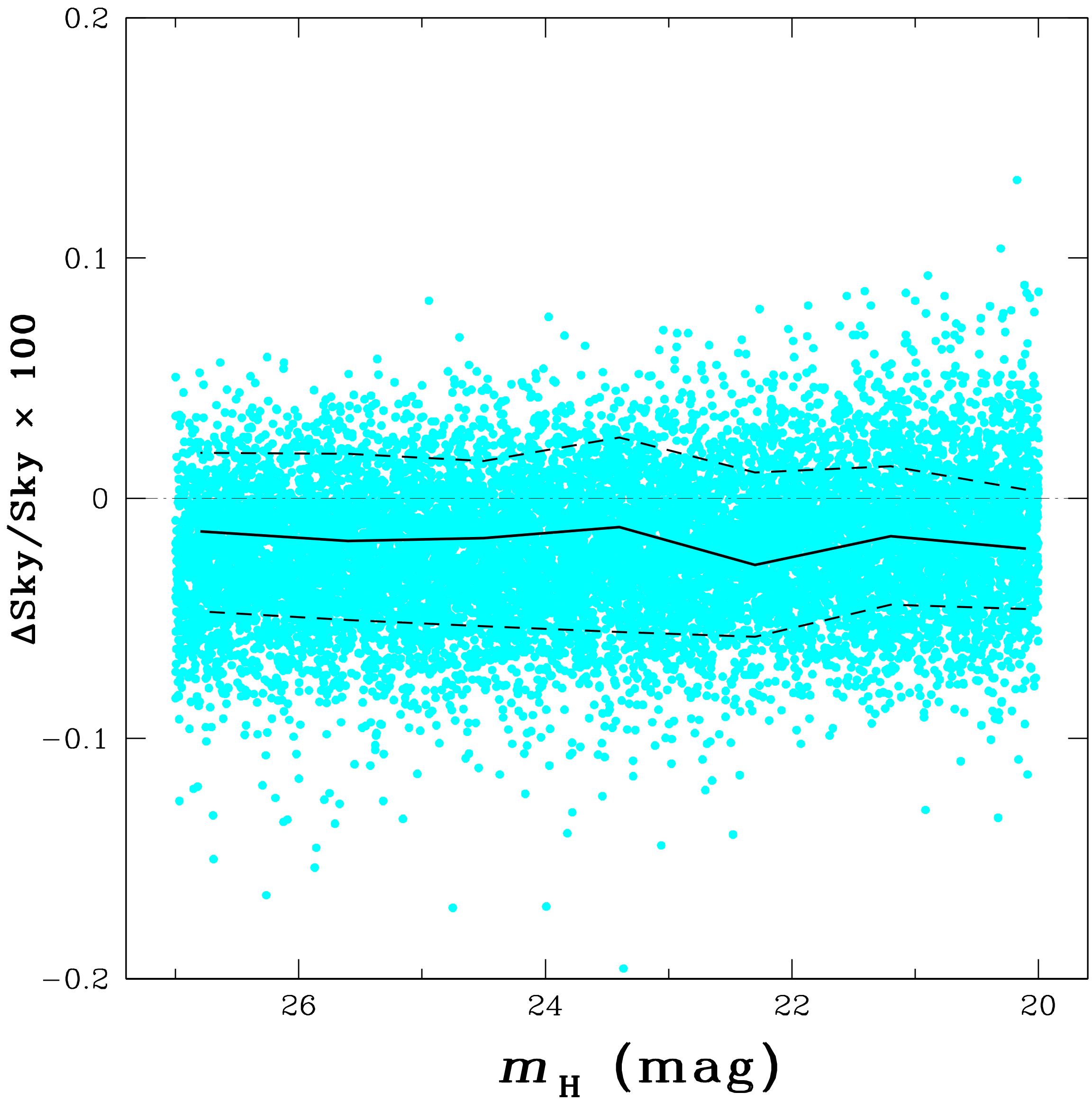

Figure 2.9: Examining the accuracy of GALFIT sky determination. Black solid and dashed lines in the scatter plots indicate the median and 1σ uncertainties of different measurements. The dot-dash line shows zero offset. For our simulations, GALFIT measures the sky value with accuracy better than a few 0.01%.

2.4 The Effects of PSF Accuracy

An important factor in obtaining a best-fit model is the accuracy of the PSF. The effective radii of high-z galaxies are comparable to and in some cases smaller than the FWHM of the PSF. Therefore, one may expect a considerable offset in `GALFIT` measurements when an inaccurate PSF is used (i.e., a PSF with different FWHM and/or different structure than the PSF used for generating the galaxy model). To study this effect, we first generate about 3,000 single-component galaxies with $0.8 < R_e < 4$ pixels, which are convolved with the CANDELS COSMOS H_{160} PSF. Then, we fit each galaxy with the H_{160} PSF from several major *HST* surveys (CANDELS, COSMOS, UDS, GOODS-S, and EGS) and compare the results. The PSFs use a combination of a hybrid TinyTim (Krist et al. 2011) PSF and a stacked empirical stellar PSF. The motivation for constructing such a hybrid PSF is that the TinyTim PSFs are better in the core region (where centroiding issues tend to broaden empirical PSFs), while empirical PSFs fit real stars better in the wings (van der Wel et al. 2012). Figure 2.10 shows that these PSF models have different core sizes (i.e. FWHM) and outer halo wing compared to the COSMOS PSF. The PSF in COSMOS has an intermediate core size.

Figure 2.11 shows that the exact choice of PSF, within the range of realistic PSF models we explored, is not important for the purposes of galaxy size determination. The systematic offsets are less than 2% and the uncertainties are less than 4%. The offsets are smaller for best-fit models with lower Sérsic indices.

2.5 Comparison to Other Studies

Van der Wel et al. (2012) performed comprehensive single-component simulations based on CANDELS imaging in H_{160}, based on their catalog of 6492 objects in GOODS-South. They find that m_H, R_e, and e can be inferred with a random accuracy of 20% or better for galaxies brighter than $m_H = 24.5$, whereas n can be measured at the same level of accuracy for galaxies brighter than $m_H = 23.5$ (their Table 3). They conclude that since a typical faint high-z galaxy is small and has a low Sérsic index, 10%-level accuracy in the single-component measurements

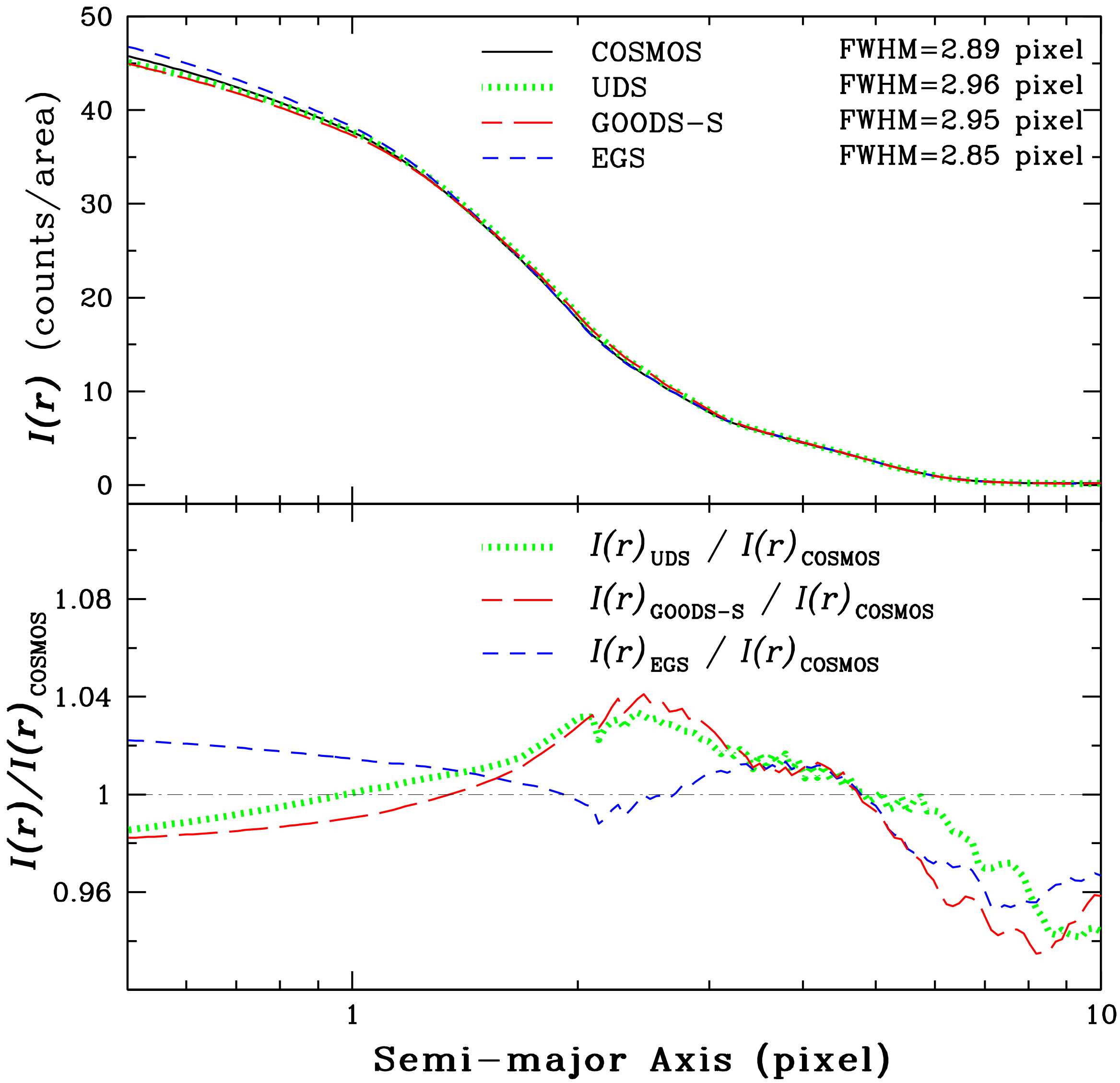

Figure 2.10: CANDELS H_{160} PSF models for different fields. The PSF models are contructed by using TinyTim for the central and outer parts of the PSF and bright stars for intermediate distances from the center. The top panel shows the one-dimensional light profile of different PSF models. The bottom panel shows the differences between the structure of different PSFs. The dot-dash line marks the case when there is no offset.

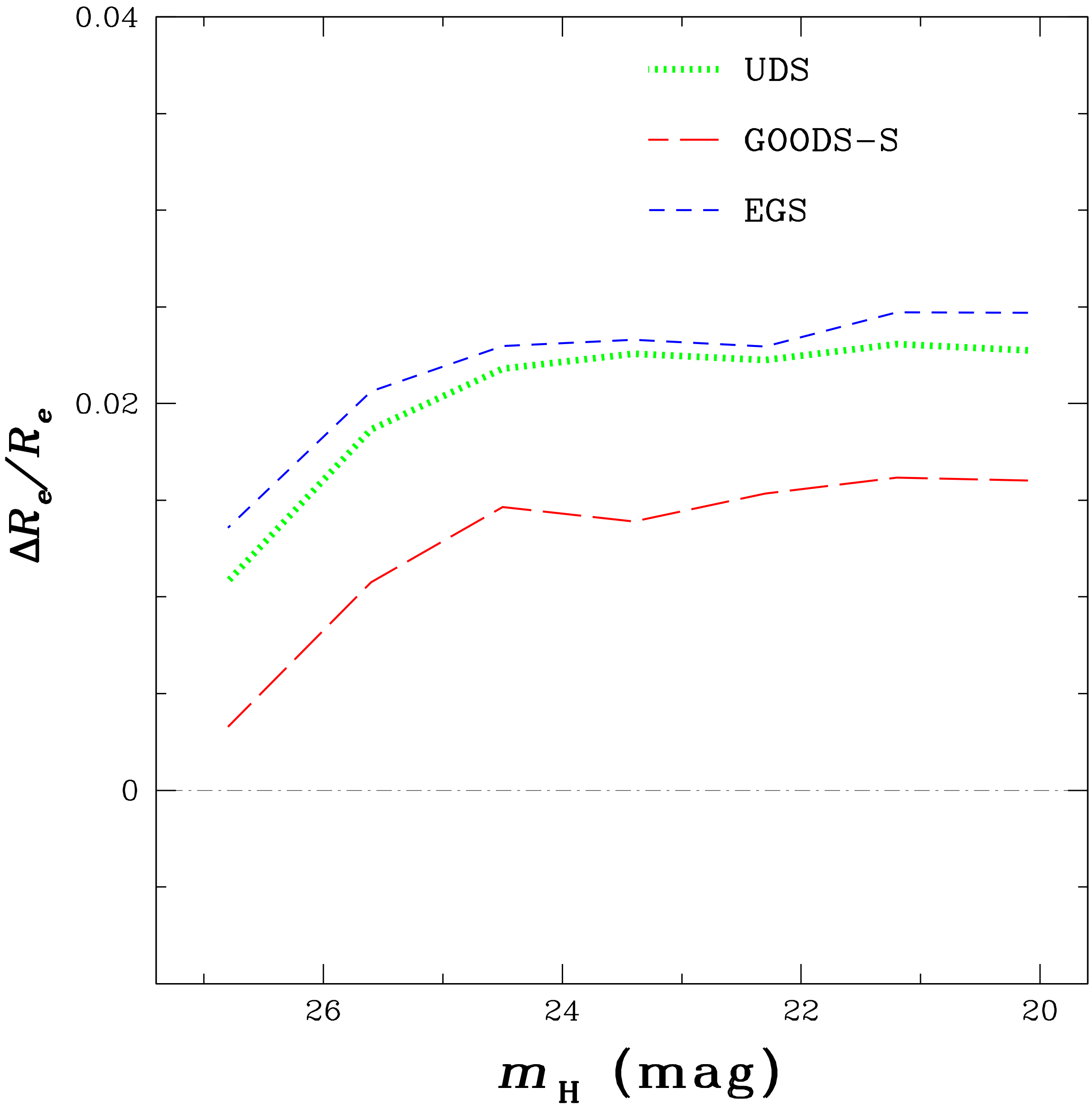

Figure 2.11: Fitting galaxies with PSFs with different structures and/or FWHMs than the intrinsic PSF of the image leads to biases that are insignificant. The systematic offsets for R_e are less than 2%, and the uncertainties are less than 4%. The dot-dash line shows zero offset.

can be reached down to $m_H \approx 24.5$. For their faintest sources ($m_H > 25.5$) with large sizes ($R_e > 0.4''$), the uncertainties in the magnitude and structural parameters start to become substantial because they are dominated by the uncertainty in the background estimate. This is in agreement with our single-component results (Tables 1 and 2). We find that at a specific magnitude the scatter is higher for larger galaxies because their surface brightness is lower.

Trujillo et al. (2007) simulate 1000 single-component galaxies with properties matching the observed distribution of their objects in I_{814}. A background sky, randomly taken from the I_{814} image, is added to the generated galaxies, and the galaxy models are convolved with the observed PSF. Based on their Figure 2, there is no systematic offset for galaxies with $m_I < 24.0$. For fainter galaxies, only those with $n > 2.5$, there is less than a 25% systematic offset toward smaller sizes. They also explore the variation of the PSF within the image to see how it can affect the recovery of the sizes. Using different stars in the image as the PSF, they find that the size estimations are robust to changes in the selected PSF; the scatter is about 10%. Abramson et al. (2013) also use six different PSFs (including an empirical PSF) and find 5%-level accuracy for lower Sérsic indices and 30%-level accuracy for higher Sérsic indices. Our Figure 2.11 confirms that the effects are small when using slightly inaccurate PSFs.

However, Mancini et al. (2010) claim that for objects with large effective radii and Sérsic indices, as elliptical galaxies with masses of $2.5 \times 10^{11} M_\odot$ are expected to be, one could substantially underestimate n and R_e for the typical S/N ($\leq$ 50–100) of their sample. They believe that this reflects the impact of $(1+z)^4$ surface brightness dimming of high-n halos. We do not observe any systematic error in size determination of single-component galaxies with $S/N > 50$ ($m_H < 24$ for typical $z = 2$ galaxies). The sizes of single-component galaxies can be underestimated if the dimension of the image is small relative to the galaxy size. This makes the sky determination less reliable. Size measurements can also be compromised if extended neighbors are not properly masked. However, when these factors are taken into account, we, in agreement with several previous studies (Häussler et al. 2007; van Dokkum & Brammer 2010; Williams et al. 2010; Buitrago et al. 2013), believe that the parameters of a single-component galaxy can be retrieved robustly over a wide range of S/N.

Meert et al. (2013) show that single-component Sérsic fits of two-component (bulge + disk) simulated galaxies, based on a spectroscopically selected sample from the Sloan Digital Sky Survey (SDSS; York et al. 2000; Stoughton et al. 2002), leads to an overestimation of the size (their Figure 8). It holds even for their model galaxies without any noise (their Figure 8*a*). Mosleh et al. (2013) also simulate two-component galaxies based on an SDSS sample. They examine the robustness of size measurements based on non-parametric fitting as well as single- and two-component Sérsic fits. For their modeled galaxies at $z = 0$, they find that their non-parametric and two-component Sérsic fits provide the most robust R_e measurements, while those based on single-component Sérsic fitting often overestimate the size, especially for massive red/early-type galaxies (their Figure 3). Redshifting their galaxies to $z = 1$, they find that the single-Sérsic fitting of two-component galaxies yield reliable size measurements, likely due to the smaller structures being washed out at high redshifts (their Figure 7).

The two-component simulation results of Meert et al. (2013) and Mosleh et al. (2013) qualitatively agree with our results for multi-component galaxies (Figures 6–8). However, Mosleh et al. (2013) finds smaller systematic offsets which could be caused by a considerable fraction of disk-dominated galaxies in their sample. Note that our simulations are limited to early-type galaxies.

2.6 Implications for Red Nuggets

One of the main goals of this study is to examine whether or not there is a bias in measuring properties of the red, massive compact galaxies at $z = 2$. These so-called red nuggets are found to have a median stellar mass $M_* \approx 10^{11}\ M_\odot$ and a median effective radius $R_e \leq 2.0$ kpc (van Dokkum et al. 2008; van der Wel et al. 2011). Red nuggets are found to have $H_{160} < 24$, with a few having $H_{160} = 23$–24 (Szomoru et al. 2012). They are seen at high S/N (≥ 100, for one *HST* orbit).

Assuming that the light distribution of these compact galaxies resembles a Sérsic profile, Figures 2.4 and 2.5 and Tables 1 and 2 show that there is no systematic bias in the size, total luminosity, Sérsic index, and ellipticity of these galaxies. The uncertainties for measuring R_e, m_H, n, and e are less than 20%, 0.2, 0.2, and 10%, respectively, for galaxies with 23 < H_{160} < 24. The uncertainties are much smaller still for brighter galaxies. Thus, provided that red nuggets have Sérsic profiles, single-component fits of these galaxies are very robust.

On the other hand, the observed compact galaxies may have an envelope with low surface brightness that is difficult to recover in detail. If the envelope does not follow a perfect Sérsic function or the overall galaxy profile changes from small to large radii, it is commonly speculated that the envelope flux and hence the true effective radius may be underestimated (e.g., Hopkins et al. 2009). We tackle this problem by taking advantage of H13's morphological study of ∼100 nearby massive elliptical galaxies with median mass $M_\odot = 1.3 \times 10^{11}\ M_\odot$. We directly test the null hypothesis that the red nuggets have undergone no morphological evolution and only passive fading since $z \approx 2$.

Figure 2.7 and Table 5 and 6 show the best-fit results of the single Sérsic fits of the multi-component galaxies. With adequate S/N (≥ 100, comparable to red nuggets studied in CANDELS), the presence of extended envelopes in ellipticals actually leads to a slight *overestimation* of their sizes rather than an underestimation. This holds over a wide range of sizes (i.e., 1 < R_e < 70 pixels). At much lower S/N values (e.g., ≤ 50), the trend reverses but the effect is very modest. Conclusion: if red nuggets have structures similar to local massive elliptical galaxies, single-component Sérsic fits of these galaxies do not underestimate their sizes. The median size of models of nearby ellipticals rescaled to mimic galaxies at $z = 2$ is $R_e \approx 0.5''$, or 4.2 kpc. Considering that the median size of red nuggets is $R_e \approx 1$ kpc, their sizes have increased by a factor of ∼4 if they are the progenitors of local massive ellipticals. Table 6 shows that the total luminosity of the multi-component galaxies can be overestimated as a result of overestimating the size. This leads to systematically higher masses for these compact galaxies. However, this effect is less than 10%, which, compared to other uncertainties involved in mass measurement, is insignificant. Hence, the total luminosity of multi-component galaxies can be measured reliably via single-component Sérsic fitting.

2.7 Summary

Recent observations of galaxies at $z = 2$ with *HST*/WFC3 have revealed a population of red, compact ($R_e \approx 1-2$ kpc), and massive ($M_* \approx 10^{11}\ M_\odot$) galaxies, the so-called red nuggets. We determine the possible biases and uncertainties in the determination of basic structural parameters of these galaxies, with special emphasis on their sizes.

For this purpose, we perform two sets of simulations: one based on idealized single-component models and the other on the observed properties of local massive ellipticals. For the local analogs, we generate galaxies with multiple components (generally three) with the properties obtained from Huang et al. (2013a), which in turn are rescaled so as to compare with galaxies observed at $z = 2.0$. We examine the effects of background noise, the accuracy of the PSF model, and the model fitting method. We analyze the artificial images in a manner similar to that popularly employed in the literature, namely through two-dimensional `GALFIT` modeling of the light distribution using a single-component Sérsic profile and compare the retrieved size, luminosity, and other structural parameters with input values.

We find that:

- If the sky estimation has been done robustly and the PSF model is relatively accurate, `GALFIT` can retrieve the properties of single-component galaxies at a wide range of magnitudes without introducing any systematic error at high accuracy (Figures 2.4 and 2.5 and Tables 1 and 2).

- Modeling multi-component galaxies with a single Sérsic component under realistic conditions does not bias the sizes too low; in fact, sizes tend to be slightly overestimated. This makes the size evolution problem, if anything, even more dramatic. The apparent compactness of red nuggets is real; it is not the result of missing faint, outer light (Figures 2.6–2.8 and Table 5).

- Models with Sérsic indices larger than 6 have larger uncertainties and can cause significant systematic errors. Refitting these galaxies by fixing the Sérsic index to $n = 6$ provides more reliable results (compare Figure 2.6 with Figure 2.7).

- We confirm that massive, compact quiescent galaxies at $z = 2$ are a factor of $\sim$4 smaller than their local counterparts.

Bibliography

Abramson, L. E., Dressler, A., Gladders, M. D., et al. 2013, ApJ, 777, 124

Barden, M., Rix, H.-W., Somerville, R. S., et al. 2005, ApJ, 635, 959

Barden, M., Häußler, B., Peng, C. Y., McIntosh, D. H., & Guo, Y. 2012, MNRAS, 422, 449

Bell, E. F., Wolf, C., Meisenheimer, K., et al. 2004, ApJ, 608, 752

Bernardi, M., Shankar, F., Hyde, J. B., et al. 2010, MNRAS, 404, 2087

Bertin, E., & Arnouts, S. 1996, Supplement Series, 117, 393

Blanton, M. R., Hogg, D. W., Bahcall, N. A., et al. 2003, ApJ, 592, 819

Bruce, V. A., Dunlop, J. S., Cirasuolo, M., et al. 2012, MNRAS, 427, 1666

Buitrago, F., Trujillo, I., Conselice, C. J., et al. 2008, ApJl, 687, L61

Buitrago, F., Trujillo, I., Conselice, C. J., Häussler, B. 2013, MNRAS, 428, 1460

Cassata, P., Giavalisco, M., Guo, Y., et al. 2010, ApJl, 714, L79

Cassata, P., Giavalisco, M., Guo, Y., et al. 2011, ApJ, 743, 96

Cimatti, A., Cassata, P., Pozzetti, L., et al. 2008, Astronomy and Astrophysics, 482, 21

Ciotti, L. 1991, Astronomy and Astrophysics, 249, 99

Conselice, C. J. 1997, Publications of the Astronomical Society of the Pacific, 109, 1251

Daddi, E., Renzini, A., Pirzkal, N., et al. 2005, ApJ, 626, 680

Damjanov, I., McCarthy, P. J., Abraham, R. G., et al. 2009, ApJ, 695, 101

de Vaucouleurs, G. 1948, Annales d'Astrophysique, 11, 247

Erwin, P., Pohlen, M., & Beckman, J. E. 2008, The Astronomical Journal, 135, 20

Fisher, D. B., & Drory, N. 2008, The Astronomical Journal, 136, 773

Franx, M., Labbé, I., Rudnick, G., et al. 2003, ApJl, 587, L79

Franx, M., van Dokkum, P. G., Schreiber, N. M. F., et al. 2008, ApJ, 688, 770

Freeman, K. C. 1970, ApJ, 160, 811

Fruchter, A., Sosey, M., Hack, W., et al. 2009, HST MultiDrizzle Handbook

Graham, A. W., Driver, S. P., Petrosian, V., et al. 2005, The Astronomical Journal, 130, 1535

Grogin, N. A., Kocevski, D. D., Faber, S. M., et al. 2011, ApJl Supp., 197, 35

Häussler, B., McIntosh, D. H., Barden, M., et al. 2007, ApJl Supp., 172, 615

Ho, L. C., Li, Z.-Y., Barth, A. J., Seigar, M. S., & Peng, C. Y. 2011, ApJl Supp., 197, 21

Hogg, D. W., Blanton, M. R., Brinchmann, J., et al. 2004, ApJl, 601, L29

Hopkins, P. F., Bundy, K., Murray, N., et al. 2009, MNRAS, 398, 898

Huang, S., Ho, L. C., Peng, C. Y., Li, Z.-Y., & Barth, A. J. 2013a, ApJ, 766, 47

Huang, S., Ho, L. C., Peng, C. Y., Li, Z.-Y., & Barth, A. J. 2013b, ApJl, 768, L28

Ichikawa, T., Kajisawa, M., & Akhlaghi, M. 2012, MNRAS, 422, 1014

Jedrzejewski, R. I. 1987, MNRAS, 226, 747

Koekemoer, A. M., Faber, S. M., Ferguson, H. C., et al. 2011, ApJl Supp., 197, 36

Kriek, M., van Dokkum, P. G., Franx, M., et al. 2006, ApJl, 649, L71

Krist, J. E., Hook, R. N., & Stoehr, F. 2011, SPIE, 8127, 16

Lawrence, A., Warren, S. J., Almaini, O., et al. 2007, MNRAS, 379, 1599

Lotz, J. M., Primack, J., & Madau, P. 2004, The Astronomical Journal, 128, 163

MacArthur, L. A., Courteau, S., & Holtzman, J. A. 2003, ApJ, 582, 689

Mancini, C., Daddi, E., Renzini, A., et al. 2010, MNRAS, 401, 933

McIntosh, D. H., Bell, E. F., Rix, H.-W., et al. 2005, ApJ, 632, 191

Meert, A., Vikram, V., & Bernardi, M. 2013, MNRAS, 433, 1344

Mosleh, M., Williams, R. J., & Franx, M. 2013, ApJ, 777, 117

Muzzin, A., van Dokkum, P., Franx, M., et al. 2009, ApJl, 706, L188

Newman, A. B., Ellis, R. S., Bundy, K., & Treu, T. 2012, ApJ, 746, 162

Oser, L., Naab, T., Ostriker, J. P., & Johansson, P. H. 2012, ApJ, 744, 63

Papovich, C., Bassett, R., Lotz, J. M., et al. 2012, ApJ, 750, 93

Peng, C. Y., Ho, L. C., Impey, C. D., & Rix, H.-W. 2002, The Astronomical Journal, 124, 266

Peng, C. Y., Ho, L. C., Impey, C. D., & Rix, H.-W. 2010, The Astronomical Journal, 139, 2097

Poggianti, B. M., Calvi, R., Bindoni, D., et al. 2013, ApJ, 762, 77

Ravindranath, S., Ferguson, H. C., Conselice, C., et al. 2004, ApJl, 604, L9

Saracco, P., Longhetti, M., & Gargiulo, A. 2010, MNRAS, 408, L21

Shen, S., Mo, H. J., White, S. D. M., et al. 2003, MNRAS, 343, 978

Simard, L., & Pritchet, C. J. 1998, ApJ, 505, 96

Simard, L., Willmer, C. N. A., Vogt, N. P., et al. 2002, ApJl Supp., 142, 1

Simard, L., Mendel, J. T., Patton, D. R., Ellison, S. L., & McConnachie, A. W. 2011, ApJl Supp., 196, 11

Stoughton, C., Lupton, R. H., Bernardi, M., et al. 2002, The Astronomical Journal, 123, 485

Szomoru, D., Franx, M., van Dokkum, P. G., et al. 2010, ApJl, 714, L244

Szomoru, D., Franx, M., & van Dokkum, P. G. 2012, ApJ, 749, 121

Taylor, E. N., Franx, M., Glazebrook, K., et al. 2010, ApJ, 720, 723

Tody, D. 1986, SPIE, 627, 733

Tody, D. 1993, Astronomical Society of the Pacific Conference Series, 52, 173

Toft, S., van Dokkum, P., Franx, M., et al. 2007, ApJ, 671, 285

Trujillo, I., Conselice, C. J., Bundy, K., et al. 2007, MNRAS, 382, 109

Trujillo, I., Cenarro, A. J., de Lorenzo-Cáceres, A., et al. 2009, ApJl, 692, L118

Valentinuzzi, T., Fritz, J., Poggianti, B. M., et al. 2010, ApJ, 712, 226

van der Wel, A., Holden, B. P., Zirm, A. W., et al. 2008, ApJ, 688, 48

van der Wel, A., Rix, H.-W., Wuyts, S., et al. 2011, ApJ, 730, 38

van der Wel, A., Bell, E. F., Häussler, B., et al. 2012, ApJl Supp., 203, 24 van Dokkum, P. G., Franx, M., Kriek, M., et al. 2008, ApJl, 677, L5

van Dokkum, P. G., & Brammer, G. 2010, ApJl, 718, L73

Williams, R. J., Quadri, R. F., Franx, M., et al. 2010, ApJ, 713, 738

Wuyts, S., Cox, T. J., Hayward, C. C., et al. 2010, ApJ, 722, 1666

Yoon, I., Weinberg, M. D., & Katz, N. 2011, MNRAS, 414, 1625

York, D. G., Adelman, J., Anderson, Jr., J. E., et al. 2000, The Astronomical Journal, 120, 1579

Chapter 3

On the limits of measuring the bulge and disk properties of local and high-redshift massive galaxies

Abstract

A considerable fraction of the massive quiescent galaxies at $z \approx 2$, which are known to be much more compact than galaxies of comparable mass today, appear to have a disk. How well can we measure the bulge and disk properties of these systems? We simulate two-component model galaxies in order to systematically quantify the effects of non-homology in structures and the methods employed We employ empirical scaling relations to produce realistic-looking local galaxies with a uniform and wide range of bulge-to-total ratios (B/T), and then rescale them to mimic the signal-to-noise ratios and sizes of observed galaxies at $z \approx 2$. This provides the first set of simulations for which we can examine the robustness of two-component decomposition of compact disk galaxies at different B/T. We confirm that the size of these massive, compact galaxies can be measured robustly using a single Sérsic fit. We can measure B/T accurately without imposing any constraints on the light profile shape of the bulge, but, due to the small angular sizes of bulges at high redshift, their detailed properties can only be recovered

for galaxies with $B/T \gtrsim 0.2$. The disk component, by contrast, can be measured with little difficulty.

3.1 Introduction

Discovery of compact, red massive galaxies at $z \approx 2$ (e.g., Franx et al. 2003; Daddi et al. 2005; Kriek et al. 2006) have opened a new door for improving the current models of galaxy formation and evolution (e.g., Wuyts et al. 2010; Oser et al. 2012; Ishibashi et al. 2013; Dekel & Burkert 2014). Several studies have confirmed the compactness of these galaxies (e.g., Daddi et al. 2005; Toft et al. 2007; Trujillo et al. 2007; Buitrago et al. 2008; Cimatti et al. 2008; Franx et al. 2008; van der Wel et al. 2008; van Dokkum et al. 2008; Damjanov et al. 2009; Hopkins et al. 2009; Cassata et al. 2010, 2011; Mancini et al. 2010; Newman et al. 2012; Szomoru et al. 2012; Barro et al. 2013; Huang et al. 2013; Williams et al. 2014). These "red nuggets," while so common at $z \approx 2$, are rare in the local universe, which implies a considerable size increase (3 – 4 times) in the last 10 billion years (van Dokkum et al. 2008; Trujillo et al. 2009; Taylor et al. 2010; van Dokkum & Brammer 2010; but see Saracco et al. 2010; Valentinuzzi et al. 2010; Ichikawa et al. 2012; Poggianti et al. 2013). Red nuggets are found to be as compact as $\sim 1 - 2$ kpc, which is comparable to the size of the *Hubble Space Telescope (HST)* point-spread function (PSF). This raises the concern that the size and mass measurements of these galaxies are subject to potential uncertainties (Hopkins et al. 2009; Muzzin et al. 2009).

Besides the small size of the red nuggets, at least a considerable fraction of them are found to have a disk, which imposes a further challenge to our paradigm of galaxy evolution. Van der Wel et al. (2011) claim that more than 50% of the population of massive quiescent galaxies at $z > 2$ are disk-dominated. Chang et al. (2013), by deprojecting the observed axial ratios of the galaxies in their sample, show that early-type galaxies at $z > 1$ are, on average, flatter than their counterparts at $z < 1$. Furthermore, they claim that the median projected axis ratio at a fixed mass decreases with redshift, which hints at the prevalence of disks at higher redshifts. Patel et al. (2013) find that their sample of quiescent massive galaxies at higher redshifts have lower axial ratios (b/a) and concluded that the stars in the progenitors of today's $2M^{\star}$ galaxies were distributed in disks at $z \approx 3$. Bruce et al. (2014) show that within the redshift interval $1 < z < 3$ most massive galaxies are morphologically composite systems containing both a bulge and a disk component. More than 80% of their sample require a disk component to properly fit their light distribution. Aside from the observational evidence of the prevalence of disks among the most massive galaxies at high redshift, cosmological simulations predict the formation of massive disk galaxies at these epochs. The compactness of red nuggets indicates that these galaxies have experienced severe dissipation during their formation. One plausible scenario is that the red nuggets are the end result of major gas-rich mergers. Robertson et al. (2006) find that nearly all their simulated gas-rich merger remnants contain rapidly rotating stellar substructure, while disk-dominated remnants are restricted to form in mergers that are gas-dominated at the time of final coalescence. They show that the formation of rotationally supported stellar systems in mergers is not restricted to idealized orbits, and both gas-rich major and minor mergers can produce disk-dominated stellar remnants. Their findings can be especially important for galaxy formation at high redshifts, where gas-dominated mergers are common.

Measuring the bulge and disk properties, and subsequently the luminosity bulge-to-total ratio (B/T), of galaxies obviously can reveal key properties and clues to formation and evolutionary paths that may be obscured by studying a bulge+disk galaxy as a single system. Several factors can affect the reliability of bulge-disk decomposition, including how the fitting pipeline is employed, the galaxy brightness [signal-to-noise ratio (S/N)], cosmological surface brightness dimming, and the effect of the PSF. One of the best ways for quantifying the influence of these factors is through galaxy simulations (e.g., Trujillo et al. 2007, Cimatti et al. 2008, Mancini et al. 2010, Szomoru et al. 2010, 2012, van Dokkum & Brammer 2010, Williams et al. 2010, Papovich et al. 2012, van der Wel et al. 2012, and Davari et al. 2014 for high-z galaxies, and Häussler et al. 2007 and Meert et al. 2013 for low-z galaxies).

This work employs well-tested properties and scaling relations of local galaxies to generate mock bulge+disk galaxies with a uniform and wide range of B/T. This provides the first set of simulations that allows us to examine the robustness of two-component decomposition of disk galaxies at different B/T values. Although our model bulge+disk galaxies do not capture the full observed complexity of local disk galaxies (e.g., Gadotti 2009; Kormendy & Barentine 2010), recent zoom-in cosmological simulations find that galaxies with bars and spiral structures are rare at $z \approx 2$ (Kraljic et al. 2012). If higher redshift bulges and disks resemble their local counterparts, the results of our rescaled model galaxies can be used as a yardstick for examining the robustness of these types of analysis for higher redshift galaxies. We address three key questions:

1) How well can single-component fitting of bulge+disk galaxies measure the global size and total luminosity of these galaxies?

2) Can we recover the properties of both the bulge and disk components, and if so, how well?

3) What are the best methods for measuring the B/T of composite galaxies? And what are the potential biases of different bulge-disk fitting methods?

This paper is organized as follows. In Section 2, the details of the galaxy simulations are provided. The main results are presented in Section 3. Comparison with similars studies is done in Section 4. In Section 5, implications of our results for red nuggets are discussed, and a summary is listed in Section 6. Results are based on a standard cosmology ($H_0 = 71$ $\mathrm{km}^{-1}\,\mathrm{s}^{-1}\,\mathrm{Mpc}^{-1}$, $\Omega_m = 0.27$, and $\Omega_\Lambda = 0.73$) and AB magnitudes.

3.2 Method

3.2.1 Technique

`GALFIT 3.0` (Peng et al. 2010) is utilized for our simulations. `GALFIT` is used extensively for modeling the light profiles of galaxies. It provides several commonly used functions in astronomical literature. For our applications, we only use the Sérsic (1968) function to model the surface brightness profiles:

$$\Sigma(R) = \Sigma_e \, exp\left\{-\kappa\left[\left(\frac{R}{R_e}\right)^{1/n} - 1\right]\right\}, \tag{3.1}$$

where R_e is the effective radius of the galaxy, Σ_e is the surface brightness at R_e, the Sérsic index n describes the profile shape, and the parameter κ is closely connected to n (Ciotti 1991). The special cases of the Sérsic profile are the exponential profile ($n = 1$; Freeman 1970) and the $R^{1/4}$ law ($n = 4$; de Vaucouleurs 1948), which are commonly observed in spiral and elliptical galaxies, respectively. This suggests that the Sérsic index can be used as a yardstick for distinguishing the disk-dominated from the bulge-dominated galaxies (e.g., Blanton et al. 2003; Shen et al. 2003; Bell et al. 2004; Hogg et al. 2004; Ravindranath et al. 2004; Barden et al. 2005; McIntosh et al. 2005; Fisher & Drory 2008).

3.2.2 Simulated Model Galaxies

We aim to simulate galaxies that resemble real, observed disk galaxies. Toward this goal, we use empirical scaling relations and other empirical constraints derived from observations of nearby galaxies as inputs to create the model galaxies. Although these constraints reduce the generality of our simulated sample, they provide us with simulated galaxies that exhibit realistic values of bulge and disk component parameters.

The well-known Kormendy relation (Kormendy 1977; Hamabe & Kormendy 1987), a projection of the galaxy fundamental plane (Djorgovski & Davis 1987; Dressler et al. 1987), reveals that elliptical galaxies and classical bulges follow a correlation between effective surface brightness (μ_e) and effective radius (R_e). The Kormendy relation indicates that larger elliptical galaxies and classical bulges have lower densities. Since brighter galaxies are bigger, a more general statement is that more luminous systems are fluffier. The Kormendy relation, which has played an important role in the study of the formation and evolution of galaxies, has been studied in different bands (e.g., La Barbera et al. 2010), environments (e.g., Nigoche-Netro et al. 2007), redshifts (e.g., La Barbera et al. 2003; Longhetti et al. 2007), and magnitude ranges (Nigoche-Netro et al. 2008).

Our simulated images of fiducial local ($z \approx 0$) galaxies will be designed to mimic Sloan Digital Sky Survey (SDSS; York et al. 2000; Stoughton et al. 2002) images taken in the g band. Using the V-band Kormendy relation of (Hamabe & Kormendy, 1987) and assuming $g - V \approx 0.5$ for E/S0 galaxies (Fukugita et al. 1995), our simulated bulges follow

$$\mu_e = 3.0 \ \log(R_e) + 20, \tag{3.2}$$

where R_e is expressed in Kpc and μ_e in mag arcsec^{-2} (Fig. 3.1d).

The disks of late-type galaxies display a correlation between their central surface brightness (μ_0) and scale length (h) (e.g., Graham & Worley 2008; Gadotti 2009; Laurikainen et al. 2010). This relation has a similar trend as the Kormendy relation, but with a different slope. We use the SDSS g-band catalog of Gadotti (2009) to quantify this correlation, so that our simulated disks follow

$$\mu_0 = 3.5 \ \log(h) + 19.75, \tag{3.3}$$

where h is expressed in Kpc and μ_0 in mag arcsec^{-2}. The analysis of Laurikainen et al. (2010), done in the K_s band, shows a similar slope for this disk scaling relation (Fig. 3.2b). Another constraint that we employ is the observed structural coupling between the bulge and disk sizes (Courteau et al. 1996; de Jong 1996), one that has been interpreted to indicate that the formation of the disk and bulge are related as a result of secular evolution. MacArthur et al. (2003) find $\langle R_e/h \rangle \approx 0.25$, independent of wavelength but with a mild trend with Hubble type: more bulge-dominated galaxies have larger R_e/h. Based on the observed distribution of R_e/h (MacArthur et al. 2003, their Fig. 21), we constrain our simulated galaxies to have $0.05 < R_e/h < 0.6$.

The simulated disk component follows the exponential light profile (Freeman 1970). On the other hand, the Sérsic indices (Sérsic 1968) of bulges correlate with their total luminosity (Fisher & Drory 2008; Graham & Worley 2008; Laurikainen et al. 2010). Using Equation 17 of Graham & Worley (2008), which is given in the B band, we assume $g - B = -0.7$ (appropriate for Sab galaxies; Fukugita et al. 1995) to obtain

$$n = 10^{-(15+M_g)/9.4}, \tag{3.4}$$

where M_g is the absolute g-band magnitude (Fig. 3.1h). The ellipticity, $e = 1 - b/a$, of bulges have a Gaussian distribution that peaks around 0.2 (Fathi et al. 2003), whereas disks, as a result of different inclination angles, have $e < 0.8$ (Ryden 2006). We assume disks and bulges have random orientations (position angles). The simulated disks have a Gaussian distribution of central surface brightness, with a mean and standard deviation of $\mu_0 = 21 \pm 0.3$ mag arcsec^{-2} (Gadotti 2009).

These initial conditions lead to a sample of model galaxies with to $0.1 < B/T < 0.7$, with the majority of the objects having $0.25 < B/T < 0.5$. There are more than 500 galaxies in each of the following bins of B/T: <0.2, 0.2–0.3, 0.4–0.3, 0.4–0.5, 0.5–0.6, and >0.6. This produces bulges with $R_e \approx 0.4''$–$5''$ (1–12 pixels) and disks with $h \approx 3.5''$–$10''$(9–25 pixels). In this paper, the analyzed effective radii are circularized effective radii, $R_{e,\mathrm{circularized}} \equiv R_{e,\mathrm{GALFIT}} \times \sqrt{1-e}$; the same applies to the disk scale lengths. Figures 3.1 and 3.2 show the properties of the simulated bulges and disks. Figure 3.2f shows that galaxies with the smallest B/T have the lowest R_e/h, in agreement with previous studies (e.g., MacArthur et al. 2003; Fisher & Drory 2008).

To obtain a robust determination of the sky background, the size of the simulated images should be at least 15 times larger than the effective radius of the galaxy (Yoon et al. 2011; Huang et al. 2013a). As the simulated images are meant to resemble SDSS data, the pixel scale is set to $0.396''$, and the zero point of the images is set to 25 mag, typical for the SDSS g band[1]. We convolve the simulated images with an empirical PSF constructed by stacking 30 bright stars selected from SDSS g-band images.

S/N is a key factor for the robustness of morphological analysis. Considering the fact that galaxies are extended objects, we use the S/N within the effective radius rather than the total S/N. We define

[1] http://www.sdss.org/dr7/algorithms/fluxcal.html

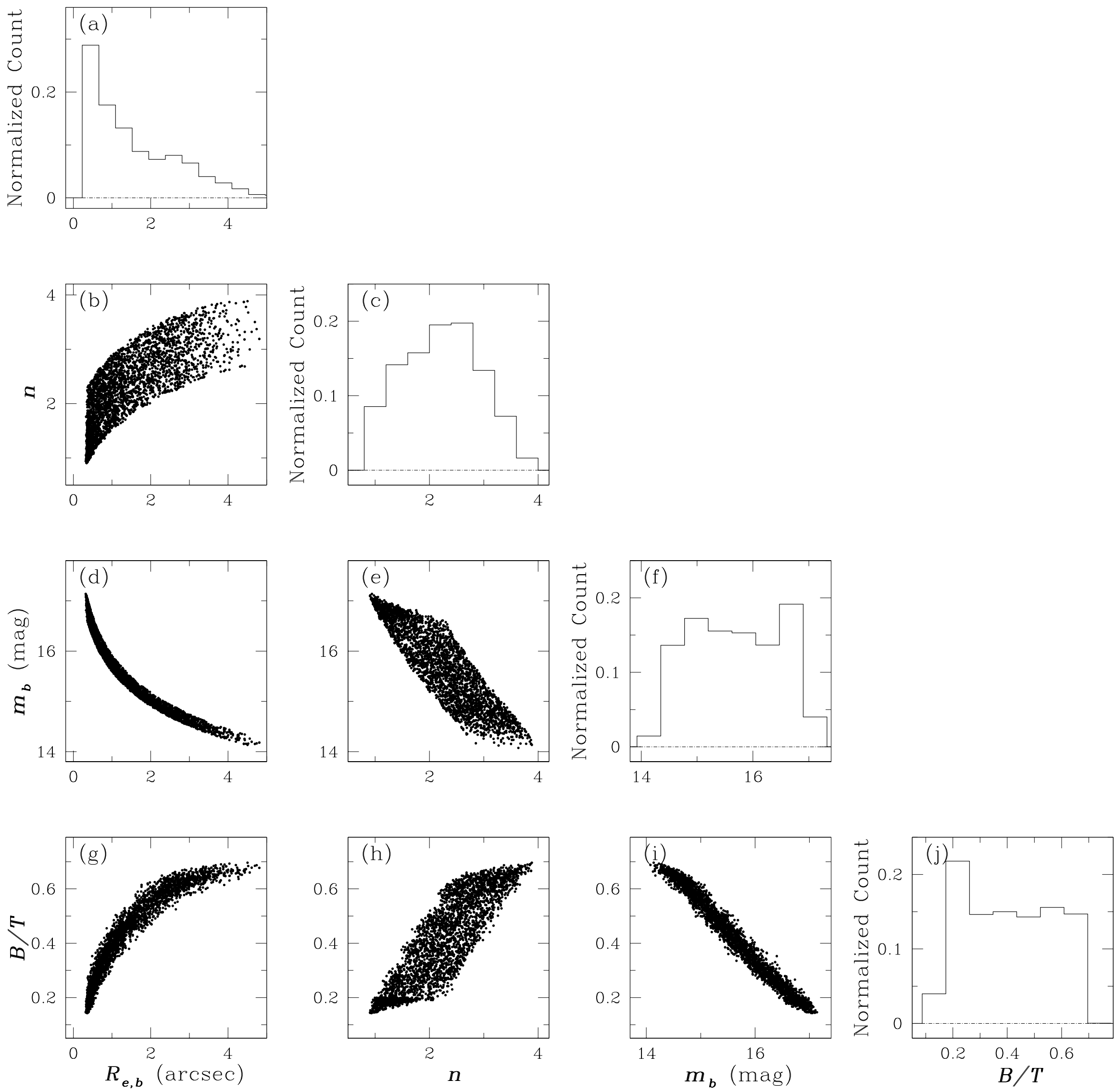

Figure 3.1: Properties of more than 2,000 simulated bulges rescaled to $z = 0.02$ ($\sim$100 Mpc). Simulated galaxies have uniform distribution of B/T in four bins (<0.2, 0.2–0.4, 0.4–0.6, and >0.6). The correlation between magnitude (m_B) and effective radius (R_e) shown in panel (d) indicates that bulges follow the Kormendy relation (Equation 3.2). Smaller bulges are less luminous, and therefore galaxies with the smallest B/T have the smallest bulges (panel g). Panel (h) shows that the Sérsic indices of bulges correlate with their total luminosity (Equation 3.4).

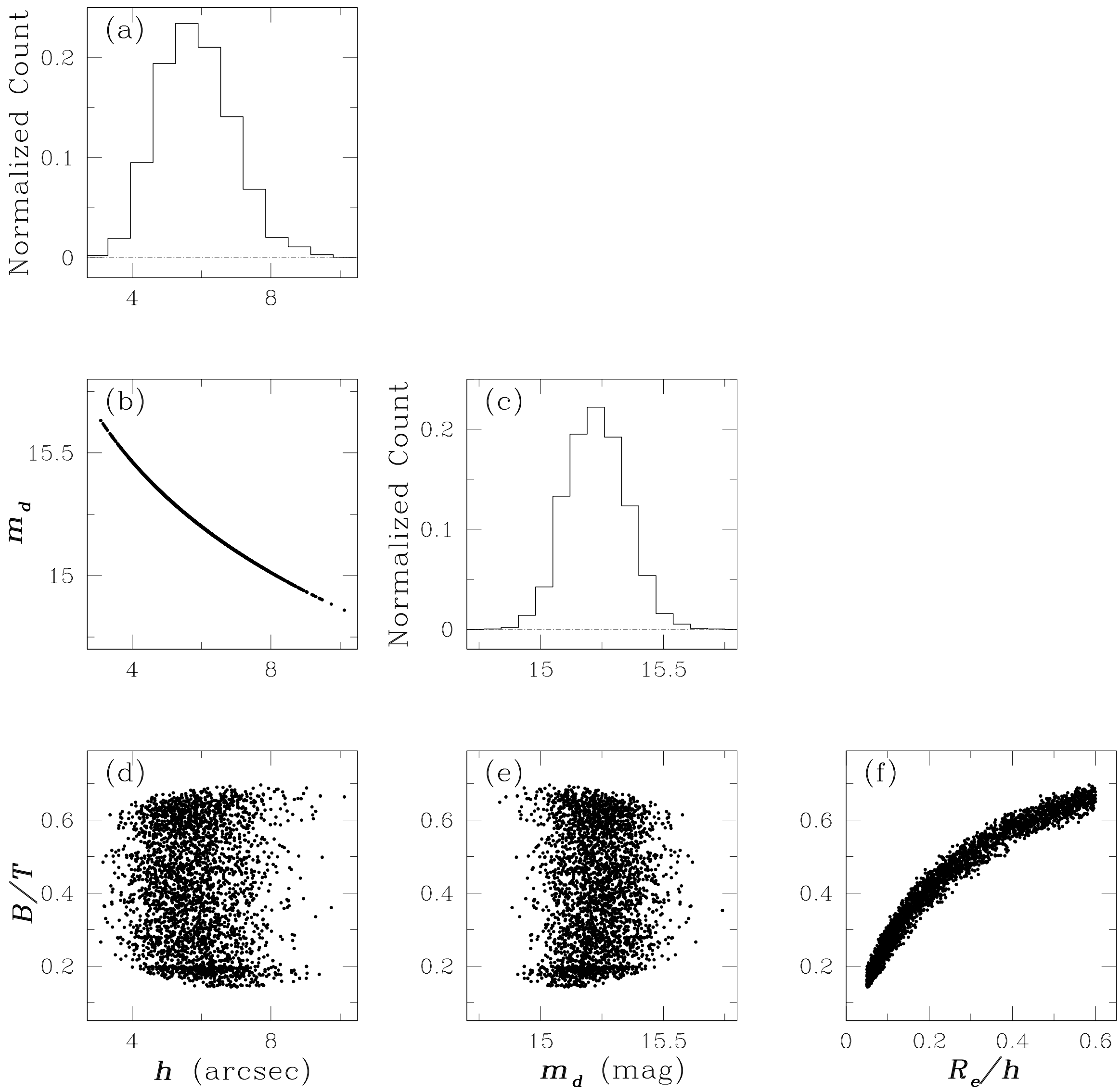

Figure 3.2: Properties of more than 2,000 simulated disks rescaled to $z = 0.02$ ($\sim$100 Mpc). Simulated galaxies have uniform distribution of B/T in four bins (<0.2, 0.2–0.4, 0.4–0.6, and >0.6). The correlation between magnitude (m_d) and the disk scale length (h) demonstrates the scaling relation between the central surface brightness of the disk and its scale length (Equation 3.3). Panel (f) shows that galaxies with lowest B/T have the smallest R_e/h, in agreement with previous studies.

$$S/N = \frac{f_{\rm galaxy}}{\sqrt{f_{\rm galaxy} + A\sigma^2}}, \quad (3.5)$$

where A is the area within the effective radius and σ is the sum of all possible sources of noise, including dark current, readout noise, and shot noise from the sky.

For each model galaxy, we generate 10 images with different noise levels over the range 100 <S/N< 10000; the S/N values are uniformly distributed in logarithmic space. In total, we generate more than 5000 images in each B/T bin, and more than 30,000 over the whole range of B/T. For the typical noise level and exposure time of SDSS images, the above range of S/N values corresponds to simulated galaxies with $8.5 < m_g < 18.5$.

Figure 3.3 shows simulated disk galaxies with four different values of B/T and three inclination angles. Figure 3.4 gives an example of a simulated galaxy with $B/T \approx 0.3$ at three different levels of S/N, which correspond to $m_g \approx 18$, 13.5, and 9 mag, and three inclination angles. Objects with low S/N look like compact galaxies due to the missing light in the outer part of the disk.

One of the main goals of this paper is to examine the reliability of model fits of high-redshift massive galaxies using one or two Sérsic components. These high-redshift galaxies are generally smaller than local galaxies, have been observed at lower S/N, and have been subject to surface brightness dimming. Therefore, we rescale the sizes and S/N of model local galaxies to mimic galaxies at $z \approx 2$. This leads to simulated galaxies with bulges with $0.02''$ $< R_e < 0.25''$ 0.3–4 pixels) and disks with $0.17'' < h < 0.5''$ (3–8 pixels). The rescaled model galaxies are simulated at 10 <S/N< 1000 (uniformly distributed in logarithmic space), and their images mimic the properties of the CANDELS[2] (Grogin et al. 2011; Koekemoer et al. 2011) UDS (UKIDSS Ultra-Deep Survey; Lawrence et al. 2007) mosaic image. For images with the noise level of those acquired using *HST*'s Wide Field Camera 3 (WFC3) in the H_{160} filter (Koekemoer et al. 2011), this range of S/N for the rescaled model galaxies is equivalent to galaxies with $18.5 < H_{160} < 28.5$ observed for one orbit with the *HST*. The simulated images are convolved with the hybrid H_{160} PSF from CANDELS UDS (van der Wel et al. 2012).

[2] `http://candels.ucolick.org/`

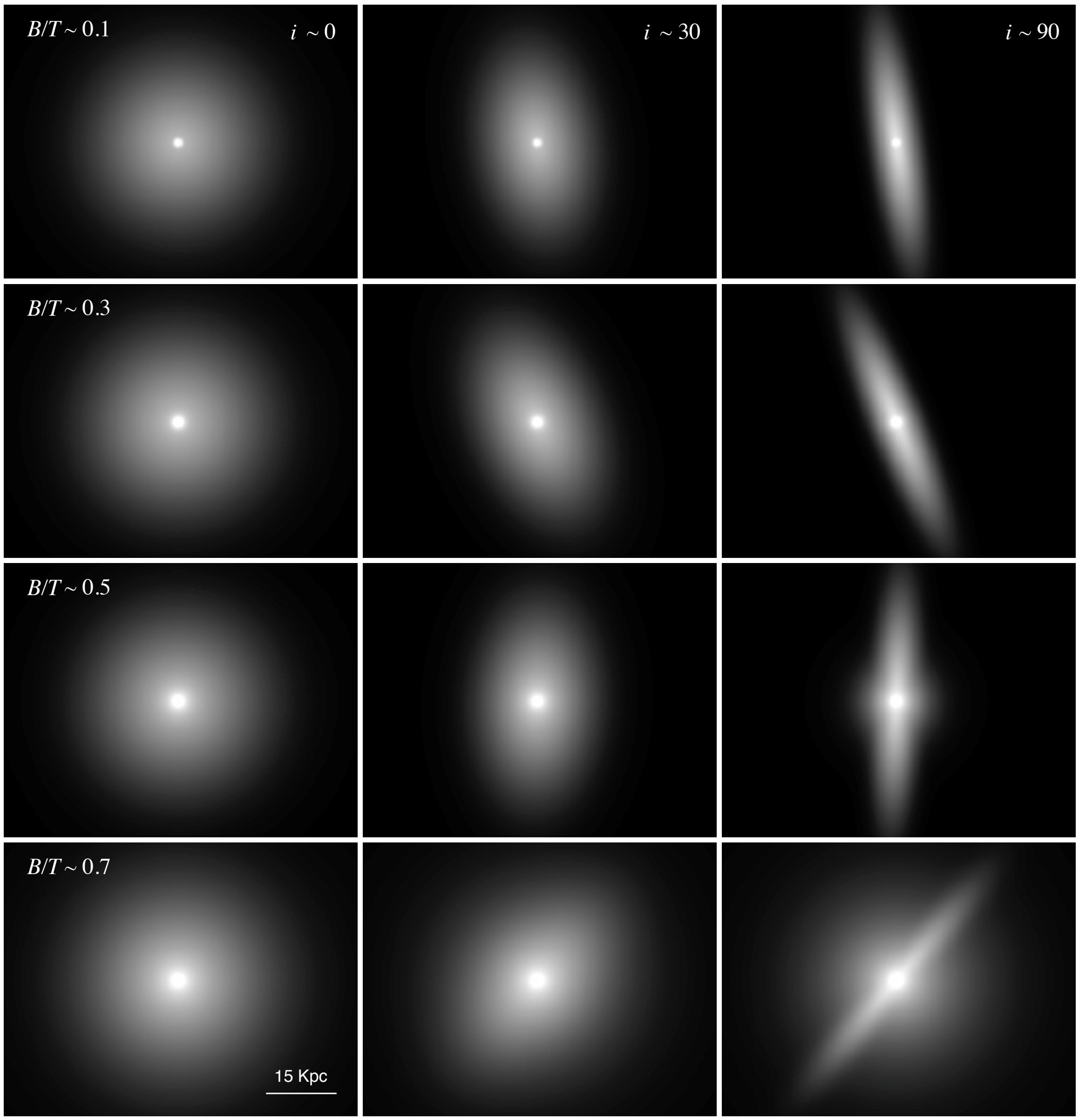

Figure 3.3: Simulated disk galaxies at four different values of B/T and three inclination angles i. No noise has been added to these images. The solid line in the lower left panel shows a scale of 15 Kpc. The simulated images mimic SDSS data.

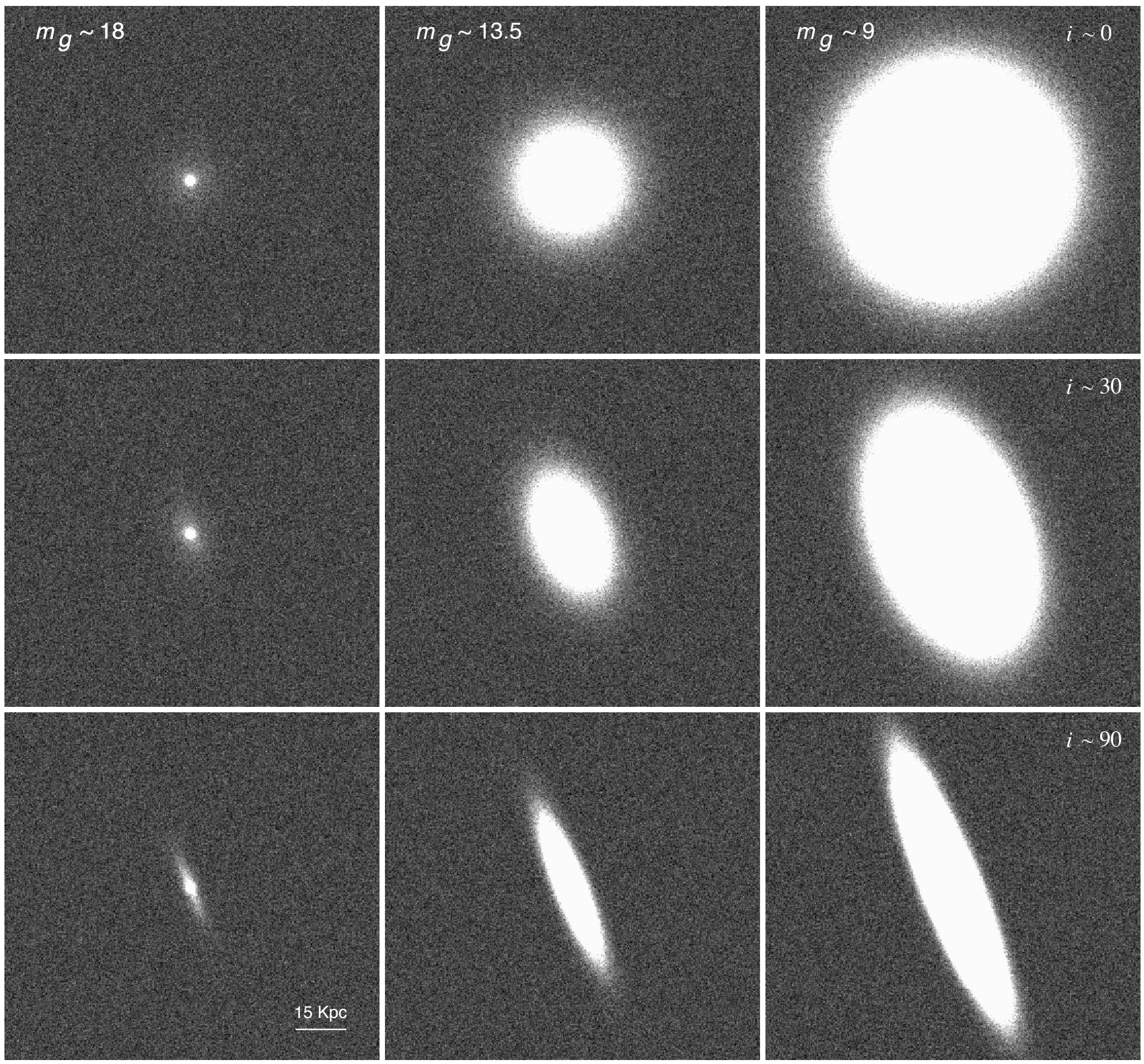

Figure 3.4: Simulated disk galaxies with $B/T \approx 0.3$ at three different values of S/N, which correspond to $m_g \approx 18$, 13.5, and 9 mag, and three inclination angles i. Galaxies with low S/N look compact because the outer part of the disk is undetected. The solid line in the lower left panel shows a scale of 15 Kpc. The simulated images mimic SDSS data.

Once the galaxies are simulated, we fit each of them in two ways: (1) single Sérsic component plus a sky component and (2) a Sérsic component (to represent a bulge), an exponential component (to represent a disk), and a sky component. The sky component is modeled as a plane with a constant slope, to correct for any residual non-flatness, to first order.

3.3 Results

3.3.1 Fitting Disk Galaxies with Single Sérsic Component

In order to quantify the reliability of our model fits, we need to determine the intrinsic size of a simulated galaxy. Davari et al. 2014 (their Fig. 3) show that this can be done robustly by using `IRAF/ellipse` (Jedrzejewski 1987) and constructing the galaxy curve-of-growth.

Local Galaxies

We first discuss the results for single-component fits, the method most widely adopted in the literature to obtain the total luminosity and basic structural parameters of galaxies. Figure 3.5 shows the difference between actual and measured effective radii as a function of S/N, for more than 30,000 model galaxies. The horizontal panels give the result at a given B/T, while the vertical panels give the results for different values of the Sérsic index n.

As shown by Davari et al. (2014), the fits with $n > 6$ are generally unreliable. This comes from the fact that Sérsic profiles with $n > 4$ have a long tail, which can be confused by the background signal and its associated noise. This generally causes overestimation of the total flux and size of a galaxy. We refit these galaxies with $n > 6$ by fixing n to 6, to minimize potential biases caused by these unreliable fits. Comparing dark and light green points in Figure 3.5 demonstrates the significant improvement in the size determination for best-fit models with high Sérsic indices.

The histograms in Figure 3.5 show that the fraction of best-fit models with $2.5 \leq n < 6$ is higher for model galaxies with higher B/T. This is expected, as previous studies have shown that the light distributions of later type galaxies resemble exponential disks ($n = 1$), whereas

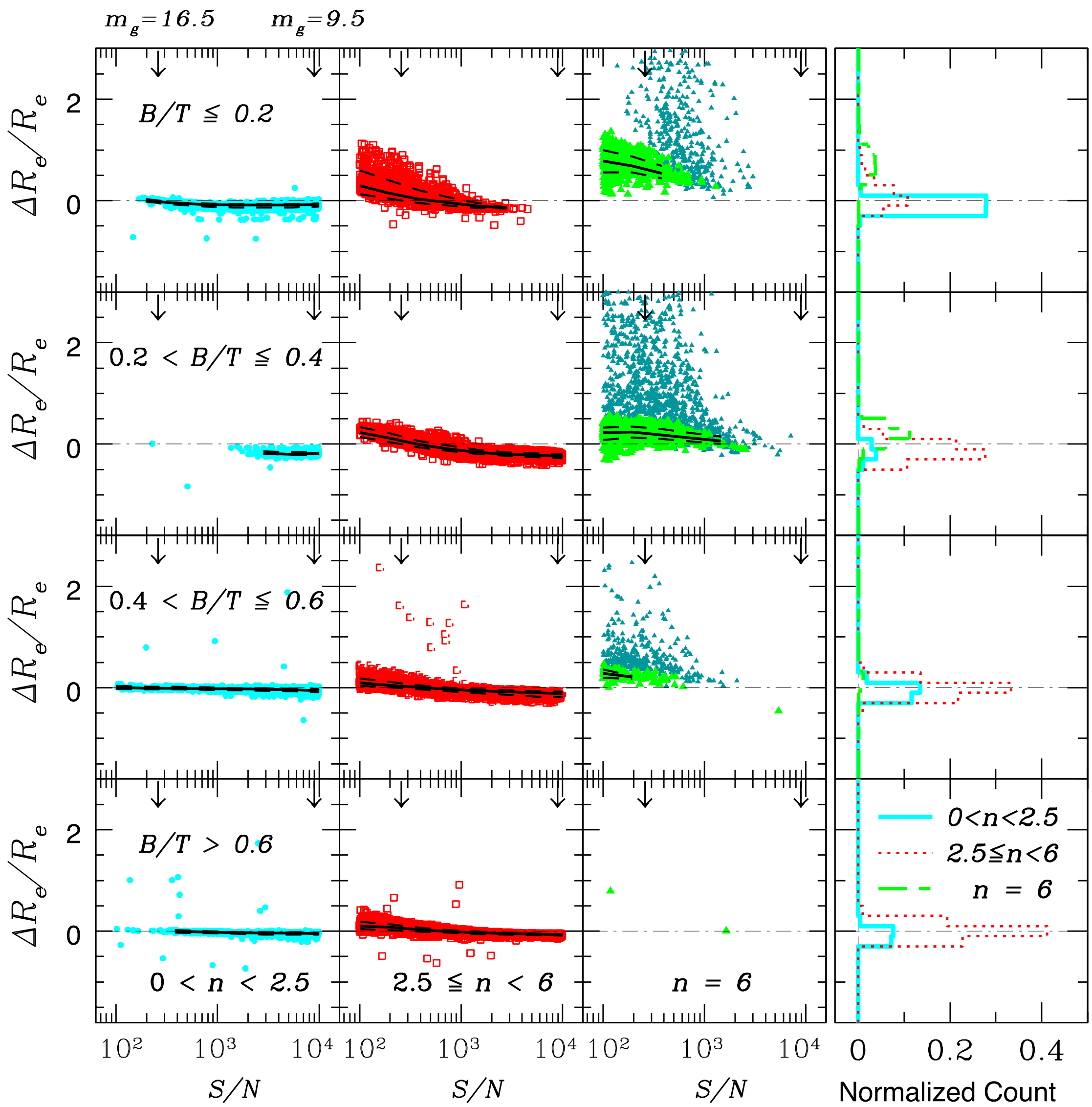

Figure 3.5: Fits of more than 30,000 *local* disk galaxies with a single Sérsic component and a sky component, which is left as a free parameter during the fit. The sky component fits the background with a plane with a constant slope and therefore can correct for any non-flatness to first order. Different rows show the offsets between the measured and the actual effective radius R_e of galaxies with different B/T; the different columns show three intervals in Sérsic index. Cyan solid circles/solid lines, red open squares/dotted lines, and light green solid triangles/dashed lines show the results of best-fit models with $n < 2.5$, $2.5 \leq n < 6$, and $n = 6$, respectively. The dark green points show the models with $n > 6$. The black solid and dashed lines indicate the median and 1σ uncertainties of different measurements. The downward-pointing arrows on the top of each subpanel indicate the S/N of a galaxy with $R_e \approx 15$ pixels, $e = 0$, and $m_g = 9.5$ or 16.5. Comparing dark and light green points shows that refitting single Sérsic fits with $n > 6$ by fixing the Sérsic index to $n = 6$ leads to significant improvement.

bulge-dominated galaxies have light distributions close to $n = 4$. On the other hand, higher background noise level affects the model galaxies with smaller B/T the most. This is evidenced by the fraction of single-component fits that yield high Sérsic indices ($n > 6$). As mentioned above, fits with $n > 6$ are generally unreliable and can lead to significant systematic offsets. This, in part, comes from the fact that Sérsic profiles with large n, which have a steep central part and a long tail at large radii, are very sensitive to changes in the central and outermost parts of the galaxy. The fraction of galaxies with $n \geq 6$ are 15%, 25%, 2%, and <1% for galaxies with $B/T < 0.2$, 0.2–0.4, 0.4–0.6, and > 0.6, respectively.

The higher fraction of unreliable fits at lower S/N for model galaxies with $B/T < 0.4$ is due to their morphological properties. This is demonstrated in Figure 3.6, which illustrates the effects of S/N on the reliability of the fits. Light distributions of model galaxies with $B/T =$ 0.15, 0.30, and 0.45 are shown at three different values of S/N. For model galaxies with B/T < 0.4 a considerable fraction of the flux resides in the disk, which leads to systematic profile deviations in the outskirts. Figure 3.6 shows that this effect is stronger for galaxies with 0.2 $\lesssim B/T \lesssim$ 0.4. Lower S/N leads to a situation where random noise dominates over systematic profile deviations in the outskirts. As the contribution of χ^2 between the outer region and inner is asymmetric, it is generally difficult to know a priori how the Sérsic index would behave when fitting a single-component profile to a multi-component model. Simulations show that the presence of a small bulge (lower B/T) preferentially leads to relatively larger biases in size and luminosity using a single-component fit. Only in the largest B/T and the highest S/N does the fit have a (slightly) opposite effect. In model galaxies with $B/T \geq 0.4$, the prominence of the bulge reduces the contribution of the disk to the overall light distribution. The bottom left panel shows that even at very low S/N `GALFIT` can still reliably measure the size and total luminosity of the model galaxy. This is in agreement with Davari et al. (2014), who find that single-component fits of early-type galaxies can accurately measure their structural properties and total luminosities over a wide range of S/N.

Note that although single-component fits to model galaxies with $0.2 < B/T < 0.4$ have the lowest fraction of best-fit models with $n < 2.5$, at high S/N their fraction is similar to that of

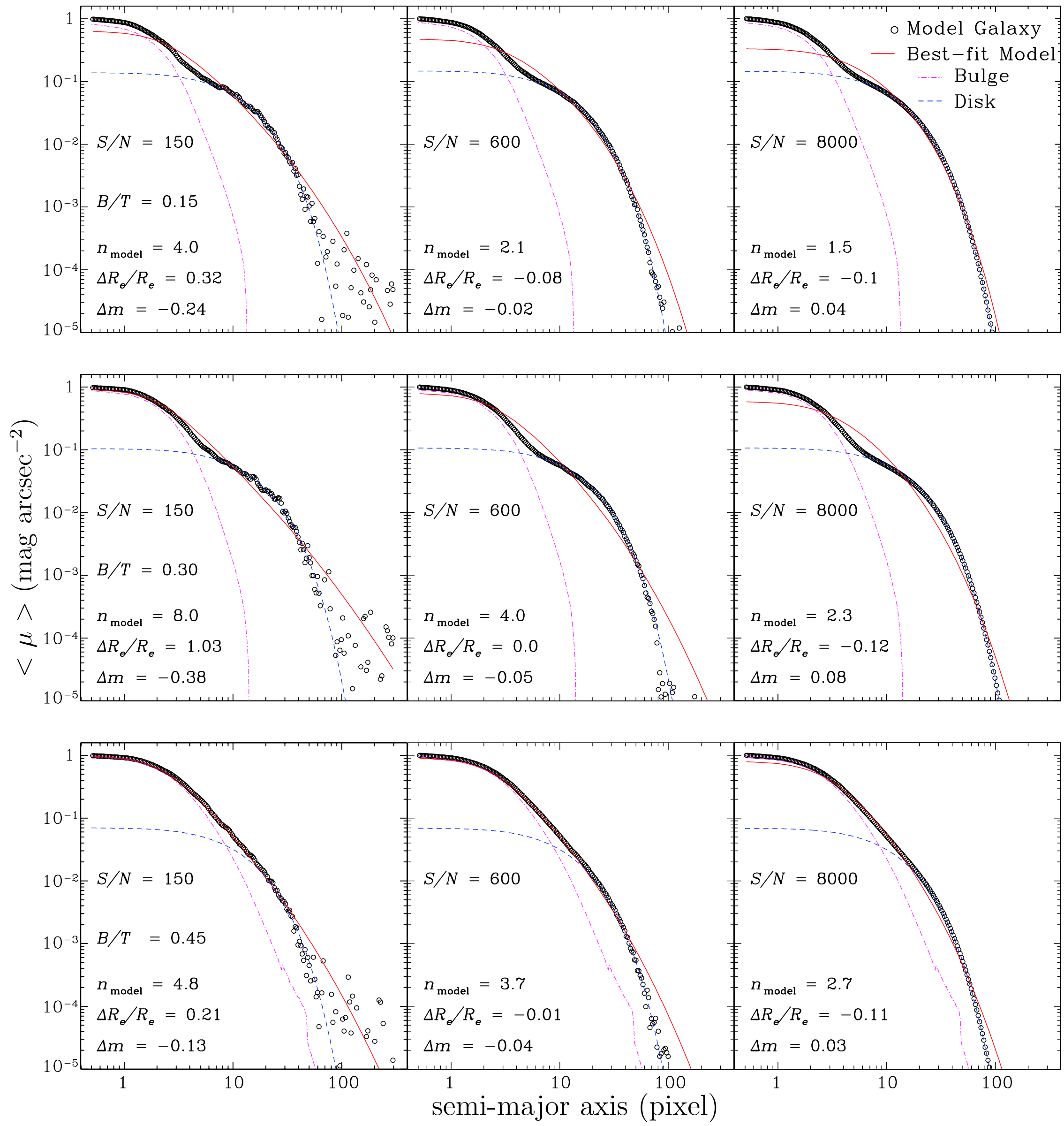

Figure 3.6: The effects of S/N on the reliability of galaxy fitting. The different panels show surface brightness profiles of simulated local galaxies with $B/T = 0.15$, 0.3, and 0.45 at three different values of S/N. Open black and open red points show the light distributions of model galaxy and best-fit model at any given S/N. Magenta dash-dotted and blue dashed lines show the actual bulge and disk light distribution of the model galaxy. For model galaxies with $B/T < 0.4$, the large fraction of disk flux leads to systematic profile deviations in the outskirts; the middle panels show that this effect is stronger for galaxies with $0.2 \lesssim B/T \lesssim 0.4$. Lower S/N leads to a situation where random noise dominates over systematic profile deviations in the outskirts. Our simulations show that the presence of a small bulge (lower B/T) leads to relatively larger biases in size and luminosity using a single-component fit. For model galaxies with $B/T \geq 0.4$, the dominance of the bulge reduces the contribution of the disk to the total light distribution. The bottom left panel shows that even at low S/N, `GALFIT` can measure the size and total luminosity of the model galaxy reliably.

model galaxies with $0.4 < B/T < 0.6$ and higher than that for $B/T > 0.6$. Therefore at higher S/N, as expected, the fraction of best-fit models with $n < 2.5$ is higher for model galaxies with lower B/T.

Tables 1 and 2 summarize the results of the single-component fits. As mentioned before, at low S/N, it is more likely to overestimate the total luminosity and size. On the other hand, at high S/N the non-homology in the light distribution of these two-component galaxies leads to underestimaton of the total luminosity. The offsets are larger for model galaxies with $0.2 < B/T < 0.4$, as these galaxies have the most prominent no-homology in their surface brightness light distribution (Fig. 3.6). And, as expected, the offsets are smaller for bulge-dominated galaxies because of the negligible contribution of the disk component to the overall light profile.

For the range of S/N in which typical local disk galaxies are observed (i.e. a few thousands), systematic offsets are less than 10%–20% for size measurements and $\lesssim$0.1 mag for luminosity measurements. Thus, single-component Sérsic fits using `GALFIT` give reliable sizes and luminosities for typical local disk galaxies.

Estimating the sky value is another key factor in morphological analysis, especially for extended objects like galaxies (e.g., MacArthur et al. 2003; Erwin et al. 2008; Bernardi et al. 2010; Yoon et al. 2011). Davari et al. (2014; their Fig. 9) show the accuracy early-type galaxies: the sky value can be measured with an accuracy better than 0.1%. That finding holds for early-type, including bulge-dominated disk, galaxies, but it may not be the case for more disk-dominated systems. As discussed above, low-S/N, disk-dominated galaxies paradoxically may be better fit by a model with a high Sérsic index, whose extended wings contribute little to χ^2 compared to improvements in the fit toward the center. In order to examine the effect of sky determination, all model galaxies are fit two ways: (1) by letting the sky be a free component in the fit and (2) by fixing the sky value to the actual background value measured independently. We found that at high S/N `GALFIT` can measure the sky value accurately when enough background pixels are available. (Note that the simulated images are at least 15 times larger than the R_e of the model galaxy.) But at low S/N (less than a few hundreds) and for galaxies with low B/T, fixing the sky value decreases the systematic offsets by $\sim 10\%$ for $2.5 \leq n < 6$ and by $\sim 20\%$ for $n \geq 6$.

Table 3.1: Size Offsets for Local Disk Galaxies

B/T (1)	n (2)	S/N 100 – 175 (3)	175 – 315 (4)	315 – 565 (5)	565 – 1000 (6)	1000 – 1750 (7)	1750 – 3150 (8)	3150 – 5650 (9)	5650 – 10000 (10)
	0 – 2.5	...	$0.00^{+0.02}_{-0.03}$	$-0.05^{+0.02}_{-0.03}$	$-0.07^{+0.02}_{-0.04}$	$-0.09^{+0.02}_{-0.04}$	$-0.09^{+0.02}_{-0.05}$	$-0.09^{+0.02}_{-0.05}$	$-0.08^{+0.02}_{-0.04}$
< 0.2	2.5 – 6	$0.29^{+0.30}_{-0.16}$	$0.14^{+0.26}_{-0.10}$	$0.03^{+0.18}_{-0.08}$	$-0.04^{+0.11}_{-0.05}$	$-0.11^{+0.06}_{-0.04}$	$-0.14^{+0.01}_{-0.01}$	...	...
	6	$0.78^{+0.22}_{-0.22}$	$0.69^{+0.18}_{-0.13}$	$0.54^{+0.14}_{-0.1}$	...	...	...	...	...
	0 – 2.5	...	...	...	...	...	$-0.18^{+0.03}_{-0.010}$	$-0.20^{+0.03}_{-0.01}$	$-0.18^{+0.04}_{-0.03}$
0.2 – 0.4	2.5 – 6	$0.23^{+0.10}_{-0.09}$	$0.12^{+0.10}_{-0.08}$	$-0.01^{+0.07}_{-0.06}$	$-0.09^{+0.07}_{-0.04}$	$-0.16^{+0.05}_{-0.03}$	$-0.20^{+0.04}_{-0.03}$	$-0.22^{+0.04}_{-0.04}$	$-0.24^{+0.04}_{-0.05}$
	6	$0.23^{+0.10}_{-0.14}$	$0.24^{+0.11}_{-0.11}$	$0.18^{+0.11}_{-0.08}$	$0.12^{+0.09}_{-0.07}$	$0.07^{+0.08}_{-0.06}$	...	...	...
	0 – 2.5	$0.01^{+0.03}_{-0.03}$	$-0.02^{+0.04}_{-0.01}$	$-0.01^{+0.02}_{-0.03}$	$-0.02^{+0.02}_{-0.03}$	$-0.02^{+0.02}_{-0.02}$	$-0.03^{+0.02}_{-0.02}$	$-0.04^{+0.02}_{-0.03}$	$-0.06^{+0.03}_{-0.04}$
0.4 – 0.6	2.5 – 6	$0.09^{+0.09}_{-0.06}$	$0.05^{+0.07}_{-0.04}$	$0.01^{+0.05}_{-0.04}$	$-0.03^{+0.03}_{-0.04}$	$-0.06^{+0.03}_{-0.04}$	$-0.08^{+0.03}_{-0.06}$	$-0.10^{+0.04}_{-0.07}$	$-0.12^{+0.04}_{-0.07}$
	6	$0.28^{+0.08}_{-0.09}$	$0.22^{+0.02}_{-0.04}$	...	...	...	...	...	...
	0 – 2.5	...	...	$0.00^{+0.02}_{-0.03}$	$-0.01^{+0.01}_{-0.03}$	$-0.03^{+0.01}_{-0.02}$	$-0.04^{+0.02}_{-0.02}$	$-0.04^{+0.02}_{-0.02}$	$-0.05^{+0.02}_{-0.02}$
> 0.6	2.5 – 6	$0.10^{+0.09}_{-0.05}$	$0.07^{+0.06}_{-0.05}$	$0.03^{+0.05}_{-0.03}$	$-0.01^{+0.03}_{-0.02}$	$-0.03^{+0.02}_{-0.02}$	$-0.05^{+0.01}_{-0.02}$	$-0.06^{+0.01}_{-0.02}$	$-0.07^{+0.01}_{-0.02}$
	6	...	...	...	...	...	...	...	...

The difference between the actual and measured effective radius R_e for local model galaxies. Single Sérsic fits with $n > 6$ are refitted by fixing the Sérsic index to $n = 6$.

Col. (1) B/T range.
Col. (2) The subsamples selected based on different ranges of Sérsic index (n).
Col. (3-10) Equally (in logarithmic space) spaced intervals of S/N.

Table 3.2: Magnitude Offsets for Local Disk Galaxies

B/T (1)	n (2)	S/N 100 – 175 (3)	175 – 315 (4)	315 – 565 (5)	565 – 1000 (6)	1000 – 1750 (7)	1750 – 3150 (8)	3150 – 5650 (9)	5650 – 10000 (10)
< 0.2	0 – 2.5	...	$-0.07^{+0.01}_{-0.02}$	$-0.03^{+0.01}_{-0.01}$	$-0.00^{+0.01}_{-0.01}$	$0.02^{+0.02}_{-0.01}$	$0.04^{+0.02}_{-0.02}$	$0.06^{+0.02}_{-0.03}$	$0.06^{+0.03}_{-0.03}$
	2.5 – 6	$-0.23^{+0.07}_{-0.11}$	$-0.16^{+0.06}_{-0.10}$	$-0.10^{+0.04}_{-0.08}$	$-0.04^{+0.03}_{-0.06}$	$0.01^{+0.02}_{-0.02}$	$0.06^{+0.01}_{-0.02}$	...	...
	6	$-0.36^{+0.07}_{-0.07}$	$-0.34^{+0.04}_{-0.05}$	$-0.28^{+0.02}_{-0.04}$	...	...	...	...	...
0.2 – 0.4	0 – 2.5	...	...	...	...	...	$0.03^{+0.01}_{-0.01}$	$0.06^{+0.04}_{-0.02}$	$0.08^{+0.04}_{-0.03}$
	2.5 – 6	$-0.17^{+0.04}_{-0.05}$	$-0.15^{+0.05}_{-0.04}$	$-0.08^{+0.03}_{-0.04}$	$-0.04^{+0.03}_{-0.04}$	$0.00^{+0.02}_{-0.02}$	$0.04^{+0.03}_{-0.02}$	$0.06^{+0.03}_{-0.02}$	$0.08^{+0.03}_{-0.03}$
	6	$-0.18^{+0.06}_{-0.05}$	$-0.19^{+0.05}_{-0.05}$	$-0.18^{+0.05}_{-0.05}$	$-0.16^{+0.03}_{-0.02}$	$-0.12^{+0.02}_{-0.03}$	...	...	...
0.4 – 0.6	0 – 2.5	$-0.02^{+0.01}_{-0.01}$	$-0.01^{+0.01}_{-0.01}$	$-0.01^{+0.01}_{-0.01}$	$-0.01^{+0.01}_{-0.01}$	$-0.00^{+0.01}_{-<0.01}$	$0.00^{+0.01}_{-<0.01}$	$0.01^{+0.02}_{-0.01}$	$0.02^{+0.02}_{-0.01}$
	2.5 – 6	$-0.08^{+0.03}_{-0.04}$	$-0.06^{+0.03}_{-0.04}$	$-0.03^{+0.02}_{-0.03}$	$-0.02^{+0.03}_{-0.02}$	$-0.00^{+0.03}_{-0.01}$	$0.01^{+0.04}_{-0.01}$	$0.03^{+0.06}_{-0.02}$	$0.04^{+0.05}_{-0.02}$
	6	$-0.16^{+0.03}_{-0.03}$	$-0.15^{+0.02}_{-0.02}$	...	...	...	...	...	...
> 0.6	0 – 2.5	...	...	$-0.01^{+0.01}_{-0.01}$	$-0.01^{+0.01}_{-<0.01}$	$-0.01^{+0.01}_{-<0.01}$	$-0.00^{+0.02}_{-<0.01}$	$0.00^{+0.03}_{-<0.01}$	$0.01^{+0.02}_{-<0.01}$
	2.5 – 6	$-0.08^{+0.03}_{-0.04}$	$-0.07^{+0.03}_{-0.03}$	$-0.04^{+0.02}_{-0.03}$	$-0.02^{+0.02}_{-0.02}$	$-0.01^{+0.02}_{-0.01}$	$-0.01^{+0.02}_{-0.01}$	$0.00^{+0.02}_{-0.01}$	$0.00^{+0.01}_{-0.01}$
	6	...	...	...	...	...	...	...	...

The difference between the actual and measured magnitude m for local model galaxies. Single Sérsic fits with $n > 6$ are refitted by fixing the Sérsic index to $n = 6$.

Col. (1) B/T range.
Col. (2) The subsamples selected based on different ranges of Sérsic index (n).
Col. (3-10) Equally (in logarithmic space) spaced intervals of S/N.

Galaxies Rescaled to $z = 2$

Figure 3.7 shows the results of fitting rescaled disk galaxies with a single Sérsic component. The trends are similar to the results for local disk galaxies (Fig. 3.5), but Tables 3 and 4 show that at high S/N the systematic offsets are smaller for rescaled galaxies. As a result of rescaling the size of local galaxies to mimic galaxies at higher redshift, the structural non-homologies are mostly washed out and single-component fits, in fact, return more reliable fits. This can be seen in Figure 3.6 (middle panels) and Figure 3.8 (top panels).

Another noticeable difference between the results of local and rescaled model galaxies is the higher fraction of single-component fits with $n \geq 6$ for more bulge-dominated galaxies. We consider these fits to be unreliable. The fraction of unreliable fits are 8%, 20%, 7%, and <4% for galaxies with $B/T < 0.2$, 0.2–0.4, 0.4–0.6, and >0.6, respectively. Figure 3.8 (botton panels) shows that for rescaled galaxies the S/N can be so low that it even affects the innermost part (i.e., bulge) of the galaxy. Note that, in order to mimic higher redshift observations, the range of S/N is different (lower) for rescaled galaxies. On the other hand, as a result of more homologous light distribution, the fraction of single-component fits with $n > 6$ is lower for rescaled galaxies with $B/T < 0.4$.

3.3.2 Fitting Disk Galaxies with Two Components

Measuring B/T and Total Luminosities

Local Galaxies Figure 3.9 shows the results of measuring the total luminosity of the bulge and disk and B/T for galaxies with three different methods: Sérsic + exponential disk, two Sérsic components, and n=4 + exponential disk. For disk-dominated galaxies (left column), B/T and bulge and disk luminosities can be measured robustly, independent of the method. For galaxies with larger B/T, Figure 3.9 shows that fixing the bulge Sérsic index to incorrect values can lead to considerable biases, especially for galaxies with intermediate B/T $(0.4 < B/T \leq 0.6)$; while the bulge flux contribution is significant, its light distribution does not necessary follow a de Vaucouleurs profile. However, fitting model galaxies with a free Sérsic + exponential disk

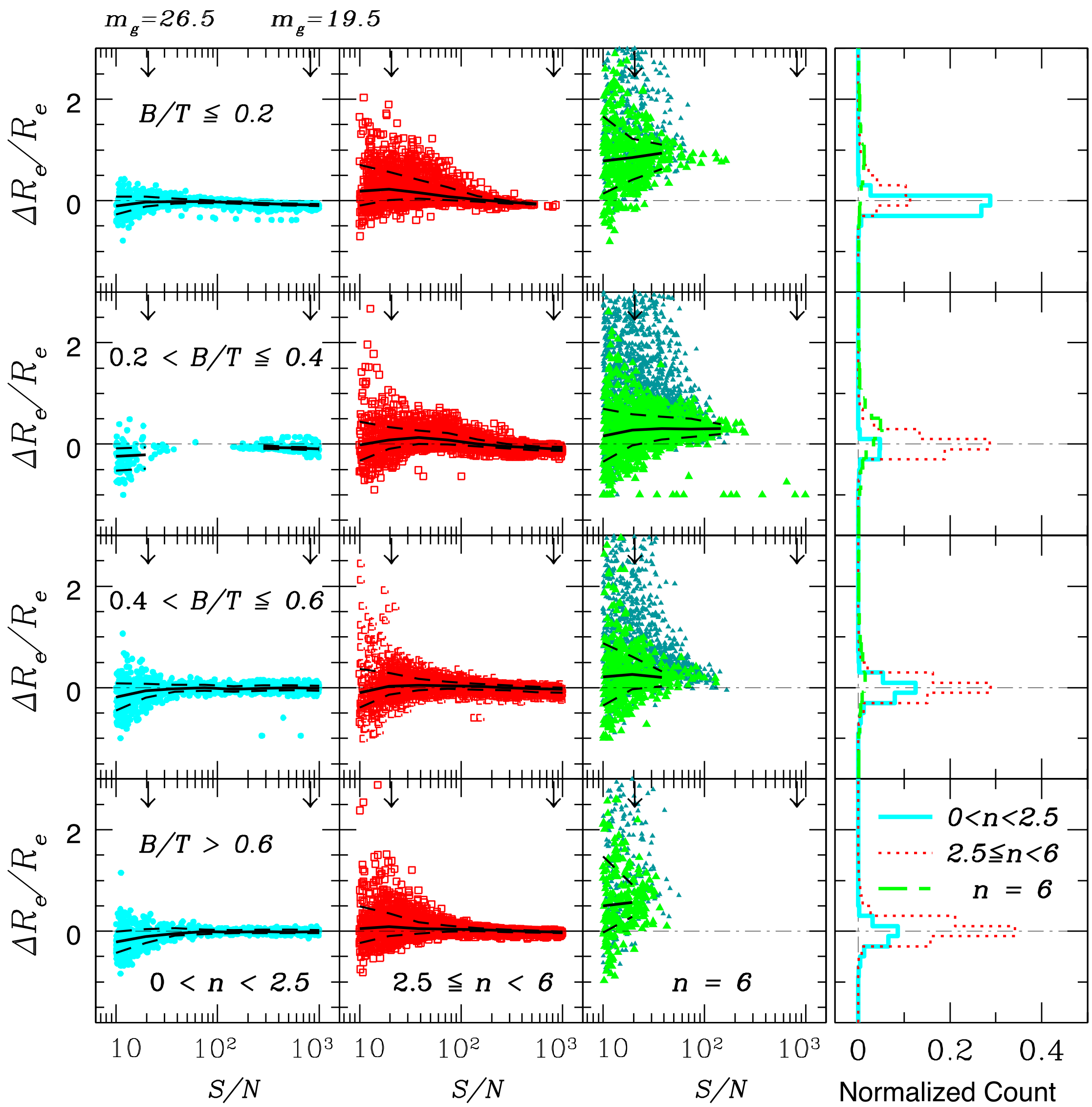

Figure 3.7: Single-component Sérsic fits of more than 30,000 disk galaxies *rescaled* to $z = 2$. The sky component was left as a free parameter. Different rows show the offsets between the measured and the actual effective radius R_e of galaxies with different B/T; the different columns show three intervals in Sérsic index. Cyan solid circles/solid lines, red open squares/dotted lines, and light green solid triangles/dashed lines show the results of best-fit models with $n < 2.5$, $2.5 \leq n < 6$, and $n = 6$, respectively. The dark green points show the models with $n > 6$. The black solid and dashed lines indicate the median and 1σ uncertainties of different measurements. The downward-pointing arrows on the top of each subpanel indicate the S/N of a galaxy with $R_e \approx 5$ pixels, $e = 0$, and $m_g = 19.5$ or 26.5. Comparing dark and light green points shows that refitting single Sérsic fits with $n > 6$ by fixing the Sérsic index to $n = 6$ leads to significant improvement.

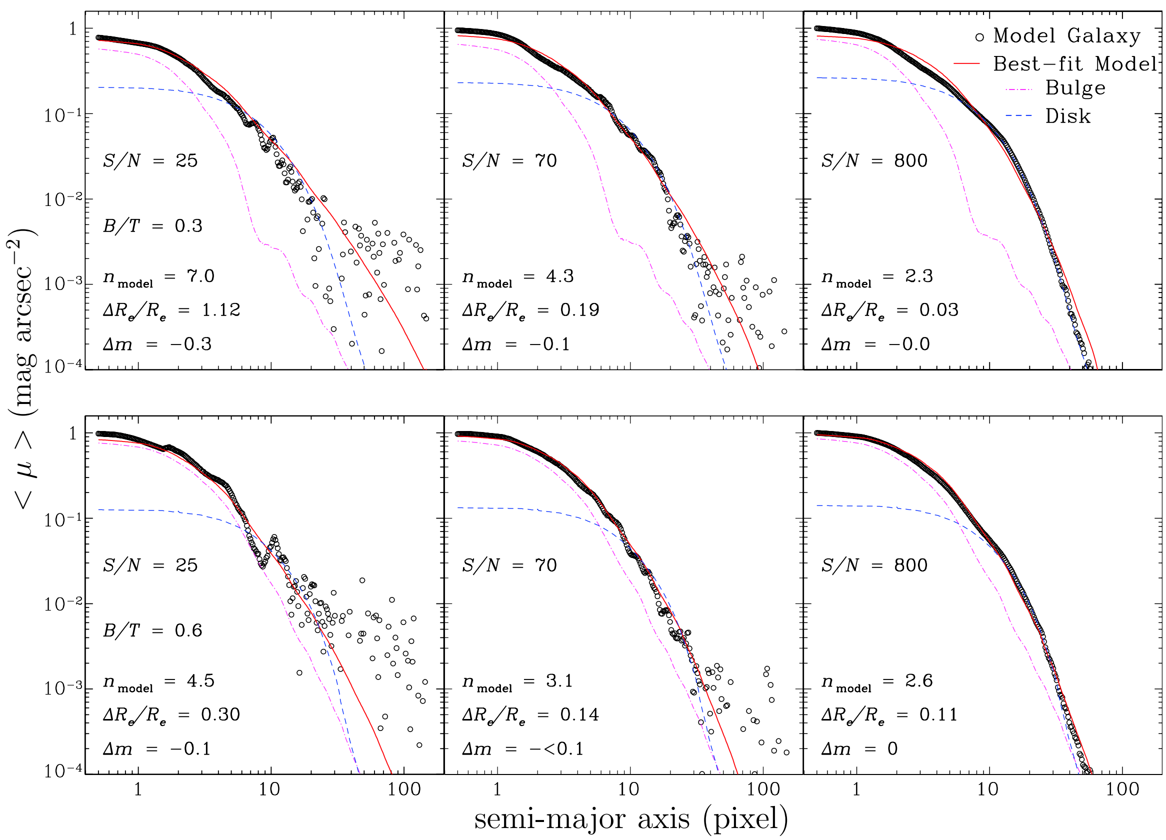

Figure 3.8: The effects of S/N on the reliability of galaxy fitting. The different panels show surface brightness profiles of simulated galaxies rescaled to $z = 2$, with $B/T = 0.30$ and 0.60 at three different values of S/N. Open black and open red points show the light distributions of model galaxy and best-fit model at any given S/N. Magenta dash-dotted and blue dashed lines show the actual bulge and disk light distribution of the model galaxy. Comparing this figure with Figure 3.6 shows that rescaling the local galaxies to higher redshift weakens the structural non-homologies, and single-component models return more reliable fits (top panels). Furthermore, for rescaled galaxies the S/N can be so low that it even affects the innermost part (i.e. bulge) of the galaxy and therefore leads to unreliable single-component fits (lower panels).

Table 3.3: Size Offsets for Disk Galaxies Rescaled to $z = 2$

		S/N							
B/T (1)	n (2)	100 – 175 (3)	175 – 315 (4)	315 – 565 (5)	565 – 1000 (6)	1000 – 1750 (7)	1750 – 3150 (8)	3150 – 5650 (9)	5650 – 10000 (10)
< 0.2	0 – 2.5	$-0.01^{+0.17}_{-0.16}$	$-0.04^{+0.07}_{-0.08}$	$-0.06^{+0.03}_{-0.04}$	$-0.05^{+0.02}_{-0.02}$	$-0.04^{+0.02}_{-0.02}$	$-0.02^{+0.01}_{-0.01}$	$-0.01^{+0.01}_{-0.01}$	$-0.00^{+<0.00}_{-<0.00}$
	2.5 – 6	$-0.20^{+0.16}_{-0.21}$	$-0.20^{+0.11}_{-0.13}$	$-0.17^{+0.06}_{-0.11}$	$-0.14^{+0.04}_{-0.08}$	$-0.10^{+0.03}_{-0.04}$	$-0.07^{+0.01}_{-0.03}$	$-0.05^{+0.01}_{-0.01}$	...
	6	$-0.41^{+0.25}_{-0.26}$	$-0.40^{+0.15}_{-0.10}$	$-0.41^{+0.09}_{-0.06}$	...	...	...	...	...
0.2 – 0.4	0 – 2.5	$0.14^{+0.19}_{-0.17}$	...	...	...	...	$-0.02^{+0.01}_{-0.01}$	$-0.01^{+0.01}_{-0.01}$	$-0.01^{+<0.00}_{-<0.00}$
	2.5 – 6	$-0.11^{+0.22}_{-0.22}$	$-0.13^{+0.12}_{-0.11}$	$-0.14^{+0.07}_{-0.07}$	$-0.12^{+0.05}_{-0.08}$	$-0.08^{+0.03}_{-0.06}$	$-0.05^{+0.02}_{-0.03}$	$-0.03^{+0.01}_{-0.02}$	$-0.01^{+0.01}_{-0.01}$
	6	$-0.18^{+0.25}_{-0.22}$	$-0.21^{+0.12}_{-0.13}$	$-0.22^{+0.07}_{-0.08}$	$-0.22^{+0.06}_{-0.08}$	$-0.23^{+0.04}_{-0.04}$	...	...	...
0.4 – 0.6	0 – 2.5	$0.10^{+0.19}_{-0.18}$	$0.04^{+0.07}_{-0.08}$	$0.00^{+0.04}_{-0.03}$	$-0.01^{+0.01}_{-0.01}$	$-0.01^{+0.01}_{-0.01}$	$-0.01^{+<0.00}_{-<0.00}$	$-0.00^{+<0.00}_{-<0.00}$	$-0.00^{+<0.00}_{-<0.00}$
	2.5 – 6	$-0.03^{+0.15}_{-0.21}$	$-0.07^{+0.09}_{-0.11}$	$-0.06^{+0.05}_{-0.06}$	$-0.05^{+0.03}_{-0.04}$	$-0.04^{+0.02}_{-0.03}$	$-0.02^{+0.01}_{-0.02}$	$-0.01^{+0.01}_{-0.01}$	$-0.01^{+0.01}_{-0.01}$
	6	$-0.18^{+0.22}_{-0.26}$	$-0.19^{+0.11}_{-0.11}$	$-0.15^{+0.06}_{-0.05}$	...	...	...	...	...
> 0.6	0 – 2.5	$0.13^{+0.22}_{-0.17}$	$0.07^{+0.08}_{-0.09}$	$0.01^{+0.05}_{-0.04}$	$-0.01^{+0.02}_{-0.01}$	$-0.01^{+0.01}_{-0.01}$	$-0.01^{+<0.00}_{-<0.00}$	$-0.01^{+<0.00}_{-<0.00}$	$-0.00^{+<0.00}_{-<0.00}$
	2.5 – 6	$-0.09^{+0.18}_{-0.23}$	$-0.08^{+0.11}_{-0.13}$	$-0.05^{+0.05}_{-0.07}$	$-0.05^{+0.02}_{-0.04}$	$-0.04^{+0.02}_{-0.02}$	$-0.03^{+0.01}_{-0.01}$	$-0.02^{+0.01}_{-0.01}$	$-0.01^{+0.01}_{-0.01}$
	6	...	...	...	...	...	...	...	...

The difference between the actual and measured magnitude m for model galaxies rescaled to $z = 2$. Single Sérsic fits with $n > 6$ are refitted by fixing the Sérsic index to $n = 6$.

Col. (1) B/T range.
Col. (2) The subsamples selected based on different ranges of Sérsic index (n).
Col. (3-10) Equally (in logarithmic space) spaced intervals of S/N.

Table 3.4: Magnitude Offsets for Disk Galaxies Rescaled to $z = 2$

		S/N							
B/T (1)	n (2)	100 – 175 (3)	175 – 315 (4)	315 – 565 (5)	565 – 1000 (6)	1000 – 1750 (7)	1750 – 3150 (8)	3150 – 5650 (9)	5650 – 10000 (10)
< 0.2	0 – 2.5	...	$-0.07^{+0.01}_{-0.02}$	$-0.03^{+0.01}_{-0.01}$	$-0.00^{+0.01}_{-0.01}$	$0.02^{+0.02}_{-0.01}$	$0.04^{+0.02}_{-0.02}$	$0.06^{+0.02}_{-0.03}$	$0.06^{+0.03}_{-0.03}$
	2.5 – 6	$-0.23^{+0.07}_{-0.11}$	$-0.16^{+0.06}_{-0.10}$	$-0.10^{+0.04}_{-0.08}$	$-0.04^{+0.03}_{-0.06}$	$0.01^{+0.02}_{-0.02}$	$0.06^{+0.01}_{-0.02}$	...	...
	6	$-0.36^{+0.07}_{-0.07}$	$-0.34^{+0.04}_{-0.05}$	$-0.28^{+0.02}_{-0.04}$	...	...	...	...	...
0.2 – 0.4	0 – 2.5	...	...	...	...	...	$0.03^{+0.01}_{-0.01}$	$0.06^{+0.04}_{-0.02}$	$0.08^{+0.04}_{-0.03}$
	2.5 – 6	$-0.17^{+0.04}_{-0.05}$	$-0.15^{+0.05}_{-0.04}$	$-0.08^{+0.03}_{-0.04}$	$-0.04^{+0.03}_{-0.04}$	$0.00^{+0.02}_{-0.02}$	$0.04^{+0.03}_{-0.02}$	$0.06^{+0.03}_{-0.02}$	$0.08^{+0.03}_{-0.03}$
	6	$-0.18^{+0.06}_{-0.05}$	$-0.19^{+0.05}_{-0.05}$	$-0.18^{+0.05}_{-0.05}$	$-0.16^{+0.03}_{-0.02}$	$-0.12^{+0.02}_{-0.03}$	...	...	...
0.4 – 0.6	0 – 2.5	$-0.02^{+0.01}_{-0.01}$	$-0.01^{+0.01}_{-0.01}$	$-0.01^{+0.01}_{-0.01}$	$-0.01^{+0.01}_{-0.01}$	$-0.00^{+0.01}_{-<0.01}$	$0.00^{+0.01}_{-<0.01}$	$0.01^{+0.02}_{-0.01}$	$0.02^{+0.02}_{-0.01}$
	2.5 – 6	$-0.08^{+0.03}_{-0.04}$	$-0.06^{+0.03}_{-0.04}$	$-0.03^{+0.02}_{-0.03}$	$-0.02^{+0.03}_{-0.02}$	$-0.00^{+0.03}_{-0.01}$	$0.01^{+0.04}_{-0.01}$	$0.03^{+0.06}_{-0.02}$	$0.04^{+0.05}_{-0.02}$
	6	$-0.16^{+0.03}_{-0.03}$	$-0.15^{+0.02}_{-0.02}$	...	...	...	...	...	...
> 0.6	0 – 2.5	...	...	$-0.01^{+0.01}_{-0.01}$	$-0.01^{+0.01}_{-<0.01}$	$-0.01^{+0.01}_{-<0.01}$	$-0.00^{+0.02}_{-<0.01}$	$0.00^{+0.03}_{-<0.01}$	$0.01^{+0.02}_{-<0.01}$
	2.5 – 6	$-0.08^{+0.03}_{-0.04}$	$-0.07^{+0.03}_{-0.03}$	$-0.04^{+0.02}_{-0.03}$	$-0.02^{+0.02}_{-0.02}$	$-0.01^{+0.02}_{-0.01}$	$-0.01^{+0.02}_{-0.01}$	$0.00^{+0.02}_{-0.01}$	$0.00^{+0.01}_{-0.01}$
	6	...	...	...	...	...	...	...	...

The difference between the actual and measured magnitude m for model galaxies rescaled to $z = 2$. Single Sérsic fits with $n > 6$ are refitted by fixing the Sérsic index to $n = 6$.

Col. (1) B/T range.
Col. (2) The subsamples selected based on different ranges of Sérsic index (n).
Col. (3-10) Equally (in logarithmic space) spaced intervals of S/N.

(cyan points) and even two Sérsic components (green points) results in robust luminosity and B/T determinations.

Previous studies have shown that not all disks follow an exponential light distribution (e.g., Boroson 1981), and therefore it is useful to know how well one can measure the Sérsic index and subsequent properties of the disk component, in case the disk has n different from 1. Comparing the cases where the disk is set to $n = 1$ versus $n =$ free in Figure 3.9, we find that although in general the uncertainties are lower for $n = 1$, at higher S/N the results of $n = 1$ and $n =$ free are comparable. This implies that, as known, the disk component need not follow a pure exponential function, in oder to find a reliable bulge+disk model fit.

Rescaled Galaxies to $z = 2$ As expected, the measurements are more uncertain for high-z galaxies (Fig. 3.10), as their bulges typically have R_e smaller than one pixel, and, besides, structural non-homologies are mostly washed out (Fig. 3.8). However, by employing different fitting methods, B/T can be measured with no significant bias for S/N of a few 100, values typical of actual *HST* observations of compact massive galaxies (e.g., Szomoru et al. 2012). Similar to the result for local galaxies, for galaxies with very small B/T, any of the methods yields reliable results; however, for galaxies with higher B/T, it is best to fit the bulge component with a free n to mitigate systematic biases, even if the biases are smaller compared to local galaxies.

Measuring Bulge Properties

Local Galaxies Figure 3.11 reinforces the conclusions drawn from Figure 3.9. Sérsic + exponential and Sérsic + Sérsic models can measure bulge properties with high accuracy. Figure 3.11 shows that $n = 4$ + exponential is not a reliable model as it leads to biases in bulge size measurements. Furthermore, any information on bulge n is lost.

Galaxies Rescaled to $z = 2$ Figure 3.12 shows that for high-z galaxies with $B/T \leq 0.4$, measuring the bulge properties is vulnerable to large uncertainties and systematic offsets independent of the fitting method. Note that the bulge effective radius of these galaxies are all less

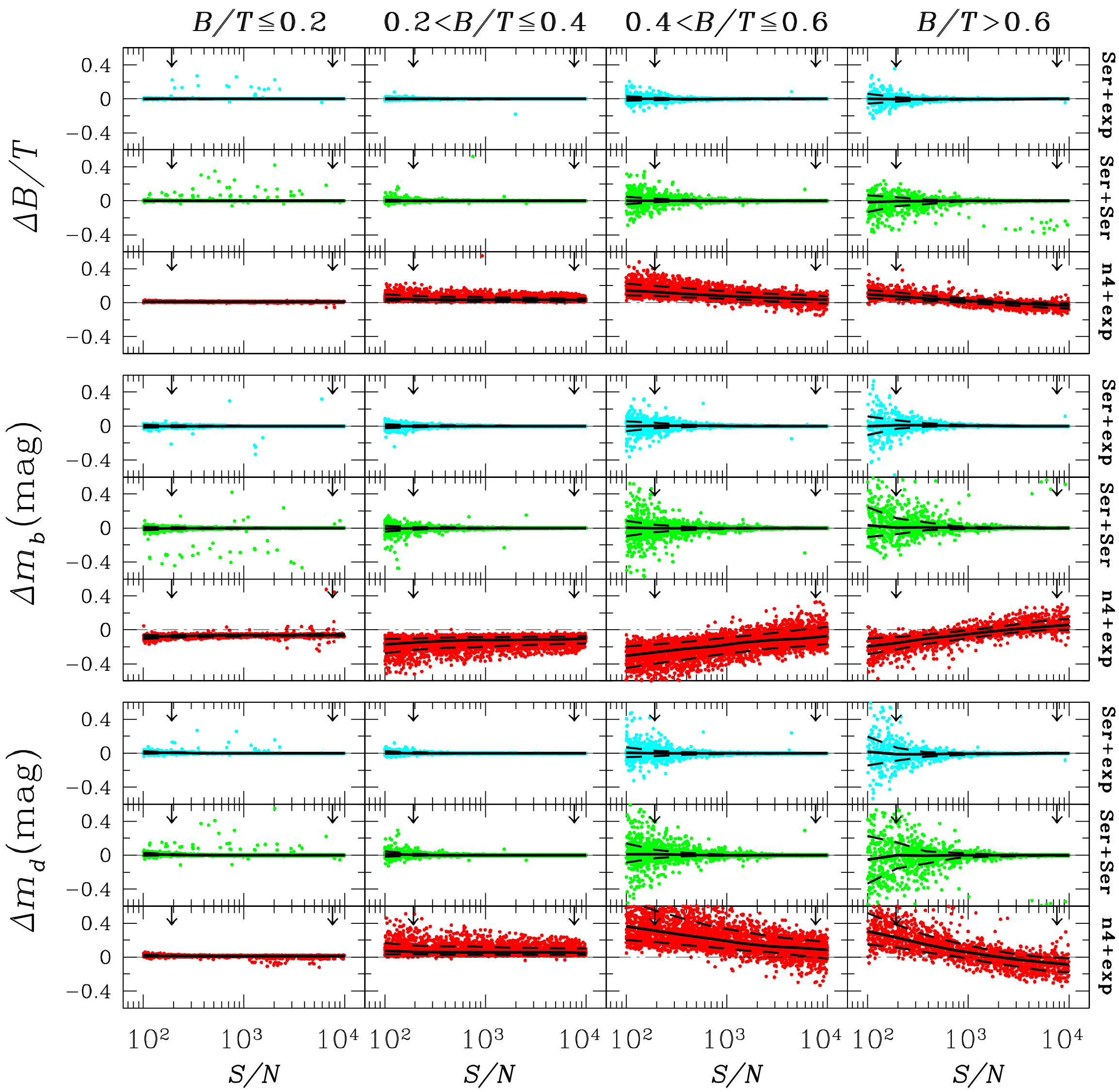

Figure 3.9: Measuring total luminosity of the bulge and disk and B/T of about 30,000 *local* disk galaxies with three different models: Sérsic + exponential disk (Ser+exp; cyan points), two Sérsic components (Ser+Ser; green points), and $n4$ + exponential disk ($n4$+exp; red points). Vertical panels show the results for different ranges of B/T, increasing from from left to right. Horizontal panels, from top to bottom, show the measurement offsets for B/T, bulge magnitude m_b, and disk magnitude m_d, respectively. The black solid and dashed lines indicate the median and 1σ uncertainties of different measurements. The downward-pointing arrows on the top of each subpanel indicate the S/N of a galaxy with $R_e \approx 15$ pixels, $e = 0$, and $m_g = 9.5$ or 16.5.

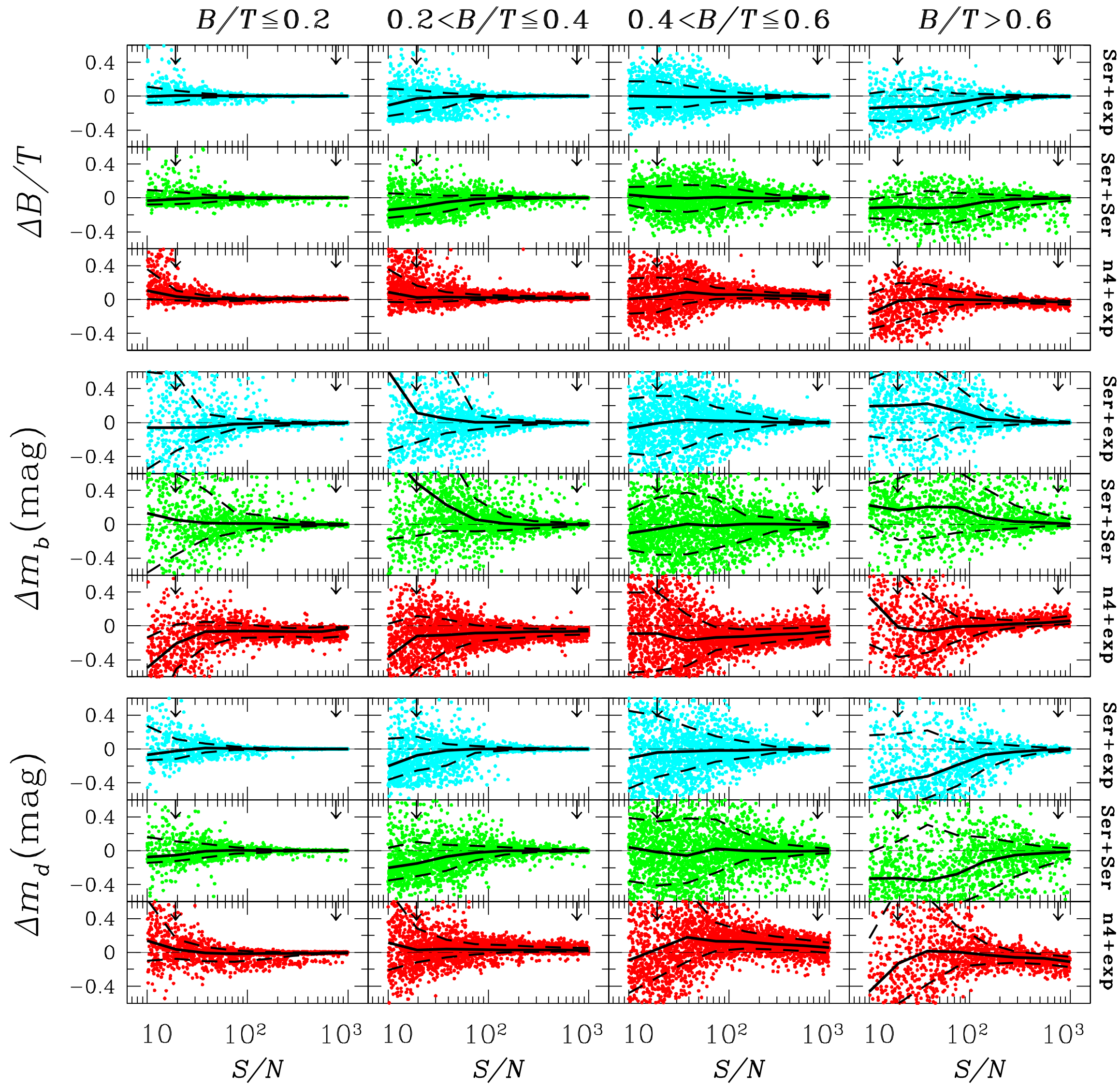

Figure 3.10: Measuring total luminosity of the bulge and disk and B/T of about 30,000 disk galaxies *rescaled* to $z = 2$ with three different models: Sérsic + exponential disk (Ser+exp; cyan points), two Sérsic components (Ser+Ser; green points), and $n4$ + exponential disk ($n4$+exp; red points). Vertical panels show the results for different ranges of B/T, increasing from from left to right. Horizontal panels, from top to bottom, show the measurement offsets for B/T, bulge magnitude m_b, and disk magnitude m_d, respectively. The black solid and dashed lines indicate the median and 1σ uncertainties of different measurements. The downward-pointing arrows on the top of each subpanel indicate the S/N of a galaxy with $R_e \approx 5$ pixels, $e = 0$, and $m_H = 19.5$ or 26.5.

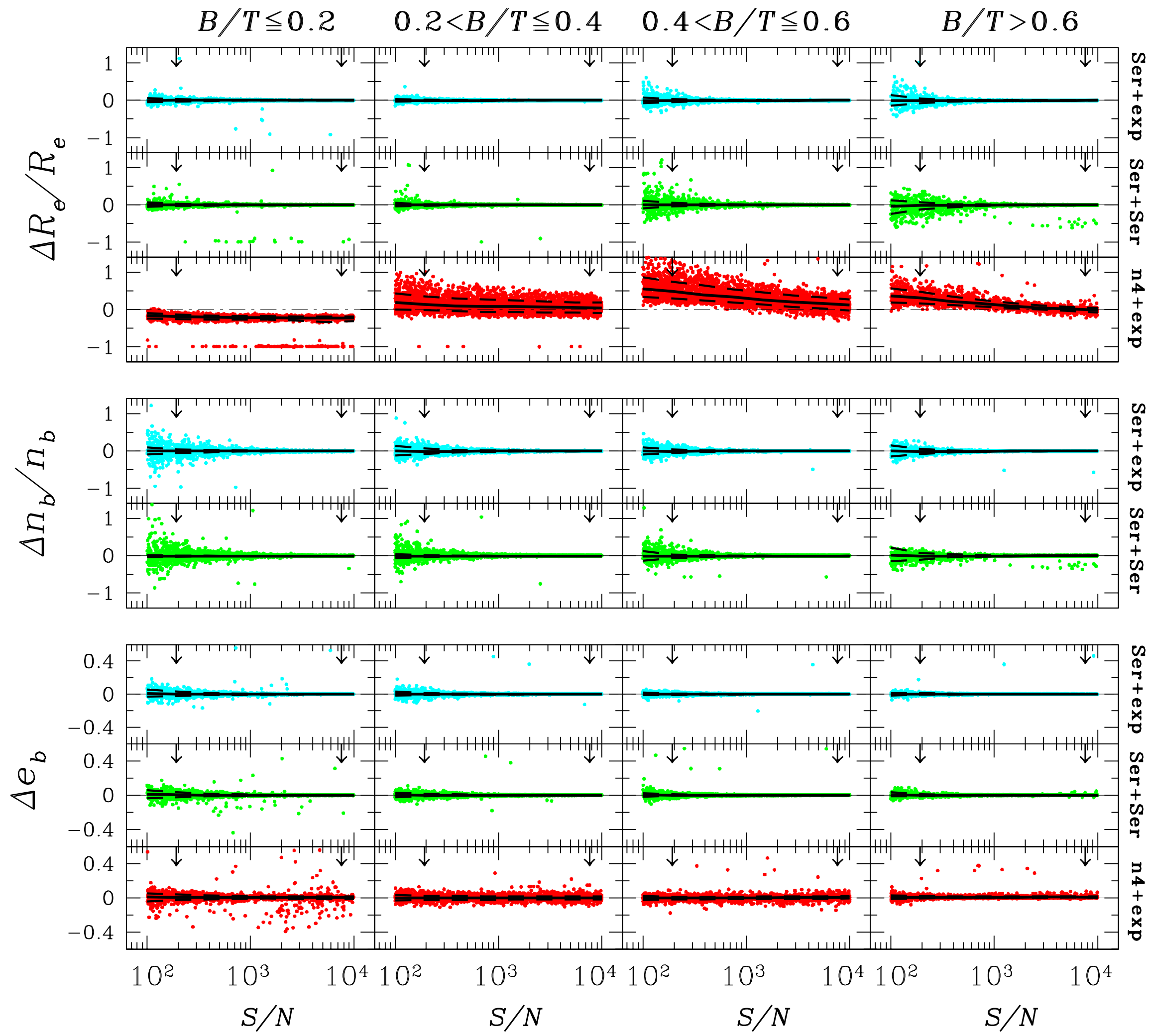

Figure 3.11: Measuring bulge properties of about 30,000 *local* disk galaxies with three different models: Sérsic + exponential disk (Ser+exp; cyan points), two Sérsic components (Ser+Ser; green points), and $n4$ + exponential disk ($n4$+exp; red points). Vertical panels show the results for different ranges of B/T, increasing from from left to right. Horizontal panels, from top to bottom, show the measurement offsets for bulge effective radius R_e, Sérsic index n_b, and ellipticity e_b. The black solid and dashed lines indicate the median and 1σ uncertainties of different measurements. The downward-pointing arrows on the top of each subpanel indicate the S/N of a galaxy with $R_e \approx 15$ pixels, $e = 0$, and $m_g = 9.5$ or 16.5.

than 0.5 pixel and thus unresolved. However, for model galaxies with $B/T \geq 0.4$ and at S/N of compact massive galaxies observed at high z, the bulge properties can be measured reliably. As expected, the Sérsic index is most vulnerable to large uncertainties.

Measuring Disk Properties

The number of pixels that each component occupies affects the robustness of the fit. The disk component, being intrinsically larger than the bulge, is therefore easier to measure than the bulge. Figure 3.13 demonstrates this fact. All methods can measure the disk properties of local galaxies with no systematic offsets over a wide range of S/N. The only exception is when the n=4+exponential model is used for galaxies with higher B/T; this method causes ∼10% systematic offsets. The middle panel of the figure shows that the Sérsic+Sérsic model can measure the disk Sérsic index robustly.

Figure 3.14 shows that even for galaxies rescaled to $z = 2$, disk properties can be measured with little to no systematic offsets and with low uncertainties at the S/N pertinent to massive compact high-z galaxies.

3.4 Comparison to Other Studies

Our results generally agree well with those of other similar recent studies. Using a spectroscopically selected sample of galaxies selected from SDSS, Meert et al. (2013) show that single-component Sérsic fits of two-component (bulge + disk) simulated galaxies can lead to systematic biases in size measurements (their Fig. 8b), but the offsets are small, generally $\lesssim$10% over a wide range of galaxy sizes. This is consistent with our simulations of local galaxies: Tables 1 and 2 show that for our disk-dominated and bulge-dominated model galaxies the systematic offsets are less than 10%, and for model galaxies with more prominent non-homology the offsets can be as large as 20%. However, for very low S/N (i.e., a few hundred) the systematic offsets can be even larger.

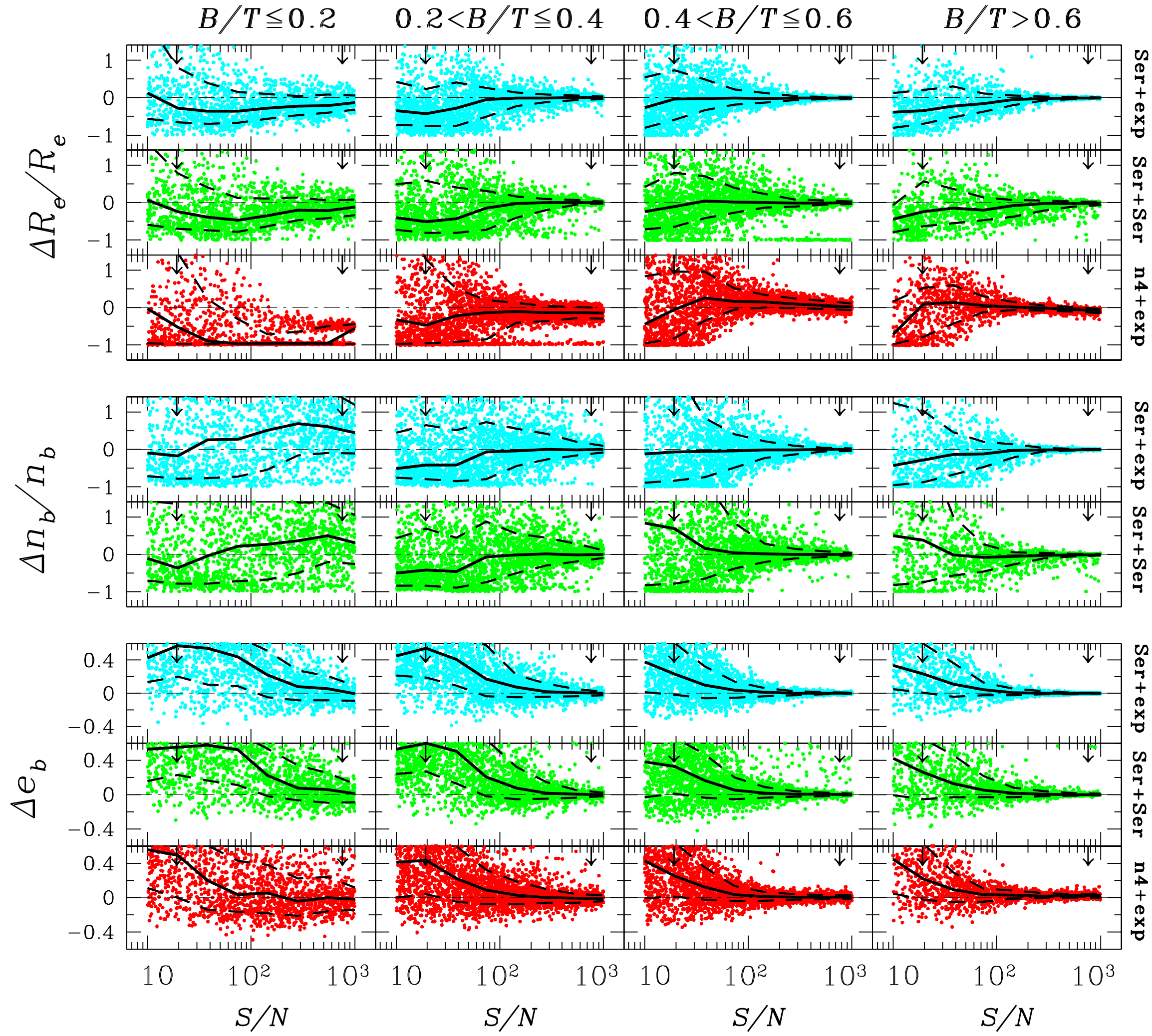

Figure 3.12: Measuring bulge properties of about 30,000 disk galaxies *rescaled* to $z = 2$ with three different models: Sérsic + exponential disk (Ser+exp; cyan points), two Sérsic components (Ser+Ser; green points), and $n4$ + exponential disk ($n4$+exp; red points). Vertical panels show the results for different ranges of B/T, increasing from from left to right. Horizontal panels, from top to bottom, show the measurement offsets for bulge effective radius R_e, Sérsic index n_b, and ellipticity e_b. The black solid and dashed lines indicate the median and 1σ uncertainties of different measurements. The downward-pointing arrows on the top of each subpanel indicate the S/N of a galaxy with $R_e \approx 5$ pixels, $e = 0$, and $m_H = 19.5$ or 26.5.

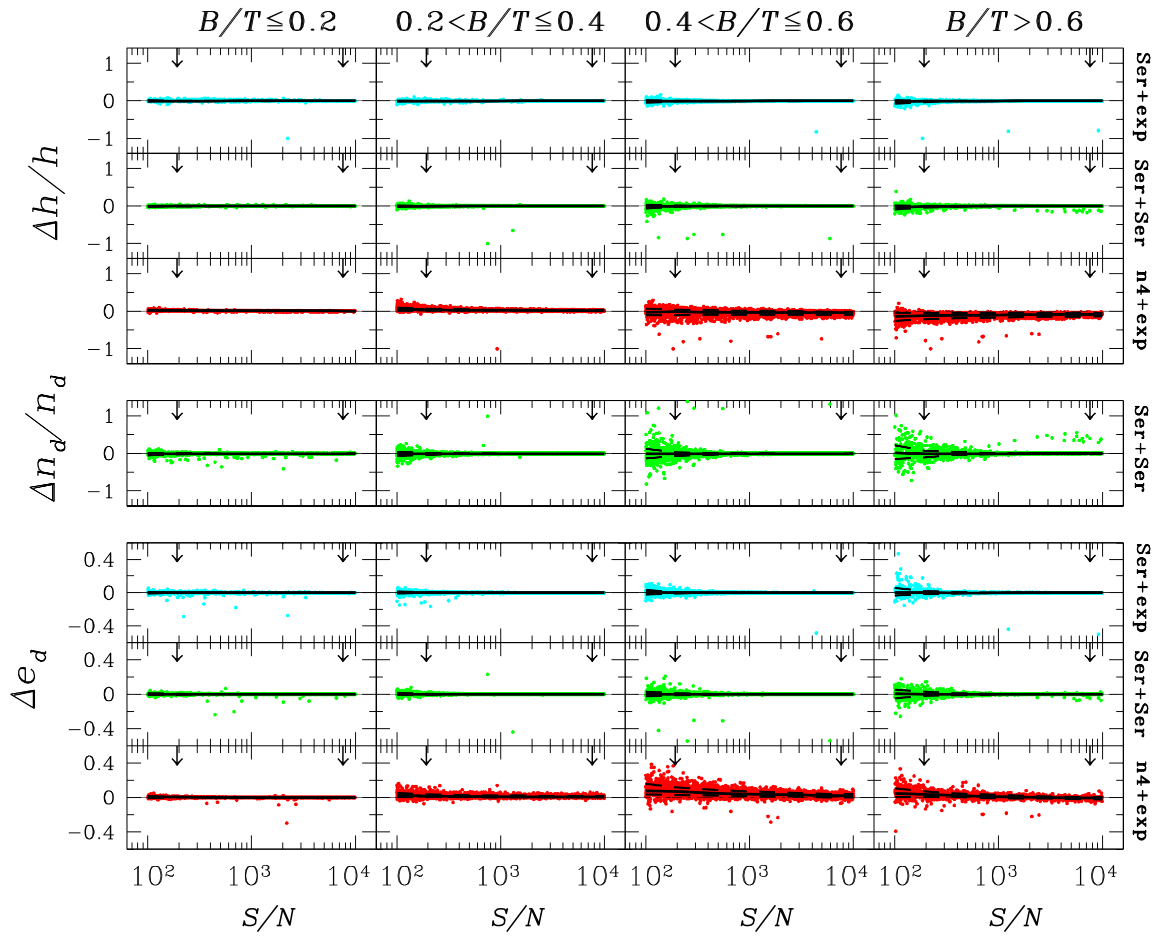

Figure 3.13: Measuring disk properties of about 30,000 *local* disk galaxies with three different models: Sérsic + exponential disk (Ser+exp; cyan points), two Sérsic components (Ser+Ser; green points), and $n4$ + exponential disk ($n4$+exp; red points). Vertical panels show the results for different ranges of B/T, increasing from from left to right. Horizontal panels, from top to bottom, show the measurement offsets for disk scale length h, Sérsic index n_d, and ellipticity e_d. The black solid and dashed lines indicate the median and 1σ uncertainties of different measurements. The downward-pointing arrows on the top of each subpanel indicate the S/N of a galaxy with $R_e \approx 15$ pixels, $e = 0$, and $m_g = 9.5$ or 16.5.

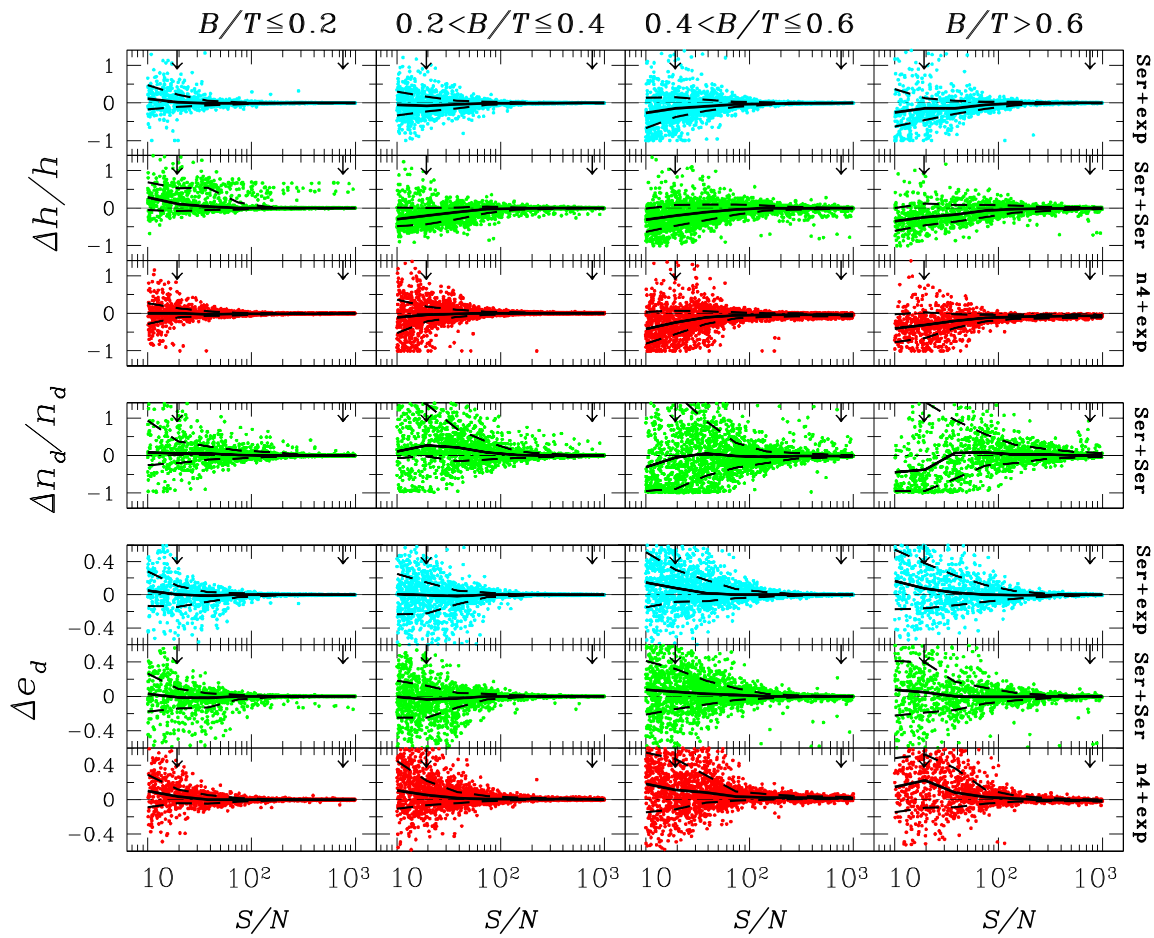

Figure 3.14: Measuring disk properties of about 30,000 disk galaxies *rescaled* to $z = 2$ with three different models: Sérsic + exponential disk (Ser+exp; cyan points), two Sérsic components (Ser+Ser; green points), and $n4$ + exponential disk ($n4$+exp; red points). Vertical panels show the results for different ranges of B/T, increasing from from left to right. Horizontal panels, from top to bottom, show the measurement offsets for disk scale length h, Sérsic index n_d, and ellipticity e_d. The black solid and dashed lines indicate the median and 1σ uncertainties of different measurements. The downward-pointing arrows on the top of each subpanel indicate the S/N of a galaxy with $R_e \approx 5$ pixels, $e = 0$, and $m_H = 19.5$ or 26.5.

Meert et al. (2013), again in agreement with our findings, show that fitting local bulge+disk model galaxies with two components result in more reliable fits and measured structural parameters (their Figs. 9 and 10), as the systematic offsets are close to zero over a wide range of apparent magnitude (i.e., S/N). They also find that disk parameters can be measured more accurately compare to those for the bulge (Fig. 3.13). The parameter most vulnerable to large uncertainties is n_b, confirming our findings (Fig. 3.11).

Meert et al. (2013) further examined the effects of image size on the accuracy of `GALFIT` sky determination. They find (their Figs. 12, 14, and 15), as we do, that `GALFIT` can measure the sky value with an accuracy of 0.1%. Our simulations indicate that when the images are large enough (i.e., 10–15 times larger than effective radius of the galaxy), the sky component can be set as a free parameter for `GALFIT` modeling.

The simulations of Mosleh et al. (2013) show that size measurements done by two-component Sérsic fits are more reliable than single Sérsic fits. They found that for local massive, red, early-type galaxies (their Fig. 3), single-component fits overestimate the size. This bias goes away for their redshifted galaxies, consistent with our findings. Rescaling galaxies to higher redshifts washes out the structural non-homology and therefore single Sérsic fits can model the galaxy light profile better.

In general, our results confirm the findings of Meert et al. (2013) and Mosleh et al. (2013). Furthermore, our simulations, for the first time, provide a detailed study of `GALFIT` modeling of galaxies with a wide range of B/T and S/N. For instance, our results show that for different methods (i.e. Sérsic+exponential, n=4+exponential), the reliability of the fits varies for different values of B/T. Knowing the optimum method for a specific value of S/N and B/T offers a roadmap for a variety of structural analysis.

3.5 Implications for Red Nuggets

Our simulations provide a metric for quantifying the uncertainties in measuring the properties of the red, massive galaxies at $z = 2$. These peculiar objects are found to be generally compact

($R_e \leq 2.0$ kpc). They mainly have $H_{160} < 23$, with a small fraction having $H_{160} \approx 23-24$ (Szomoru et al. 2012). This translates to high S/N (≥ 100) for typical single-orbit *HST* exposures.

Several previous studies have shown that if the light distributions of red nuggets follow a single Sérsic profile, at the S/N that these galaxies are observed, the structural parameters and the total luminosity can be measured accurately (e.g., Häussler et al. 2007; Trujillo et al. 2007; Cimatti et al. 2008; Szomoru et al. 2010; van Dokkum & Brammer 2010; Williams et al. 2010; Papovich et al. 2012; van der Wel et al. 2012; Meert et al. 2013; Mosleh et al. 2013; Davari et al. 2014).

On the other hand, the structural non-homologies can lead to biases in size measurements using single-component fitting (a popular method). Davari et al. (2014) found that if the red nuggets have structures similar to those of local massive elliptical galaxies, single Sérsic fits return reliable size (with about 10% systematic offsets) and total luminosity measurements. In this paper, we further extend previous work by examining the potential biases of single-component size measurements of red nuggets, *assuming* that their light distributions resemble that of late-type, disk galaxies. Our work is motivated by the possibility that red nuggets contain a significant disk component. We are interested in knowing whether the presence of a disk affects the overall size and luminosity measurements of red nuggets, as well as the prospects of decomposing the bulge and disk components, to study derive their structural parameters and eventually their redshift evolution.

Figure 3.7 and Tables 3 and 4 show the best-fit results of the single-component Sérsic fits of the bulge+disk galaxies. With adequate S/N (≥ 100, comparable to red nuggets studied in CANDELS), the presence of a disk has an insignificant effect (a few percent underestimation) on their sizes. This holds over a wide range of sizes ($1 < R_e < 25$ pixels). At much lower S/N values (e.g., ≤ 50), the systematic offsets are about 20%, which is still insignificant compared to the estimated amount of evolution (200%–500%). Conclusion: if red nuggets have structures similar to those of local spiral galaxies, single-component Sérsic fits of these galaxies measure their global sizes robustly. Furthermore, Table 4 shows that the total luminosity of the bulge+disk galaxies can be measured very accurately, too. The Sérsic indices of the best-fit single-component models can be an indicator of the B/T of the galaxy (Fisher & Drory 2008). We found that, at the S/N of observed red nuggets, all the best-fit models with $n \leq 2$ have $B/T < 0.3$. It is more difficult to physically interpret fits with $n \approx 4$, as it can indicate either a high B/T or a galaxy with moderate B/T (e.g., $\sim$0.4) and moderately low S/N (Fig. 3.6, middle panels). Lower values of Sérsic indices are more informative and less difficult to interpret.

We also examine how well one can measure the B/T of disk galaxies and the reliability of the resulting parameters for the bulge and disk components. Figure 3.10 shows that for galaxies with $B/T \geq 0.2$ and at the S/N pertinent to red nuggets, B/T can be accurately measured from fitting a Sérsic + exponential disk model.

The properties of bulges can be measured robustly in galaxies with $B/T \geq 0.4$ and with little to no systematic offsets but with large uncertainties in those with $0.2 \leq B/T < 0.4$ (Fig. 3.12). The best strategy is to leave the Sérsic index of the bulge free, while adding an exponential component for the disk. Fixing the bulge Sérsic index to $n = 4$ introduces systematic biases, apart from removing any information on n. And for galaxies with smaller B/T, measuring the bulge properties is hopeless. This limitation comes from the fact that most of the bulges in this regime have effective radii less than half a pixel. For well-resolved bulges, even at very low B/T, the bulge properties can be measured well.

The properties of the disk are easiest to measure and least subject to serious systematic error (Fig. 3.14). This is expected, as the disk component is the most extended and is least effected by the PSF. As for the case of the bulge mentioned above, the best strategy is to set the bulge Sérsic index free while fixing the disk to an exponential. Of course, this imposes the assumption that the disk follows an exponential light distribution.

3.6 Summary

A considerable fraction of the compact, red massive galaxies at $z \approx 2$ may have a disk component. This motivated us to simulate mock observations of model galaxies to investigate the extent to which a disk component, if present, can be detected under realistic conditions typical of actual observations.

The simulated bulge+disk galaxies span a uniform and wide range of B/T, and we constrain the disk and bulge components to follow empirical scaling relations established for local galaxies. We then rescale these $z \approx 0$ galaxies to mimic the S/N and sizes of galaxies observed at $z \approx 2$. This provides the first set of simulations that allows us to examine the robustness of two-component image decomposition of compact disk galaxies at different B/T.

First, we measure the basic structural parameters using single Sérsic fits, with special emphasis on their sizes. This analysis method is popularly employed in the literature. We then study the robustness of different methods of bulge+disk decomposition of these composite galaxies. Furthermore, we assess the effectiveness of different sky background fitting methods.

For the range of S/N and sizes pertinent to red nuggets, we conclude:

- Modeling bulge+disk galaxies with a single Sérsic component does not bias the sizes too low, by no more than 10%. The apparent compactness of red nuggets is real; it is not the result of missing faint, outer light. However, single-component fits of galaxies with low B/T preferentially leads to relatively larger biases in size and luminosity.

- The B/T can be measured accurately, regardless of the B/T.

- Bulge properties of galaxies with $B/T \gtrsim 0.4$ can be measured robustly. This becomes increasingly difficult for galaxies with B/T below this limit.

- Disk properties are subject to the least amount of systematic and random error, regardless of the B/T.

- Fits with Sérsic indices larger than 6 have larger uncertainties and can cause significant systematic errors. Refitting these galaxies by fixing n to 6 provides more reliable results.

- `GALFIT` can measure the sky value accurately when enough background pixels are available at high S/N. At low S/N, fixing the sky value during the fitting reduces systematic errors.

Bibliography

Barden, M., Rix, H.-W., Somerville, R. S., et al. 2005, ApJ, 635, 959

Barro, G., Faber, S. M., Pérez-González, P. G., et al. 2013, ApJ, 765, 104

Bell, E. F., Wolf, C., Meisenheimer, K., et al. 2004, ApJ, 608, 752

Bernardi, M., Shankar, F., Hyde, J. B., et al. 2010, MNRAS, 404, 2087

Blanton, M. R., Hogg, D. W., Bahcall, N. A., et al. 2003, ApJ, 592, 819

Boroson, T. 1981, ApJl Supp., 46, 177

Bruce, V. A., Dunlop, J. S., McLure, R. J., et al. 2014, MNRAS, 444, 1660

2008ApJ...687L..61B Buitrago, F., Trujillo, I., Conselice, C. J., et al. 2008, ApJl, 687, L61

Cassata, P., Giavalisco, M., Guo, Y., et al. 2010, ApJl, 714, L79

Cassata, P., Giavalisco, M., Guo, Y., et al. 2011, ApJ, 743, 96

Chang, Y.-Y., van der Wel, A., Rix, H.-W., et al. 2013, ApJ, 762, 83

Cimatti, A., Cassata, P., Pozzetti, L., et al. 2008, Astronomy and Astrophysics, 482, 21

Ciotti, L. 1991, Astronomy and Astrophysics, 249, 99

Courteau, S., de Jong, R. S., & Broeils, A. H. 1996, ApJl, 457, L73

Daddi, E., Renzini, A., Pirzkal, N., et al. 2005, ApJl, 626, 680

Damjanov, I., McCarthy, P. J., Abraham, R. G., et al. 2009, ApJ, 695, 101

Davari, R., Ho, L. C., Peng, C. Y., & Huang, S. 2014, ApJ, 787, 69

de Jong, R. S. 1996, Astronomy and Astrophysics, 313, 45

de Vaucouleurs, G. 1948, Annales d'Astrophysique, 11, 247

Dekel, A., & Burkert, A. 2014, MNRAS, 438, 1870

Djorgovski, S., & Davis, M. 1987, ApJ, 313, 59

Dressler, A., Lynden-Bell, D., Burstein, D., et al. 1987, ApJ, 313, 42

Erwin, P., Pohlen, M., & Beckman, J. E. 2008, The Astronomical Journal, 135, 20

Fisher, D. B., & Drory, N. 2008, The Astronomical Journal, 136, 773

Franx, M., Labbé, I., Rudnick, G., et al. 2003, ApJl, 587, L79

Franx, M., van Dokkum, P. G., Schreiber, N. M. F., et al. 2008, ApJ, 688, 770

Freeman, K. C. 1970, ApJ, 160, 811

Fukugita, M., Shimasaku, K., & Ichikawa, T. 1995, Publications of the Astronomical Society of the Pacific, 107, 945

Gadotti, D. A. 2009, MNRAS, 393, 1531

Graham, A. W., & Worley, C. C. 2008, MNRAS, 388, 1708

Grogin, N. A., Kocevski, D. D., Faber, S. M., et al. 2011, ApJl Supp., 197, 35

Hamabe, M., & Kormendy, J. 1987, in IAU Symp. 127, Structure and Dynamics of Elliptical Galaxies, ed. P. T. de Zeeuw & S. D. Tremaine, 379

Häussler, B., McIntosh, D. H., Barden, M., et al. 2007, ApJl Supp., 172, 615

Hogg, D. W., Blanton, M. R., Brinchmann, J., et al. 2004, ApJl, 601, L29

Hopkins, P. F., Bundy, K., Murray, N., et al. 2009, MNRAS, 398, 898

Huang, S., Ho, L. C., Peng, C. Y., Li, Z.-Y., & Barth, A. J. 2013a, ApJ, 766, 47

Huang, S., Ho, L. C., Peng, C. Y., Li, Z.-Y., & Barth, A. J. 2013b, ApJ, 768, L288, L288, L288, L288, L288, L288, L288, L28

Ichikawa, T., Kajisawa, M., & Akhlaghi, M. 2012, MNRAS, 422, 1014

Ishibashi, W., Fabian, A. C., & Canning, R. E. A. 2013, MNRAS, 431, 2350

Jedrzejewski, R. I. 1987, MNRAS, 226, 747

Koekemoer, A. M., Faber, S. M., Ferguson, H. C., et al. 2011, ApJl Supp., 197, 36

Kormendy, J. 1977, ApJ, 218, 333

Kormendy, J., & Barentine, J. C. 2010, ApJl, 715, L176

Kraljic, K., Bournaud, F., & Martig, M. 2012, ApJ, 757, 60

Kriek, M., van Dokkum, P. G., Franx, M., et al. 2006, ApJl, 649, L71

La Barbera, F., Busarello, G., Merluzzi, P., Massarotti, M., & Capaccioli, M. 2003, ApJ, 595, 127

La Barbera, F., de Carvalho, R. R., de La Rosa, I. G., & Lopes, P. A. A. 2010, MNRAS, 408, 1335

Laurikainen, E., Salo, H., Buta, R., Knapen, J. H., & Comerón, S. 2010, MNRAS, 405, 1089

Lawrence, A., Warren, S. J., Almaini, O., et al. 2007, MNRAS, 379, 1599

Longhetti, M., Saracco, P., Severgnini, P., et al. 2007, MNRAS, 374, 614

MacArthur, L. A., Courteau, S., & Holtzman, J. A. 2003, ApJ, 582, 689

Mancini, C., Daddi, E., Renzini, A., et al. 2010, MNRAS, 401, 933

McIntosh, D. H., Bell, E. F., Rix, H.-W., et al. 2005, ApJ, 632, 191

Meert, A., Vikram, V., & Bernardi, M. 2013, MNRAS, 433, 1344

Mosleh, M., Williams, R. J., & Franx, M. 2013, ApJ, 777, 117

Muzzin, A., van Dokkum, P., Franx, M., et al. 2009, ApJl, 706, L188

Newman, A. B., Ellis, R. S., Bundy, K., & Treu, T. 2012, ApJ, 746, 162

Nigoche-Netro, A., Moles, M., Ruelas-Mayorga, A., Franco-Balderas, A., & Kjørgaard, P. 2007, Astronomy and Astrophysics, 472, 773

Nigoche-Netro, A., Ruelas-Mayorga, A., & Franco-Balderas, A. 2008, Astronomy and Astrophysics, 491, 731

Oser, L., Naab, T., Ostriker, J. P., & Johansson, P. H. 2012, ApJ, 744, 63

Papovich, C., Bassett, R., Lotz, J. M., et al. 2012, ApJ, 750, 93

Patel, S. G., van Dokkum, P. G., Franx, M., et al. 2013, ApJ, 766, 15

Peng, C. Y., Ho, L. C., Impey, C. D., & Rix, H.-W. 2002, The Astronomical Journal, 124, 266

Peng, C. Y., Ho, L. C., Impey, C. D., & Rix, H.-W. 2010, The Astronomical Journal, 139, 2097

Poggianti, B. M., Calvi, R., Bindoni, D., et al. 2013, ApJ, 762, 77

Ravindranath, S., Ferguson, H. C., Conselice, C., et al. 2004, ApJl, 604, L9

Robertson, B., Bullock, J. S., Cox, T. J., et al. 2006, ApJ, 645, 986

Ryden, B. S. 2006, ApJ, 641, 773

Saracco, P., Longhetti, M., & Gargiulo, A. 2010, MNRAS, 408, L21

Sérsic, J. L. 1968, Atlas de Galaxias Australes (Córdoba: Obs. Astron., Univ. Nac. Córdoba)

Shen, S., Mo, H. J., White, S. D. M., et al. 2003, MNRAS, 343, 978

Szomoru, D., Franx, M., & van Dokkum, P. G. 2012, ApJ, 749, 121

Szomoru, D., Franx, M., van Dokkum, P. G., et al. 2010, ApJl, 714, L244

Taylor, E. N., Franx, M., Glazebrook, K., et al. 2010, ApJ, 720, 723

Toft, S., van Dokkum, P., Franx, M., et al. 2007, ApJ, 671, 285

Trujillo, I., Cenarro, A. J., de Lorenzo-Cáceres, A., et al. 2009, ApJl, 692, L118

Trujillo, I., Conselice, C. J., Bundy, K., et al. 2007, MNRAS, 382, 109

Valentinuzzi, T., Fritz, J., Poggianti, B. M., et al. 2010, ApJ, 712, 226

van der Wel, A., Bell, E. F., Häussler, B., et al. 2012, ApJl Supp., 203, 24

van der Wel, A., Holden, B. P., Zirm, A. W., et al. 2008, ApJ, 688, 48

van der Wel, A., Rix, H.-W., Wuyts, S., et al. 2011, ApJ, 730, 38

van Dokkum, P. G., & Brammer, G. 2010, ApJl, 718, L73

van Dokkum, P. G., Franx, M., Kriek, M., et al. 2008, ApJl, 677, L5

Williams, C. C., Giavalisco, M., Cassata, P., et al. 2014, ApJ, 780, 1

Williams, R. J., Quadri, R. F., Franx, M., et al. 2010, ApJ, 713, 738

Wuyts, S., Cox, T. J., Hayward, C. C., et al. 2010, ApJ, 722, 1666

Yoon, I., Weinberg, M. D., & Katz, N. 2011, MNRAS, 414, 1625

Chapter 4

Detection of Prominent Stellar Disks in the Progenitors of Present-day Massive Ellipticals

Abstract

Massive galaxies at higher redshifts, $z > 2$, show different characteristics than their local counterparts. They are compact and most likely have a disk. Understanding the evolutionary path of these massive galaxies can give us some clues on how the universe has been behaving in the last 10 billion years. We trace the evolution of local massive galaxies by performing detailed morphological analysis, namely, single Sérsic fittings and bulge+disk decompositions. CANDELS images and catalogues offer an ideal dataset for this study. We analyze about 250 massive galaxies selected from all CANDELS fields (COSMOS, UDS, EGS, GOODS-South and GOODS-North). We confirm that both star-forming and quiescent galaxies have increased their sizes significantly within $0 < z < 2.5$. The global Sérsic index of quiescent galaxies has increased over time (from $n \approx 2.5$ to $n > 4$), while for star-forming galaxies, it stays almost intact ($n \approx 2.5$). The bulge+disk decompositions reveal that massive galaxies at higher redshifts have prominent stellar disks. Furthermore, a considerable fraction of our sample have visually

detectable spiral structures or a thin disk, which further confirms that high-z massive galaxies have a prominent stellar disk. By $z \approx 0.5$, massive quiescent galaxies begin to resemble the local elliptical galaxies. Star-forming galaxies have lower B/T at each redshift bin. Bulges of star-forming and quiescent galaxies follow different evolutionary trajectories, while their disks evolve similarly. We argue that major mergers, along with minor mergers, have played a crucial role in the significant size increase of high-z galaxies and the destruction of their massive and large-scale disks.

4.1 Introduction

Several studies have shown that at $z \approx 2$ a considerable fraction of the massive galaxies ($M_\star \approx 10^{11}$ $M_\odot$) are compact compared to their local counterparts (e.g., Daddi et al. 2005; Toft et al. 2007; Trujillo et al. 2007; Buitrago et al. 2008; Cimatti et al. 2008; Franx et al. 2008; van der Wel et al. 2008; van Dokkum et al. 2008; Damjanov et al. 2009; Hopkins et al. 2009; Cassata et al. 2010, 2011; Mancini et al. 2010; Newman et al. 2012; Szomoru et al. 2012; Barro et al. 2013; Williams et al. 2014). The rarity of compact massive galaxies at the present time implies a considerable size increase in the last 10 billion years (van Dokkum et al. 2008; Trujillo et al. 2009; Taylor et al. 2010; van Dokkum et al. 2010; but see Saracco et al. 2010; Valentinuzzi et al. 2010; Ichikawa et al. 2012; Poggianti et al. 2013). Recent comprehensive simulations found that the commonly used methods for measuring the sizes of these galaxies (single Sérsic) is reliable (e.g., Mosleh et al. 2013; Davari et al. 2014; Davari et al. 2015), despite the fact that their sizes are comparable to the size of the *Hubble Space Telescope (HST)* point-spread function (PSF).

A number of studies have revealed the presence of a stellar disk in these high redshift massive galaxies (van der Wel et al. 2011; Chang et al. 2013; Patel et al. 2013; Bruce et al. 2014). This may come as a surprise as at the local universe, almost all the massive galaxies are ellipticals (van der Wel et al. 2009; Baldry et al. 2012). But considering the fact that during the early universe, the galaxies gas content was higher (Naoz & Barkana 2007; Carilli

& Walter 2013) and therefore gas-rich mergers were more common, it is plausible to observe rotationally supported massive galaxies at those redshifts (Robertson et al. 2006, Ueda et al. 2014). Therefore, besides the observational evidence, tracing back the formation history of local massive ellipticals can give us some clues on why their progenitors may commonly have a disk component (Barro et al. 2013; Toft et al. 2014; van Dokkum et al. 2015).

Local massive elliptical galaxies are found to be old and have a high α/Fe ratio (Thomas et al. 2005) which indicates a short formation timescale at the early epochs. Thomas et al. (2005) show that the the stellar populations of the local massive elliptical galaxies have formed as early as $z = 3$ – 5. They claim that the star formation timescales of these massive galaxies, derived from their high α/Fe ratio, are not more than just a few 100 million years. At $z \approx 3$, using constant cumulative number density (van Dokkum et al. 2010; Patel et al. 2013), these galaxies are found to be as massive as 5×10^{10} $M_\odot$ or more. That means, during that quick mass build up period, these galaxies average star formation rate (SFR) was about several 100 $M_\odot$/yr. In other words, these galaxies have experienced an early episode of violent star formation (i.e., star burst). Gas-rich major mergers are a plausible responsible mechanism for this burst.

Another study which supports this scenario is presented by Toft et al. (2014). They claim that massive red and compact galaxies at $z \approx 2$, the so-called "red nuggets," are the direct descendants of the submillimeter galaxies (SMGs; Blain et al. 2002) at $z > 3$. SMGs are amongst the most luminous, rapidly star-forming galaxies known, with luminosities greater than 10^{12} $L_\odot$ and SFRs of about 10^2 – 10^3 $M_\odot$/yr. (e.g., Kovács et al. 2006; Coppin et al. 2008; Chapman et al. 2010; Magnelli et al. 2010a; Michałowski et al. 2010; Magnelli et al. 2010b; Michałowski et al. 2012). Toft et al. (2014) show that the mass-size distribution of these two classes are similar, besides their mean stellar mass surface density. Both types are best fit by low Sérsic indices. Commonly found SMGs with double peaked CO profiles can be the indicators of major mergers, besides rotation (Frayer et al. 1999; Neri et al. 2003; Sheth et al. 2004; Kneib et al. 2005; Greve et al. 2005; Tacconi et al. 2006; Riechers et al. 2011; Ivison et al. 2013). Toft et al. (2014) show that the majority of SMGs have multiple components or irregularities indicative of ongoing merging and/or clumpy structures. They concluded that red nuggets are the result of gas-rich mergers (Wuyts et al. 2010; Wellons et al. 2015) which led to starbursts. Subsequently, these galaxies are quenched as a result of gas exhaustion, feedback from the starburst, or the ignition of an AGN (Sanders et al. 1988; Hopkins et al. 2006; Wuyts et al. 2010). Besides, the fact that the high-z massive galaxies are compact hints at the necessity of high dissipation on a short timescale (e.g., Naab et al. 2007) which again supports the need for gas-rich major mergers.

Classically, major mergers are believed to transform disky galaxies to bulge-dominated galaxies (Toomre 1977; Barnes & Hernquist 1992). However, more recent and comprehensive simulations show that this may not be always the case. In fact, gas-rich major mergers are commonly found to produce disk-dominated galaxies (Barnes 2002; Robertson et al. 2006; Robertson & Bullock 2008; Hopkins et al. 2009). These disks are believed to form as a result of the gas content that does not lose significant angular momentum during the major merger (Springel & Hernquist 2005). Hopkins et al. (2009) argue that a higher gas fraction increases the chance of forming a disk. In fact, Ueda et al. 2014, by conducting a CO study of 30 local merger remnants, find that the majority of the remnants show kinematical signatures of rotating molecular gas disks. Furthermore, Targett et al. (2013) find that more than 95% of the SMGs (remnants of gas-rich mergers) are either pure disk or disk-dominated. Their Figure 6 shows the wide range of their SMGs axial ratio distribution which rejects the possibility of being dominantly round (i.e., with no disk component).

Therefore, it is expected to observe large-scale stellar disks among the high-z massive galaxies. This hypothesis is attested by a number of studies. van der Wel et al. 2011 show that 50% of their massive galaxies at $z > 2$ are disk-dominated. Similarly, Chang et al. (2013) find that massive galaxies at $z > 1$ have higher axial ratios than their lower redshifts counterparts. Patel et al. (2013) claim that between redshifts 3 and 0, galaxies have become noticeably rounder.

Now the question remains: how have these red, compact, massive, and most likely disk-dominated galaxies at $z \approx 2$ turned into local ginats like M87? We aim to trace this morphological transition and fill in the blank. We do so by performing reliable 2D modeling of the light distributions of massive galaxies within $0.5 < z < 2.5$. Besides performing a simple single Sérsic fitting, when possible, a bulge+disk decomposition of these massive galaxies is executed. Examining the bulge and disk properties, plus the luminosity bulge-to-total ratio (B/T), provides key indicators that can be missed by studying a bulge+disk galaxy as a single system. For instance, Bruce et al. (2014) have performed a comprehensive morphological analysis and find that massive galaxies transition from disk-dominated to bulge-dominated between $z = 3$ and 1, but the emergence of elliptical-like galaxies takes place at lower redshifts. Bruce et al. (2014) bulge+disk decomposition is done by fixing the Sérsic index of the bulge and disk to n=4 and n=1, respectively. In other words, it is assumed that all bulges follow a de Vaucouleurs light profile. Davari et al. (2015) simulations show that this method can lead to biases in measuring the properties of the bulge and the disk, depending on the size and redshift of the galaxy. Besides, by fixing the bulge Sérsic index, one cannot tell how the bulge density and shape is evolving, and an important piece of information is lost. For our study, we use n=free+n=1 method which is shown to be a more reliable method for decomposing a galaxy into its bulge and disk components (Davari et al. 2015).

The Cosmic Assembly Near-infrared Deep Extragalactic Legacy Survey (CANDELS)[1] (Grogin et al. 2011; Koekemoer et al. 2011), one of the largest projects in the history of Hubble, have provided an unprecedented chance of these types of morphological studies. In fact, one of the original science goals of CANDELS is tracing the bulge and disk growth in the rest-frame optical observations at $1 < z < 3$ (see Grogin et al. 2011, "*Cosmic High Noon*"). We take advantage of all wide and deep images taken in the infamous five widely separated fields; GOODS-South & GOODS-North (The Great Observatories Origins Deep Survey; Giavalisco et al. 2004), UDS (UKIDSS Ultra-Deep Survey; Lawrence et al. 2007), COSMOS (The Cosmic Evolution Survey; Scoville et al. 2007a; Scoville et al. 2007b), and EGS (The Extended Groth Strip; Davis et al. 2007). This yields a statistically uniform and robust sample which further mitigates the cosmic variance.

We address three key questions:

[1] `http://candels.ucolick.org/`

1) How does the size and shape of the light distribution (Sérsic index) of star-forming and quiescent massive galaxies evolve?

2) Do the high redshift massive galaxies have a stellar disk component? If yes, how significant is their B/T evolution in the last 10 billion years?

3) What can be learned from the evolution of bulges and disks about the evolutionary passage of massive galaxies?

Our findings show that the massive galaxies were compact and indeed more disk-dominated at higher redshifts and became more bulge-dominated over time. Their local counterparts, massive elliptical galaxies, don't have a large-scale disk. Therefore, major mergers, besides the minor mergers, have played an important role in the significant size increase of high-z galaxies and the destruction of their massive and large-scale disks.

This paper is organized as follows. In Section 2, the details of the sample definition are provided and the employed techniques are described in Section 3. The morphological analysis are presented in Section 4. In Section 5, implications of our results are discussed, and a summary is listed in Section 6. Results are based on a standard cosmology ($H_0 = 71$ km^{-1} s^{-1} Mpc^{-1}, Ω_m = 0.27, and $\Omega_\Lambda = 0.73$) and AB magnitudes.

4.2 Sample Definition

We utilize CANDELS images and catalogues. Besides their high quality near-IR photometry taken with *HST*/WFC3, CANDELS observations are complemented with *HST*/ACS deep visible images, mid-IR with Spitzer Space Telescope, and in the ultraviolet with ground-based observations. This provides a reliable dataset for the photometric redshift and mass measurements.

The photometric redshifts are computed by combining eleven separate measurements explained in Dahlen et al. (2013). Each group used a different combination of photometric redshift code, template spectral energy distributions (SEDs), and priors. TFIT (Laidler et al. 2007) is used to derive the employed photometry components (from U band to mid-infrared). They found that the median $\Delta z/(1+z_{spec}) < 0.01$ (where $\Delta z \equiv z_{spec}$ - z_{phot}) with the RMS of about

0.03. As this study is mostly concerned with broad evolutionary trends between $z \approx 2.5$ to 0.5, precise redshifts for individual objects are not essential to our analysis.

The stellar masses are the median of estimated stellar masses from ten different teams within CANDELS, who used the same photometry and redshifts estimates but with their preferred fitting codes, assumptions, priors, and parameter grid (Mobasher et al. 2015; Santini et al. 2015). Santini et al. (2015) show that, for massive galaxies, there is a good agreement between CANDELS and 3D-HST (Skelton et al. 2014). Mobasher et al. (2015) perform extensive simulations for quantifying the different sources of errors and uncertainties, using the ten independent methods and mock galaxy catalogues with a range of redshifts, masses, and SEDs. They concluded that different methods have comparable scatter, $\sigma(\Delta log(M)) = 0.136$ dex (where $\Delta log(M) \equiv log(M_{estimated})$ - $log(M_{actual})$), with no significant bias.

We employ the CANDELS H band images and the accompanied catalogues for the visible rest-frame analysis of the massive galaxies evolution within $0.5 \leq z \leq 2.5$. The high resolution (pixel scale = $0.06''$), high 5σ limiting magnitudes ($\approx$ 27 mag), and coverage of the five most studied fields (COSMOS, UDS, EGS, GOODS-South and GOODS-North) make this dataset unique and ideal for our photometric analysis.

The most massive galaxies at local universe are almost all quiscent (Baldry et al. 2012). This is not the case at earlier epochs (Whitaker et al. 2011). This means that the massive star-forming galaxies have all quenched over time. Therefore, for tracing back the formation of local massive ellipticals and gleaming a bigger picture, quantifying the evolution of both quiescent and star forming galaxies are required. We use UVJ color-color diagram which can separate quiscent galaxies from reddened star-forming galaxies (see, e.g. Labbé et al. 2006; Wuyts et al. 2007; Williams et al. 2009; Patel et al. 2013). We use Patel et al. (2013) selection criteria for distinguishing these two classes of galaxies (Figure 4.1). Quiescent galaxies populate a region defined by U - V > 1.3, V - J > 1.6, and

$$U - V > 1.08 \times (V - J) + 0.43 \tag{4.1}$$

Table 4.1: H Band Selected Sample

Redshift Bin	$log(M/M_{odot})$ (1)	N (2)	Quiescent Fraction (3)
0.5<z≤1.0	11.02–11.27	31	0.41±0.09
1.0<z≤1.5	10.95–11.20	51	0.37±0.08
1.5<z≤2.0	10.85–11.10	89	0.45±0.10
2.0<z≤2.5	10.74–10.99	77	0.68±0.10

Massive galaxies selected from five different CANDELS fields; COSMOS, UDS, GOODS-South, GOODS-North, & EGS.

Col. (1) Stellar mass range based on constant cumulative number density.
Col. (2) Number of galaxies.
Col. (3) UVJ diagram is used for distinguishing quiescent from star forming galaxies.

where U, V, and J are rest-frame magnitude. Rest-frame photometry calculated using the EAZY photometric redshift code (Brammer et al. 2008) and the templates from Muzzin et al. (2013). Figure 4.2 and Table 1 show our sample fraction of star-forming and quiescent galaxies at different redshifts. It can be seen that at $z = 2.5$ most of the local red massive galaxies were star-forming galaxies. By $z = 1$, the majority of massive galaxies are quenched, in agreement with Brammer et al. (2011) and Patel et al. (2013).

For this study, massive galaxies are selected using the number density selection rather than using a mass limit. Red nuggets are found to have doubled their mass in the last 10 billion years (van Dokkum & Brammer 2010). In other words, local massive galaxies were less massive in the past and could be left out a stellar mass limit selection. Therefore, for tracing back the evolution of massive galaxies, it is more reasonable to select galaxies at a constant cumulative number density (van Dokkum & Brammer 2010; Brammer et al. 2011; Papovich et al. 2011; Patel et al. 2013). We use Patel et al. (2013) criteria for selecting galaxies at a fixed cumulative number density, n_c. Their Figure 2 shows the mass of the galaxies with the cumulative number density equal to 1.4×10^{-4} Mpc^{-3} between $0.25 < z < 3.0$. The chosen n_c correspondes to the number density of galaxies with $M_* \approx 11.2\ M_{sun}$ at $z = 0$ and stellar masses slightly above the mass completeness limit az $z \approx 3$. At redshift 0.5 and 2.5, this number density represents $M_* \approx 11.1$ and $10.8\ M_{sun}$, respectively. By taking into account the stellar mass measurements systematic uncertainties, at each redshift bin, a mass range is determined which corresponds to

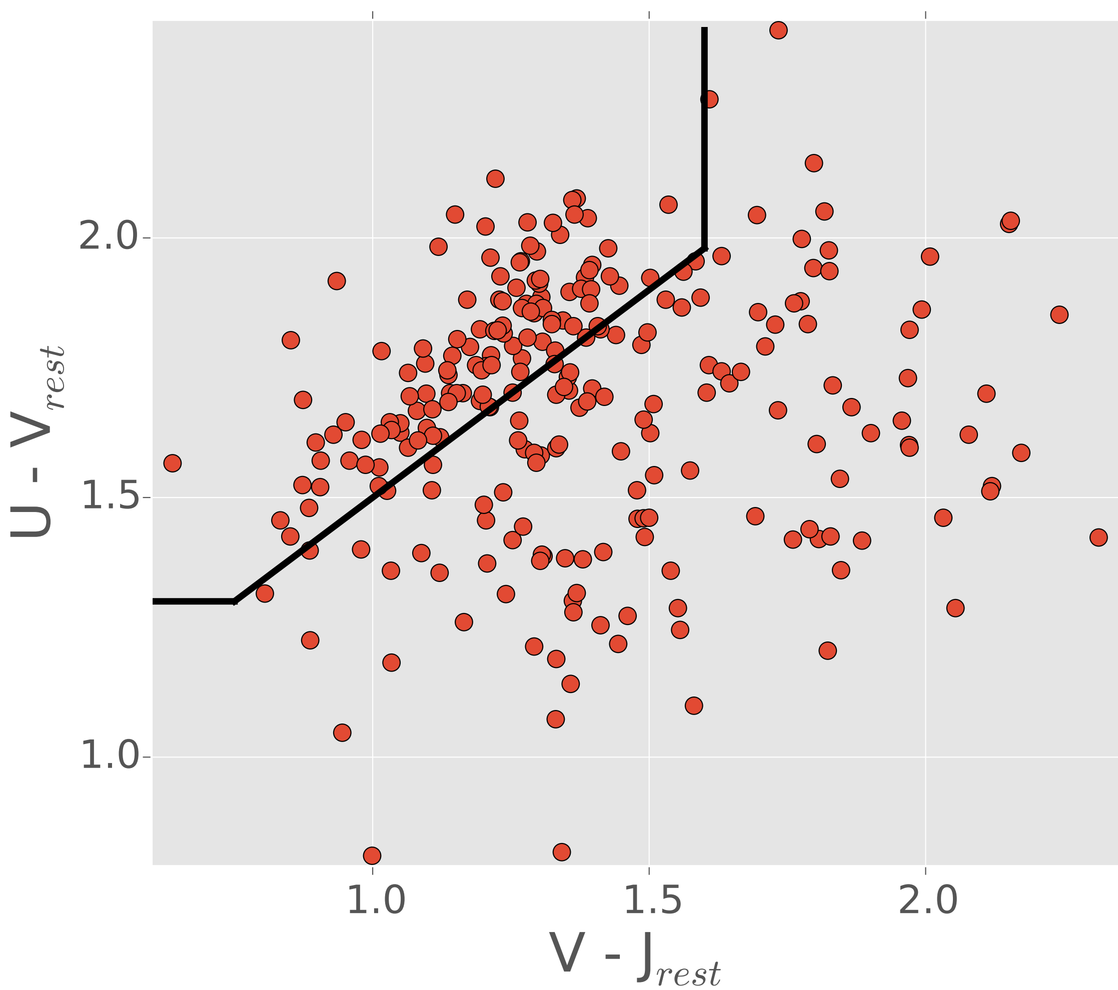

Figure 4.1: UVJ color-color diagram is used for distinguishing quiscent galaxies from star-forming galaxies. The quiescent galaxies populate the top left region of the diagram.

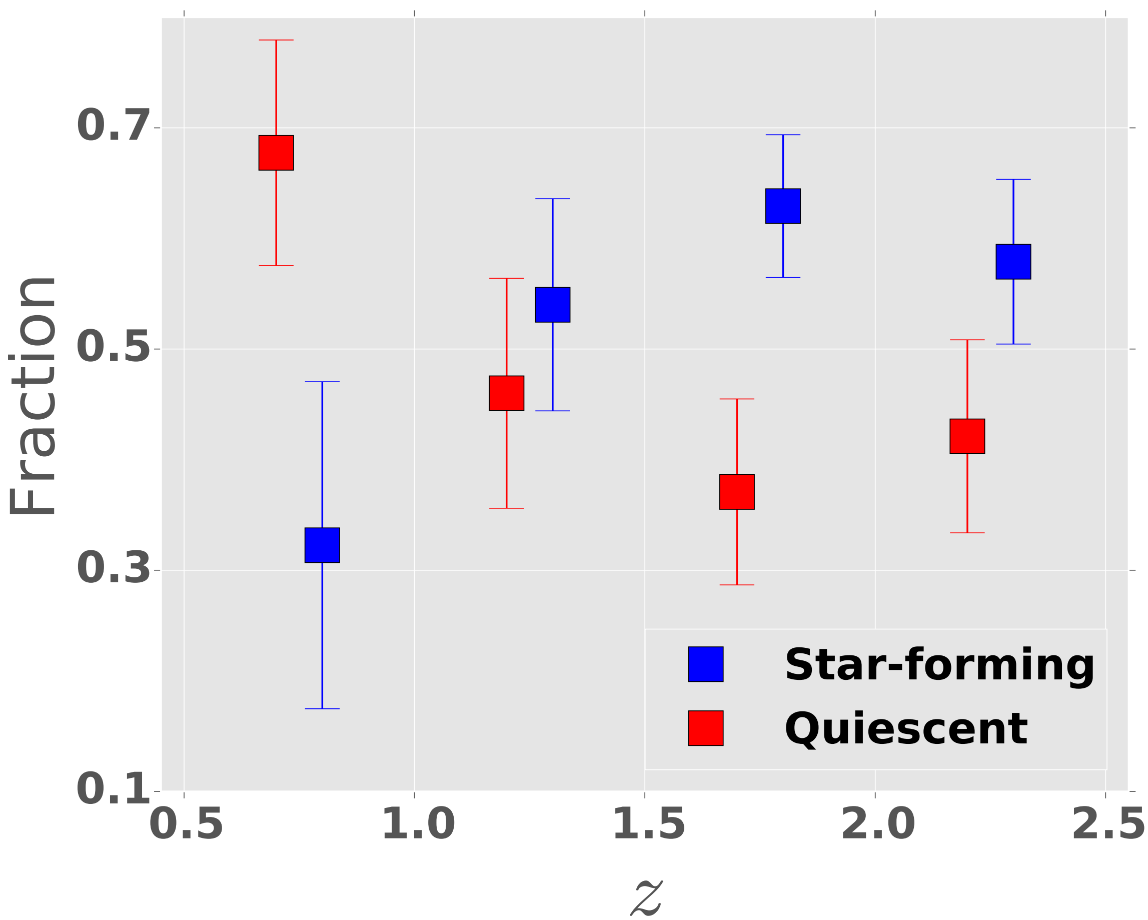

Figure 4.2: Fraction of massive star-forming and quiescent galaxies between $0.5 < z < 2.5$. UVJ color-color diagram is used for distinguishing quiscent galaxies from reddened star-forming galaxies.

the fixed n_c. After removing objects very close to the edge of the images, we are left with about 250 objects. Table 1 shows how many galaxies are in each redshift bin.

4.3 GALFIT Modeling

We use `GALFIT 3.0` (Peng et al. 2010) as the main galaxy modeling tool for this study. GALFIT is a popular, powerful, and simple to use image analysis code that is routinely used for modeling light profile of galaxies and other objects. Out of several commonly used functions in astronomical studies, we mainly use the Sérsic (1968) function to model the surface brightness profiles:

$$\Sigma(R) = \Sigma_e \; exp\left\{-\kappa \left[\left(\frac{R}{R_e}\right)^{1/n} - 1\right]\right\}, \tag{4.2}$$

where Σ_e stands for the surface brightness, R_e is the half-light radius (i.e., effective radius), n is the Sérsic index which is related to the shape of the profile, and κ is a dependent variable on n (Ciotti 1991).

Special interest is given to the Sérsic profile in the morphological studies as the infamous exponential profile ($n = 1$; Freeman 1970) and the $R^{1/4}$ law ($n = 4$; de Vaucouleurs 1948) are the special cases of this profile. These special cases are commonly associated with the disks and elliptical galaxies & (traditionally) bulges and therefore can be used to roughly quantify the B/T (i.e., how bulge/disk-dominated a galaxy is). However, modern studies assume a more general n for bulges (e.g., Blanton et al. 2003; Shen et al. 2003; Bell et al. 2004; Hogg et al. 2004; Ravindranath et al. 2004; Barden et al. 2005; McIntosh et al. 2005; Fisher & Drory 2008).

For performing a GALFIT fitting, a number of components are needed, including: a PSF model, a sigma image, and (sometimes) a bad pixel mask. For each galaxy, we use the H band CANDELS Hybrid PSF corresponding to its field (e.g., UDS, COSMOS, and etc.; van der Wel et al. 2012). These Hybrid PSFs are built by combining a stacked empirical stellar PSF and a TinyTim (Krist et al. 2011) PSF. The CANDELS weight maps are used as the input GALFIT sigma images. The postage stamp of each galaxy is more than 10 – 15 times greater than the size of the galaxy, and as a result, there are several other objects present in that postage stamp. Therefore, providing a bad pixels file is crucial. We use Davari et al. 2014 method for creating the bad pixel fits images. In short, SExtractor[2] (Bertin & Arnouts 1996) is used for detecting the area occupied by the bright objects in the image. Then, those objects are masked by doubling the detected areas by SExtractor.

Depending on the type of GALFIT modeling, initial parameters (guesses) can have a big effect on the fitted model. For single Sérsic fits, unless the initial guesses are so far off the actual values, the initial parameters do not have a major effect. Regardless, we use 1D light profiles obtained by `IRAF/ellipse` (Jedrzejewski 1987) to find reliable initial guesses. By building a galaxy curve-of-growth, the effective radius and total luminosity can be estimated, as well as the axial ratio and position angel (for more details see Davari et al. 2014). Using appropriate initial guesses becomes much more important for the bulge+disk decompositions. For this type of modeling, we again use the obtained 1D light profiles for estimating the initial guesses. Assuming that the disk component of galaxies follows an approximately exponential profile, we look for the straight line part of the galaxy light profile in the logarithmic space. Depending on the B/T, this region locates two to five times R_e away from the center of the galaxy, where the effect of bulge component is minimal. A fitted straight line to that section of light distribution (in logarithmic space) provides an estimate for the disk scale length and its central surface brightness. The obtained total brightness from the single Sérsic is used for finding the total brightness of the bulge component and therefor B/T. Each galaxy is fitted numerous times with different initial guesses for bulge R_e and n plus all the estimated parameters.

While fitting a single Sérsic might require only a few iterations, bulge+disk decompositions can require several fits with different initial guesses. The diagnostic plots (explained below) are a must for evaluating the goodness of a GALFIT fit. Lastly, the fitted sky component is left as a free parameter and its initial values are set to zero. Davari et al. (2014) and Davari et al. (2015) show that once the postage stamp is more than 10 times larger than the galaxy, GAFLIT

[2] `http://www.astromatic.net/software/sextractor`

can measure the sky reliably. Figure 4.3 and 4.4 show the diagnostic plot examples used to examine the goodness of a fit and wether or not a second component is in fact needed. Top left panels show the mean surface brightness (μ) profile of the galaxy, the GALFIT fit model, bulge, and disk components (in cases of bulge+disk decomposition). Bottom left panels show model - galaxy mean surface brightness. The error bars in the left panels are calculated using the image background RMS and galaxy flux measurement error (calculated using ELLIPSE). The right panels, from top to bottom, show the galaxy, the GALFIT model, and the residual (model - galaxy), respectively.

Figure 4.3 top right panel makes it clear that the fitted galaxy has spiral arms. The left panels confirm this fact as there is a non-homology in the galaxy light profile as the single Sérsic model is trying to capture the most of the combination of two components. Figure 4.3 bottom light profile plots show that the bulge+disk decomposition mimics the light profile of the galaxy nicely. And not surprisingly, this galaxy is disk-dominated (i.e. $B/T = 0.05$). On the other hand, Figure 4.4 shows a case where the galaxy is basically a big bulge and adding a second component doesn't improve the model fit significantly. The high B/T of this galaxy (i.e. $B/T = 0.92$) validates this hypothesis.

Davari et al. 2014 and 2015 demonstrate that GALFIT single Sérsic fits with large Sérsic indices ($n > 6$) can lead to significant biases, and one way to remedy that is to refit these galaxies by fixing the n to 6. Note, that before fixing n, it is recommended to try several different initial guesses for the fit and if the problem persists, then it is safe to proceed with fixing n. For our study, we follow the same general rule except the diagnostic plots are given more weight. For example, if fixing n to 4 or 8 gives a better fit and residual than fixing n to 6, then those values are used. Another common case of unreliable model fits is when the effective radius of the bulge component drops below 0.5 pixel. For many of these cases, changing the initial guesses of bulge R_e and n leads to a solution with more realistic R_e values. But if the problem persists, bulge R_e (or sometimes bulge n or both) will be fixed to different initial values and the diagnostic plot will determine which values are the most reliable ones.

Using these general rules, less than 10 out ot 250 galaxies could not be modeled reliably

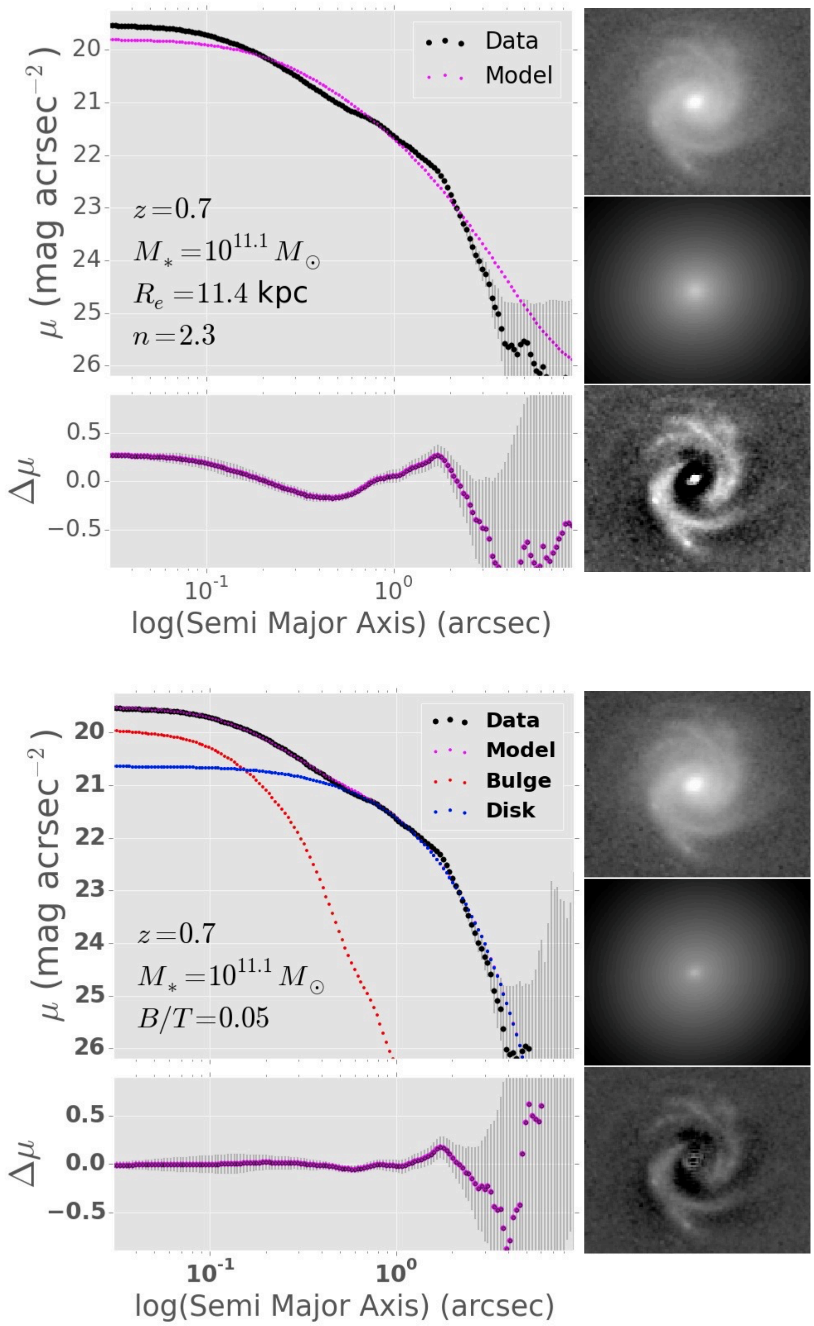

Figure 4.3: Diagnostic plots used to examine the goodness of a fit. Top left panels show the mean surface brightness (μ) profile of the galaxy, the GALFIT fit model, bulge, and disk components (in cases of bulge+disk decomposition). Bottom left panels show the difference between the model - galaxy mean surface brightness. The error bars in the left panels is calculated using the image background value RMS and galaxy flux measurement error using ELLIPSE. The right panels, from top to bottom, show the galaxy, the GALFIT model and the residual (model - galaxy), respectively. Top panel makes it clear that the fitted galaxy has spiral arms and the model is trying to capture the most of the combination of two components (non-homology). bottom light profile plots show that bulge+disk decomposition mimic the light profile of the galaxy nicely.

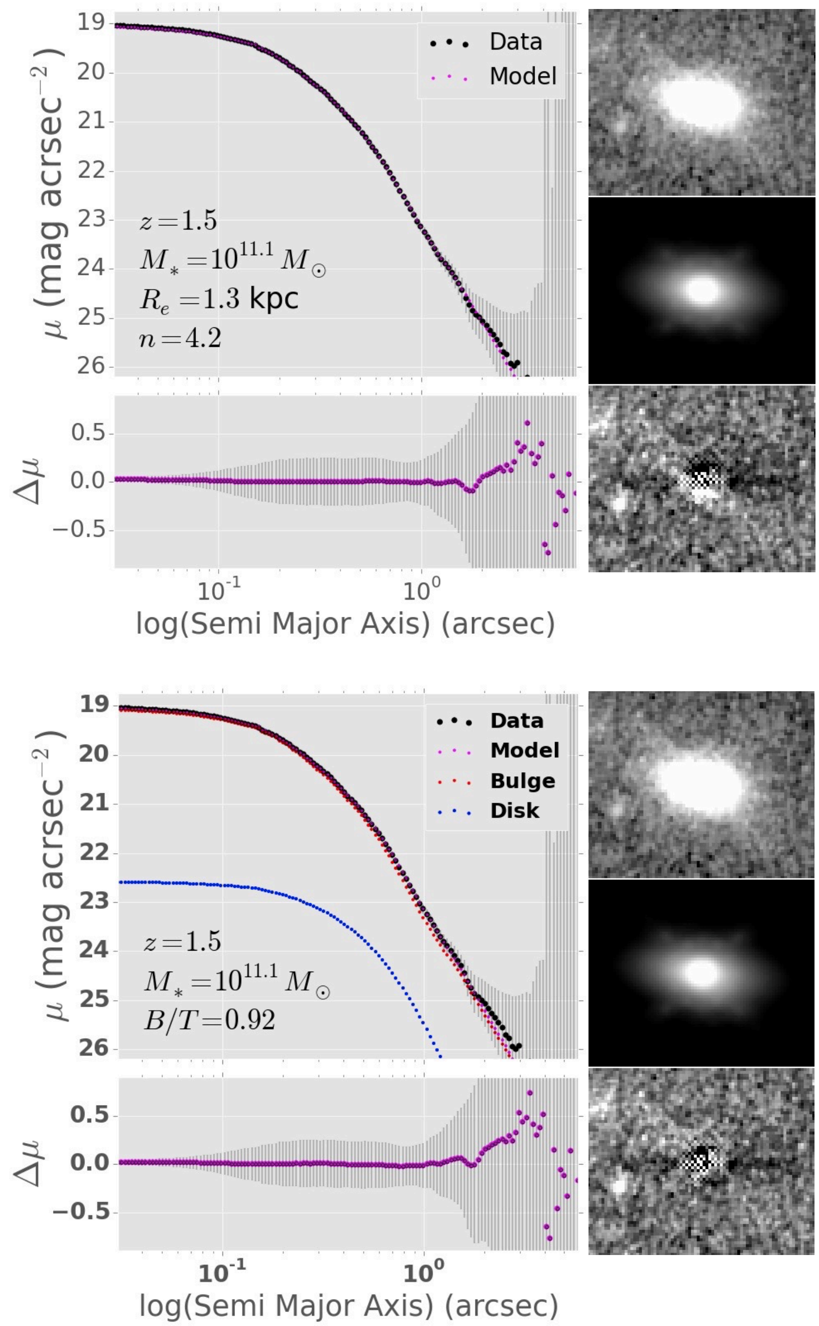

Figure 4.4: Similar to Figure 4.3. This galaxy is basically a big bulge and adding a second component doesn't improve the model fit significantly. The high B/T of this galaxy (i.e. $B/T = 0.92$) validate this hypothesis.

and are left out of the following analysis. In most of these cases, the image contains multiple regions with non-uniform and anomalous background values.

4.4 Results

4.4.1 Fitting Galaxies with Single Sérsic Component

Single Sérsic fitting is probably the most widely adopted method in the literature for morphological studies, at least in recent years. This method provides a rather straightforward and handy way for evaluating some key morphological properties of galaxies: namely size or effective radius (R_e), Sérsic index (n), and ellipticity (e). For instance, if a randomly distributed galaxy population has a significant disk component, we expect a wide distribution of n and e. Davari et al. 2014 and Davari et al. 2015 simulations show that single component fits of massive, bright galaxies at the redshift range of interest can be measured with little to no systematic errors or uncertainties.

Figure 4.5 summarizes the results of single Sérsic fitting of massive galaxies within $0.5 < z < 2.5$. Red, blue, and black filled boxes show the median in each redshift bin for quiescent, star-forming, and combined, respectively. The error bars correspond to the interquartile range of different measurements. The gray filled diamonds show the median values for a sample from GAMA data release 2 (Driver et al. 2009; Liske et al. 2015). The sample mass range corresponds to our number density selection (i.e., $M_\star = 10^{11.1} - 10^{11.3}\ M_\odot$) at $0 < z < 0.5$. The related morphological parameters are derived by single Sérsic fitting, consistent with our method.

To quantify the significance of the observed evolution of different properties of galaxies, two statistical tests are performed: two sample Kolmogorov-Smirnov test (KS) and one-way analysis of variance (ANOVA). KS is used to test whether the star-forming and quiescent sample quantities come from the same distribution. The KS has the advantage of making no assumption about the distribution of data. (i.e, non-parametric.) The result of KS is summarized by two quantities: D-value and p-value. D-value shows the maximum difference between the empirical cumulative distribution functions of the two samples, while p-value indicates the significance

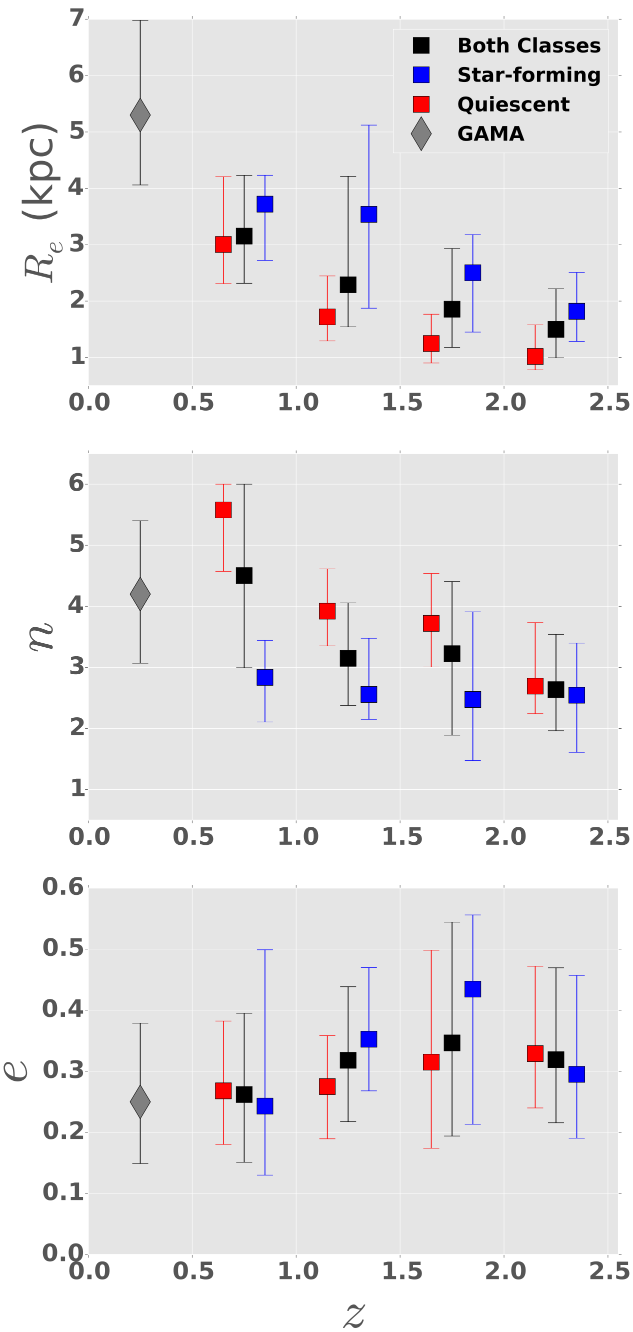

Figure 4.5: Results of single Sérsic fitting of massive galaxies between $0.5 < z < 2.5$. Top, middle, and bottom panels show the evolution of effective radius (R_e) in kiloparsec, Sérsic index (n), and ellipticity (e), respectively. Red, blue and black filled boxes show the median in each redshift bin for quiescent, star-forming, and combined, respectively. The error bars corresponds to the interquartile range of different measurements. The gray filled diamond show the median values for a sample from GAMA data release 2 with mass range corresponding to our number density selection criteria.

Table 4.2: Single Sérsic Fits Statistical Tests Results

	ANOVA		KS	
Variable (1)	F-value (2)	p-value (3)	D-value (4)	p-value (5)
R_e	20.39	0.00	0.28	0.00
n	9.98	0.00	0.35	0.00
e	1.66	0.18	0.15	0.14

Col. (1) Parameters measured using Single Sérsic fitting.
Col. (2) (variance of sample means at different redshift bins) / (variance of the whole sample)
Col. (3) Small p-values (< 0.05) reject the null-hypothesis that the means values are not statistically different at different redshift bins.
Col. (4) The maximum difference between the empirical cumulative distribution functions of the two samples.
Col. (5) Small p-values (< 0.05) reject the null-hypothesis that the two samples are drawn from the same distribution.

of the difference between two samples. Small p-values (< 0.05) reject the null-hypothesis that the two samples are drawn from the same distribution. ANOVA is used to determine whether or not there are any statistically significant differences between the means of sample quantities in our redshift bins. F-value (i.e., F statistics) and p-value summarize the results of ANOVA, where F-value quantifies the variance between groups compared to the variance within groups: (variance of sample means at different redshift bins) / (variance of the whole sample). High F-values (i.e., small p-values) reject the null-hypothesis that the means values are not statistically different at different redshift bins are not significantly different and therefore it can be concluded that there is an evolution over the observed redshift range. Single Sérsic fits KS and ANOVA test results are listed in Table 2.

Figure 4.5 top panel shows the significant size evolution. Based on Table 3, the size increase is more prominent for quiescent galaxies. The quiescent galaxies have increased their sizes by a factor of three down to $z = 0.5$ and more than five by $z = 0$. However, the amount of size increase for both star-forming and quiescent galaxies are comparable between $z = 2.5$ and $z = 0.5$; about 2 kpc. The size-mass relation slope of massive galaxies are consistent with the value found in van Dokkum et al. (2010) and Patel et al. (2013). In average, the size interquartile ranges are smaller for quiescent galaxies which indicates a greater size diversity among star

Table 4.3: Quantifying the Size Evolutions

Variable	Quiescent	Star-forming	Both
R_e	-1.75±0.16	-1.17±0.31	-1.19±0.03
$R_{e_{bulge}}$	-2.55±0.43	-1.61±0.17	-2.38±0.43
h	-1.60±0.07	-1.14±0.15	-1.27±0.06

The evolution of the bulge, disk, and global sizes are quantified using $parameter \propto (1{+}z)^{\alpha}$. The α values for the star-forming, quiescent, and both classes are listed.

forming galaxies. In other words, quiescent galaxies sizes are more homogenous. Furthermore, the star-forming galaxies at each redshift are larger than quiescent galaxies, in agreement with previous similar studies (e.g., Zirm et al. (2007); Szomoru et al. 2011; Whitaker et al. 2011; Patel et al. 2013; and Williams et al. 2014). Table 2 confirms that the star-forming and quiescent galaxies have different size distributions and there is a statistically significant size evolution at the observed redshift range.

Figure 4.5 middle panel shows how the global Sérsic indices of star-forming and quiescent galaxies have evolved. At higher redshift, the Sérsic indices of both classes are very similar ($n \approx 2.5$), consistent with a composite bulge+disk system. But over time, the difference becomes more and more prominent. The Sérsic index of star-forming galaxies stays almost intact while for quiescent galaxies, it increases significantly. At the lowest redshift bins, the median Sérsic indices of quiescent galaxies resemble that of local elliptical galaxies ($n > 4$). Morishita et al. (2014) finds that the Sérsic indices of massive quiescent galaxies have increased significantly from $0.5 < z < 2.5$ and remains almost the same for star-forming galaxies, in agreement with our results. Patel et al. 2013 find a similar trend for massive quiescent galaxies and a less significant increase for star-forming ones. Szomoru et al. (2011) also finds lower Sérsic indices for galaxies with higher star formation rates. Table 2 shows that the star-forming and quiescent galaxies have different global Sérsic index distributions and their mean values have evolved over time.

Although it seems that the ellipticity of massive galaxies have decreased between $z = 2.5$ and $z = 0$ (Figure 4.5 bottom panel), Table 2 ANOVA p-value indicates no statistically significant deference between their ellipticity means at different redshift bins. Furthermore, the KS p-value shows that the distribution of star-forming and quiescent galaxies ellipticity are statistically indistinguishable. At higher redshift bins, both classes have a wider range of ellipticity which can be an indicator of a disk component in these galaxies.

Table 2 ANOVA p-value for the ellipticity of massive galaxies indicates no statistically significant deference between their e means at different redshift bins. However, comparing only our highest and lowest redshift bins shows a drop in the overal ellipticity of the massive galaxies. The two sample *one-sided* t-test gives a p-value=0.05, which rejects the null-hypothesis that the $2.0 < z < 2.5$ and $0.5 < z < 1.0$ galaxies ellipticity means are not statistically different. Whitaker et al. (2011) and Patel et al. (2013) also concluded that local massive galaxies seem rounder. The KS p-value shows that the distribution of star-forming and quiescent galaxies ellipticity are statistically indistinguishable. At higher redshift bins, both classes have a wider range of ellipticity which can be an indicator of a disk component in these galaxies. On the other hand, the ellipticity distribution of local elliptical galaxies (i.e., GAMA results) and galaxies at $0.5 < z < 1.0$ are almost identical.

4.4.2 Fitting Galaxies with Two Components

While single Sérsic fitting provides a reliable first order estimate of morphological properties, decomposing a galaxy into its bulge and disk components can reveal a new set of valuable galaxy evolution indicators. Davari et al. (2015) simulations show that B/T of high redshift bulge+disk systems can be potentially measured accurately without imposing any constraints on the light profile shape of the bulge. However, due to the small sizes of bulges at high redshifts, fitted bulge properties are reliable only for galaxies with $B/T \geq 0.2$, unless the bulge size is about one pixel or greater. The disk component, by contrast, can be measured with little difficulty.

Figure 4.6 top panel reveals how the B/T of massive galaxies has changed between $z = 2.5$ and $z = 0.5$. At higher redshifts, the quiescent galaxies have intermediate B/T (≈ 0.4) and over time became more and more bulge-dominated. At the lowest redshift bin, these quiescent galaxies (with $B/T \approx 0.8$) begin to resemble the local massive elliptical galaxies. Although,

Table 4.4: Bulge+Disk Decomposition Statistical Tests Results

	ANOVA		KS	
Variable (1)	F-value (2)	p-value (3)	D-value (4)	p-value (5)
B/T	13.36	0.00	0.49	0.00
m_{bulge}	12.93	0.00	0.49	0.00
m_{disk}	6.93	0.00	0.22	0.01
$R_{e_{bulge}}$	30.77	0.00	0.21	0.01
n_{bulge}	17.92	0.00	0.24	0.00
e_{bulge}	9.10	0.00	0.34	0.00
h	32.38	0.00	0.11	0.40
e_{disk}	0.09	0.97	0.10	0.51

Col. (1) Parameters measured using Single Sérsic fitting.
Col. (2) (variance of sample means at different redshift bins) / (variance of the whole sample)
Col. (3) Small p-values (< 0.05) reject the null-hypothesis that the means values are not statistically different at different redshift bins.
Col. (4) The maximum difference between the empirical cumulative distribution functions of the two samples.
Col. (5) Small p-values (< 0.05) reject the null-hypothesis that the two samples are drawn from the same distribution.

star-forming galaxies have also become more bulge-dominated, their B/T at all redshift bins are less than that of their quiescent counterparts. Table 4 confirms that star-forming and quiescent galaxies have different B/T distributions. Similarly, Bruce et al. (2012) find that massive galaxies at $z > 2$ are mostly disk-dominated and by $1 < z < 2$ have increased their B/T to intermediate values with very few elliptical like galaxies down to $z = 1$. They show that disk-dominated galaxies have a higher SFR which translates into star-forming galaxies having a lower B/T. Lang et al. (2014) results also show a increase in B/T between $1.5 < z < 2.5$ and $0.5 < z < 1.5$ for massive galaxies.

Figure 4.6 middle and bottom panels show that while bulges of both types of galaxies have become brighter over time, the disks of quiescent galaxies are disappearing. Meanwhile, the star-forming galaxies disks are becoming brighter at lower redshift bins. Figure 4.6 middle panel shows that the bulge magnitudes of quiescent galaxies have significantly smaller scatters than star-forming galaxies. This can indicate a more homogenous formation and evolution history of quiescent galaxies bulges. Furthermore, it can be seen that the bulges of quiescent

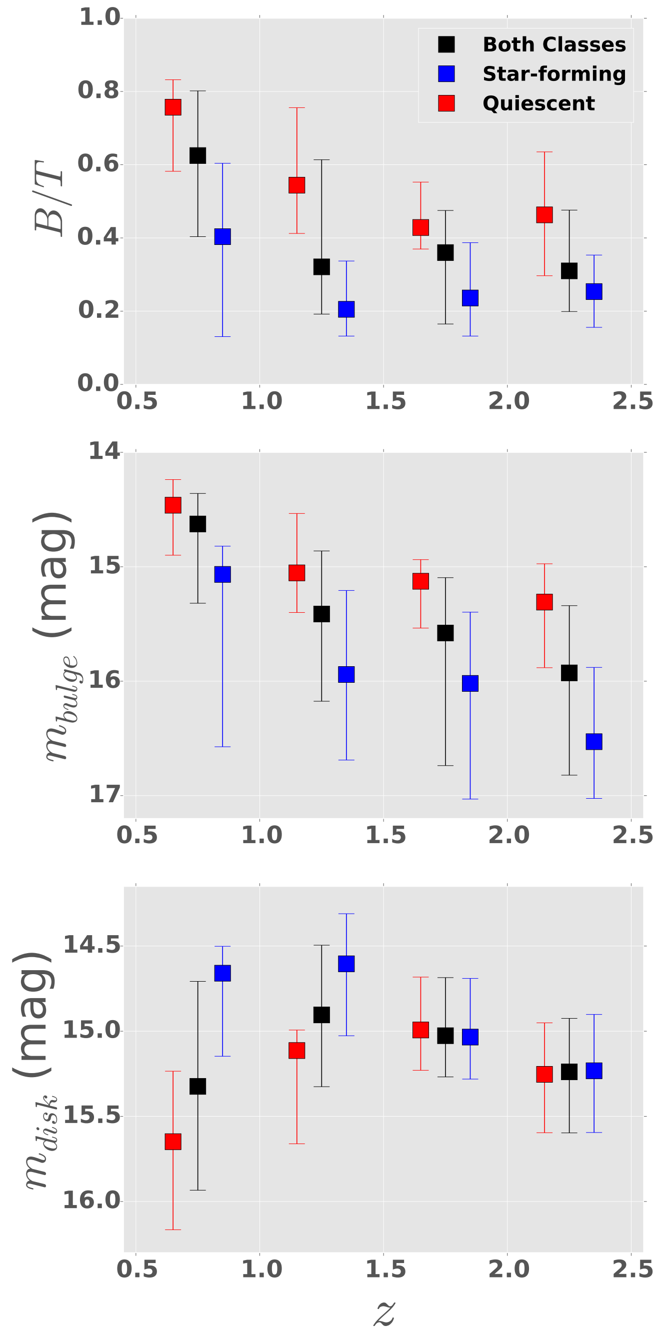

Figure 4.6: Results of bulge+disk decomposition of massive galaxies between $0.5 < z < 2.5$. Top, middle, and bottom panels show the evolution of flux bulge-to-total ratio (B/T), bulge magnitude (m_{bulge}), and disk magnitude (m_{disk}), respectively. Red, blue and black filled boxes show the median in each redshift bin for quiescent, star-forming, and combined, respectively. The error bars corresponds to the interquartile range of different measurements.

galaxies, at all redshifts, are brighter than their star-forming counterparts. Table 4 shows that bulge and disk magnitude distributions of both types of galaxies are different and have evolved between redshift 2.5 and 0.5.

Top panel of Figure 4.7 and Table 3 reinforces the size evolution observed by single Sérsic GALFIT models (Figure 4.5 top panel). The bulges of both classes of galaxies have grown, and once more, this evolution is greater for quiescent galaxies. The disk scale lengths (Figure 4.7 top panel) of both star-forming and quiescent galaxies have increased, as well, but Table 4 shows that their distributions are not distinguishable. Table 3 indicates that the disk size increase is less significant compared to the bulge component.

As shown in Figure 4.7 middle panel, the Sérsic indices of quiescent galaxies bulges have increased considerably but stayed almost the same for star-forming massive galaxies. This is similar to the results of single Sérsic analysis (Figure 4.5 middle panel). By redshift 0.5, bulges of quiescent galaxies have Sérsic indices similar to the local ellipticals and classical bulges (Fisher & Drory 2008).

Figure 4.8 bottom panel and Table 4 shows that the disk ellipticity of both classes have similar distribution and have not changed between $z = 2.5$ and 0.5. On the other hand, the bulges of massive galaxies have become rounder in this period. Quiescent galaxies have lower bulge ellipticity and by $z = 0.5$, their distribution is similar to those of the local massive ellipticals and classical bulges (Fathi & Peletier 2003).

4.5 Implications for Galaxy Evolution

4.5.1 Red Nuggets

The discovery of red nuggets has captured a lot of attention in the recent years as it requires more critical thinking about how the local massive elliptical galaxies have formed and what has been their evolutionary history. Observed compactness of red nuggets at $z \approx 2$ raised the question of whether the massive red galaxies have indeed increased their sizes by a factor of roughly 3 – 5 while maintaining their passive state, or have there been flaws with the size

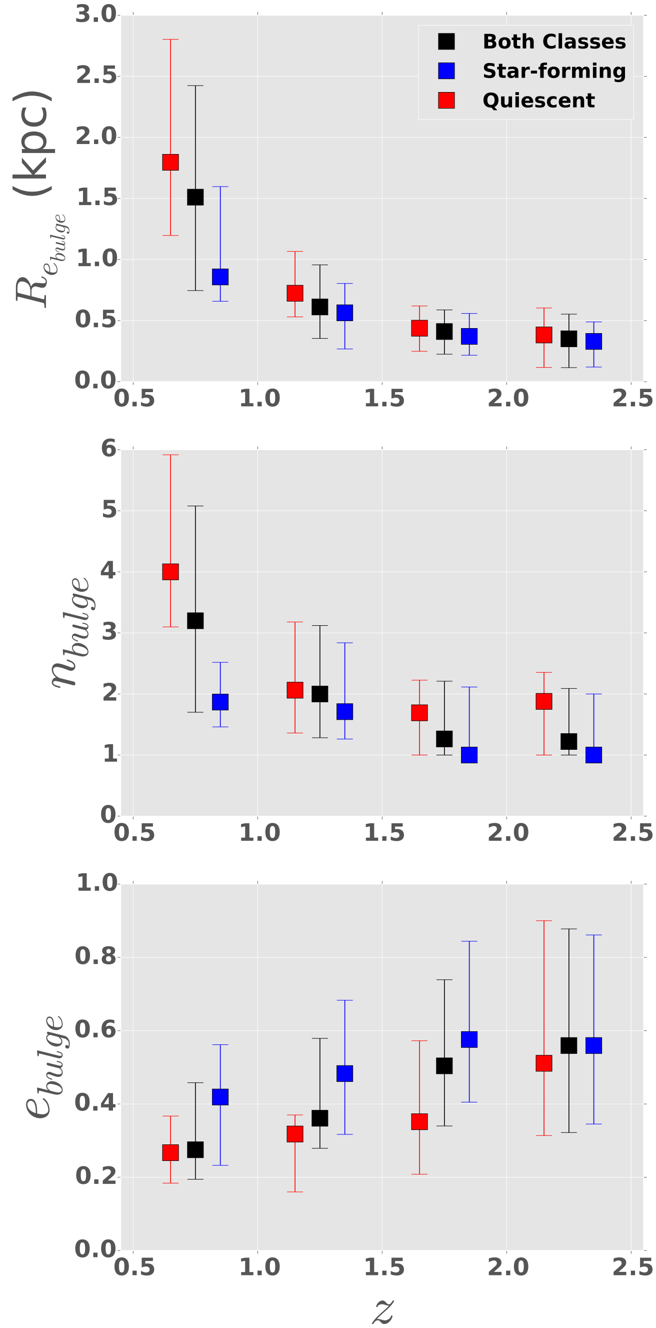

Figure 4.7: Results of bulge+disk decomposition of massive galaxies between $0.5 < z < 2.5$. Top, middle, and bottom panels show the evolution of bulge effective radius ($R_{e_{bulge}}$) in kiloparsec, bulge Sérsic (n_{bulge}), and bulge ellipticity (e_{bulge}), respectively. Red, blue and black filled boxes show the median in each redshift bin for quiescent, star-forming, and combined, respectively. The error bars corresponds to the interquartile range of different measurements.

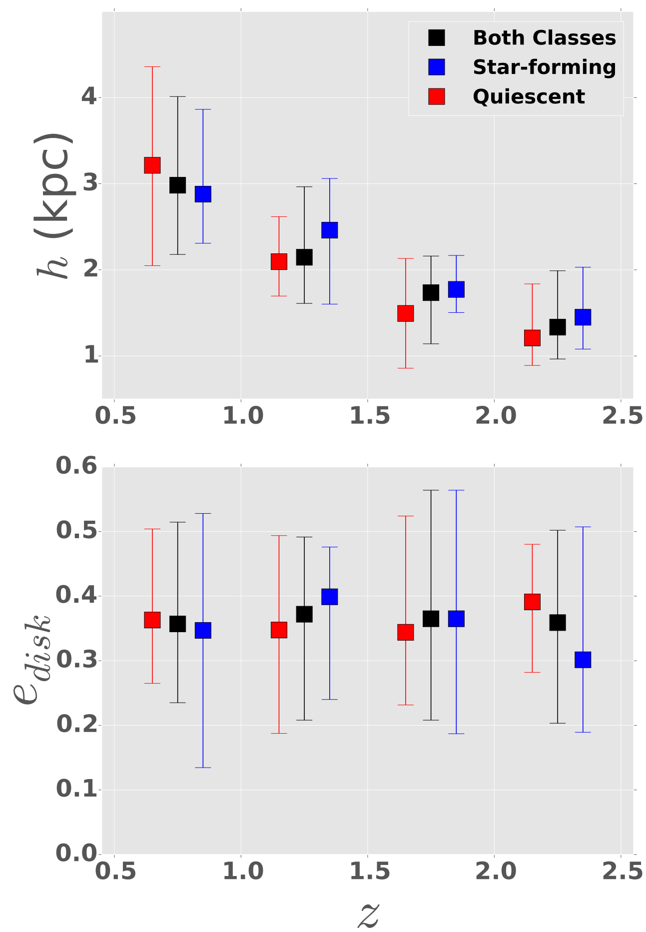

Figure 4.8: Results of bulge+disk decomposition of massive galaxies between $0.5 < z < 2.5$. Top, and bottom panels show the evolution of disk scale length (h) in kiloparsec, and disk ellipticity (e_{disk}), respectively. Red, blue and black filled boxes show the median in each redshift bin for quiescent, star-forming, and combined, respectively. The error bars corresponds to the interquartile range of different measurements.

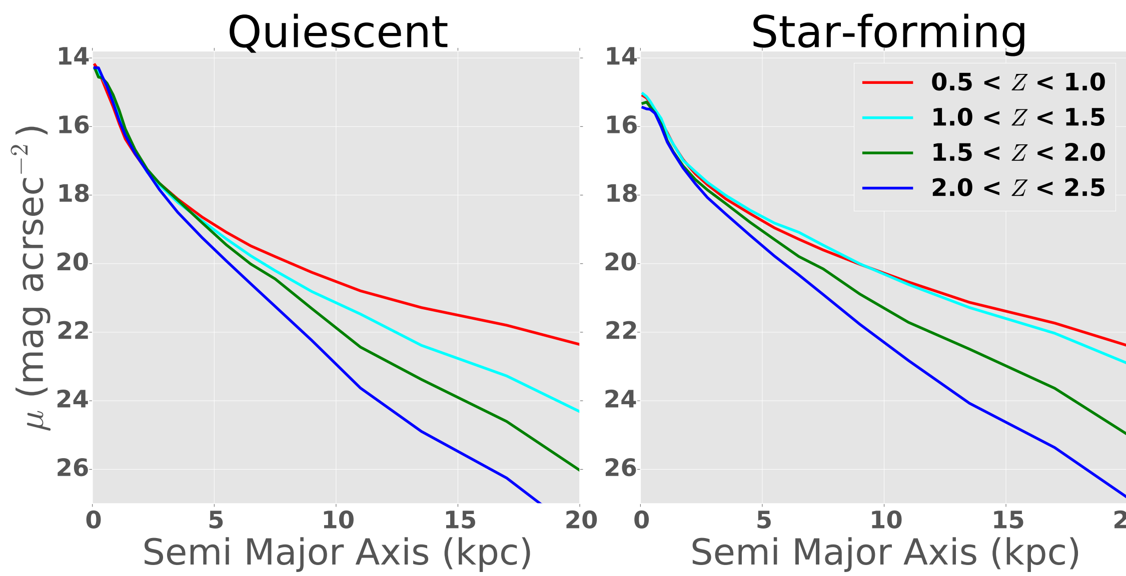

Figure 4.9: The inside-out growth of massive galaxies. Median light distributions of massive quiescent and star-forming galaxies are shown in four redshift bins. While the inner few kiloparsecs of these galaxies has been almost intact since $z \approx 2.5$, over time more material is accreted in their outskirts. Quiescent galaxies accretion continues at least down to $z \approx 0.5$, while it seems that star-forming galaxies stop accreting by $z \approx 1.0$. The inner region of quiescent galaxies are brighter and have a higher density.

measurement methods employed? Recent extensive simulations (Mosleh et al. 2013; Davari et al. 2014; Davari et al. 2015), besides the consistent results of multiple independent studies (e.g., Daddi et al. 2005; Toft et al. 2007; Trujillo et al. 2007; Buitrago et al. 2008; Cimatti et al. 2008; Franx et al. 2008; van der Wel et al. 2008; van Dokkum et al. 2008; Damjanov et al. 2009; Cassata et al. 2010; Newman et al. 2012; Szomoru et al. 2012), have minimized skepticism. Figure 4.5 confirms that massive galaxies at $z \approx 2$ were compact and over the next 10 billion years, their sizes have increased significantly. Figure 4.9 shows that these galaxies have grown inside-out (Patel et al. 2013; Huang et al. 2013). Figure 4.9 shows the median light distribution of massive quiescent and star-forming galaxies in four redshift bins. While the inner few kiloparsec of these galaxies have been almost unchanged since $z \approx 2.5$, over time more and more material is accreted in their outskirts. Quiescent galaxies accretion continues at least down to $z \approx 0.5$, while it seems that star-forming ones stop accreting by $z \approx 1.0$.

The compactness of the red massive galaxies at higher redshifts and their similarities to

Table 4.5: Estimated Fraction of Massive Galaxies with a Prominent Stellar Disk Using Different Diagnostics

	$B/T \leq 0.5$ (1)			Spiral Structures (2)			Edge-on Disks (3)		
redshift bin	Quiescent	Star-forming	Both	Quiescent	Star-forming	Both	Quiescent	Star-forming	Both
$0.5<z\leq1.0$	0.17±0.07	0.67±0.11	0.36±0.07	0.05± 0.04	0.30±0.14	0.13±0.06	0	0.10±0.09	0.03±0.03
$0.5<z\leq1.5$	0.50±0.12	0.86±0.06	0.72±0.06	0	0.67±0.09	0.37±0.07	0.09±0.06	0.19±0.07	0.14±0.05
$1.5<z\leq2.0$	0.64±0.09	0.90±0.04	0.81±0.05	0	0.18±0.05	0.11±0.03	0.12±0.06	0.13±0.04	0.12±0.03
$2.0<z\leq2.5$	0.53±0.09	0.93±0.04	0.77±0.05	0	0.05±0.03	0.03±0.02	0.13±0.06	0.09±0.04	0.11±0.04

Col. (1) Massive galaxies with bulge-to-total ratios less than 0.5.
Col. (2) Massive galaxies with visually detectable spiral structures.
Col. (3) Edge-one massive galaxies with $e > 0.6$.

SMGs reveal the high dissipation at their early formation epochs which in turn led to the starburst and subsequently potential disk formation (e.g., Targett et al. 2013; Toft et al. 2014). This raises some important questions: How have the morphology of these red massive galaxies changed since the universe was only about 2 billion years old? Are the red nugget light distributions similar to their local counterparts, or in fact, do they have more than one component; bulge+disk? Table 5 shows the estimated fraction of galaxies with a prominent stellar disks using three different diagnostics: galaxies with $B/T < 0.5$, visually detectable spiral structures, and edge-one galaxies with $e > 0.6$ (see the next section.) Table 5 confirms the presence of prominent stellar disks among high-z massive galaxies. This further reinforces that the progenitors of massive elliptical galaxies have notable different characteristics from their local counterparts and have evolved significantly since $z = 2.5$. Our study traces this gradual transition. By $z = 0.5$, B/T of red massive galaxies is high and their stellar disk component is nearly destroyed (Figure 4.6), their global and bulge Sérsic index is similar to a de Vaucouleurs light profile (Figure 4.5 and Figure 4.7), and their bulge axial ratio distribution is similar to their local counterparts. All these indicators confirm the fact that red nuggets are in fact the ancestors of local massive ellipticals. But how are their disks destroyed? Can this be accomplished by minor mergers alone or are major mergers required?

Another key player in the plausible evolutionary scenarios, which has captured less attention, are the compact blue galaxies; blue nuggets. Figure 4.5 shows that, although star-forming galaxies are larger than quiescent galaxies at each redshift bin, at high redshifts, these galaxies are compact, as well. Studies have shown that local massive star-forming galaxies are rare (e.g., Baldry et al. 2012). Therefore, most of these high redshift blue nuggets have turned into red nuggets. Figure 4.2 illustrates how over time the massive star-forming galaxies evolve into red massive galaxies. Besides, Figure 4.6 shows that at each redshift, the B/T and bulge surface density of quiscent galaxies are higher. Therefore, the star formation shut-off and increase in the B/T, and global & bulge n (Figure 4.5 and 4.7) coincide. Furthermore, considering the fact that the disks of quiescent and star-forming galaxies at each redshift bin have more or less similar characteristics (Figure 4.8), one can conclude that the distinct evolutionary path of these two classes can be explained by how their bulge components have evolved.

One possible explanation for the increasing fraction of quiescent galaxies, inside-out growth, and disappearance of the disks is mergers. The tidal features and streams seen in deep imaging of local massive quiescent galaxies support the role of mergers in their evolutionary history (van Dokkum 2005; Tal et al. 2009; Janowiecki et al. 2010). Furthermore, the mass increase of red galaxies after being quenched (van Dokkum et al. 2010) supports the growth via mergers.

Minor mergers are considered as the most plausible mechanism for explaining the size evolution of red nuggets into local massive elliptical galaxies (e.g., Bournaud et al. 2007; Bezanson et al. 2009; Hopkins et al. 2009; Naab et al. 2009; van Dokkum et al. 2010; Oser et al. 2012; Hilz et al. 2013). Welker et al. (2015) show that dry minor and major mergers are significantly more effective at increasing the sizes of massive compact galaxies. They find that dry mergers (consistent with Hilz et al. 2013) produces $R_e \propto M^\alpha$ with $\alpha \approx 2$. We find a similar α for our quiescent massive galaxies between redshift 2.5 and 0.5, $\alpha =$ -1.76 $\pm$ 0.16. However, this value is considerably smaller for star-forming galaxies with $\alpha =$ -1.17 $\pm$ 0.30. Welker et al. (2015) also show that by $z \approx 1$, more than 80% their massive galaxies ($M_\star > 10^{10.5}\ M_\odot$) have experienced minor mergers. Hopkins et al. (2010) show that the merger rate is expected, on average, to increase monotonically with the stellar mass, and therefore can be even higher for our sample. Figure 4.10 demonstrates that the residuals of galaxy images after the removal of the bulge+disk model, a more reliable visual inspection of disturbed morphologies and potentially nearby merging objects can be achieved. Our visual inspection shows that at $0.5 < x < 1.0$, more than 60% of quiescent galaxies have nearby objects or show merger signatures (e.g., distortion, tidal tails, and shells). At the same redshift, that fraction is about 40% for star-forming galaxies. Merger candidate fractions for both classes are abut 30% at $1.0 < x < 1.5$ and drops significantly beyond that. This drop can be caused by the surface brightness dimming effect. While these fractions are by no means indicators of massive galaxies merger fractions at those redshifts, it shows that at $z < 1.5$, mergers can play a significant role in size and morphology evolution of these galaxies.

On the other hand, it is not clear whether minor mergers can destroy the prominent stellar disks observed in high-z massive galaxies. Major mergers are classically considered as the main physical driver for getting rid of the disk or the bulge formation. Hopkins et al. (2010) find that major mergers are needed for forming galaxies with high B/T. Furthermore, Bernardi et al. (2011) concluded that major mergers dominate the assembly history of massive early-type galaxies based on the their scaling relations.

Although H band images of galaxies at different redshift bins capture the flux in different rest-frame bands (i.e., V to approximately I band), comprehensive multi-wavelength studies of local galaxies have found that B/T does not have a strong dependence on the observed rest-frame wavelength range (e.g., Schulz et al. 2003; Graham & Worley 2008). The observed B/T differences between different bands is not greater than 0.1. Additionally, for quiescent galaxies less color gradient and therefore dependence of B/T on the observed rest-frame flux is expected.

4.5.2 Further Evidence of Prominent Stellar Disks: Detection of Spiral Structures and Thin Disks

Despite the prevalence of the spiral structures in the local universe (e.g., Lintott et al. 2011; Willett et al. 2013), these features are not believed to be common among the star forming galaxies at higher redshifts (e.g., Conselice et al. 2005; Bournaud & Elmegreen 2009; Conselice

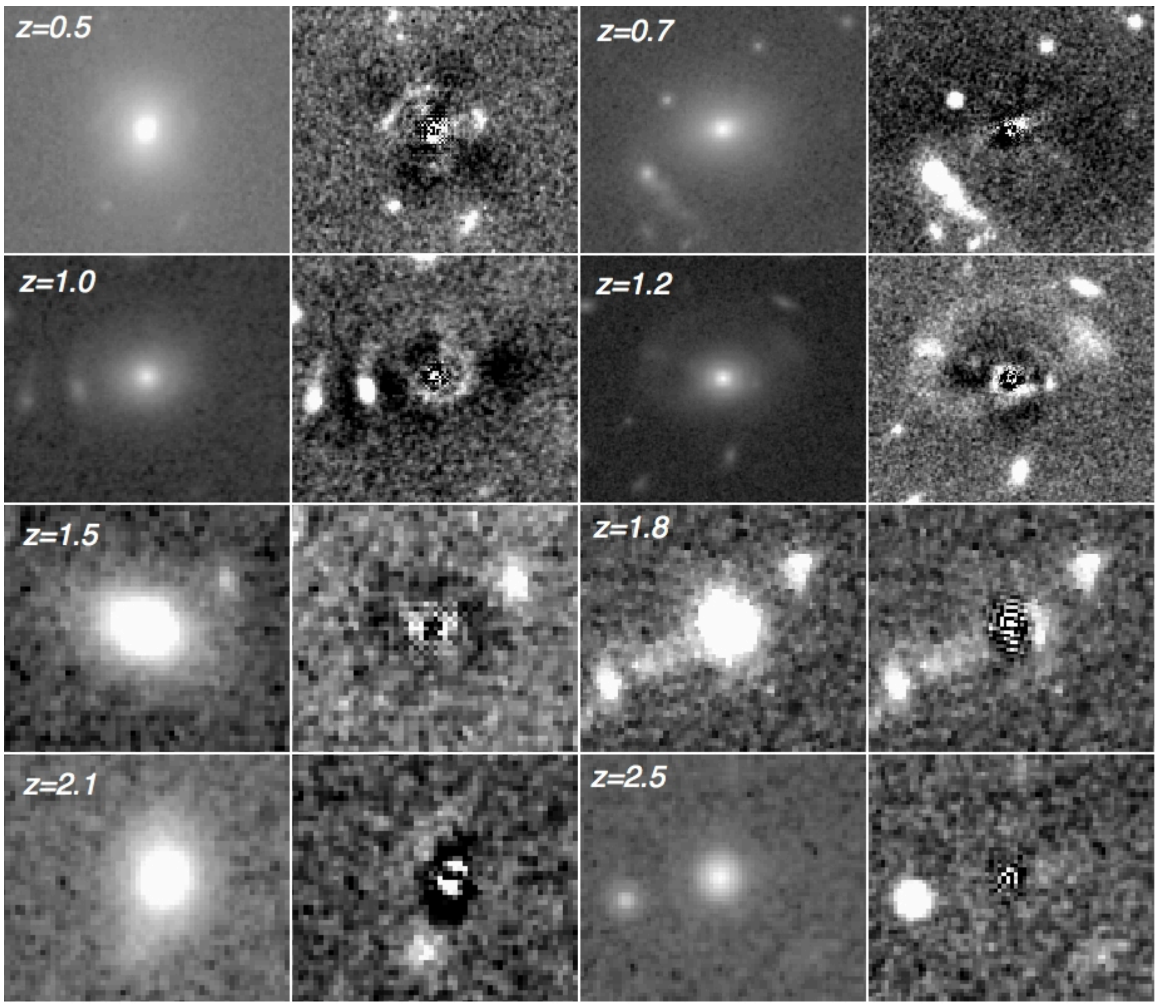

Figure 4.10: Examples of galaxies which either (potentially) experienced mergers or have nearby neighbors, at different redshifts. Galaxies and their accompanied residual images show that after the removal of bulge+disk model from the galaxy image, a more reliable visual inspection of neighboring and potentially merging objects can be achieved.

et al. 2011). This has been contributed to the disks being dynamically hot at higher redshifts (Genzel et al. 2006; Law et al. 2007; Law et al. 2009).

Figure 4.11 shows how galaxy residuals of bulge+disk models can reveal the spiral structures which could be harder to detect otherwise (see also Bruce et al. (2012) Figures C1 and C3). Table 5 shows the fraction of star-forming galaxies which contain a spiral structure that can be detected visually. There is almost no quiescent galaxy with a visually detectable spiral structure. A considerable fraction of star-forming galaxies at $0.5 < z < 1.5$ have spiral structures (mainly spiral arms). Even about 20% of star forming galaxies at $1.5 < z < 2.0$ have this property. Spiral arms are formed in galaxies with disks that are sufficiently gravitationally dominated which in turn is closely related to the Toomre parameter Q (Toomre 1964) for stars and/or gas (see Dobbs & Baba 2014 for a review). The existence of spiral arms at higher redshifts provides further evidence for the existence of stellar disks at those epochs.

The fraction of star-forming galaxies with spiral structures drops at the lowest redshift bin. This drop may not be reliable for two reasons. First, the star-forming sample size at $0.5 < z < 1.0$ is very small (only 10) and therefore the sample proportions are not statistically significant. Second, the H band images of star-forming galaxies at $0.5 < z < 1.0$ are missing the bluer parts of the galaxy flux. However, considering the high fraction of galaxies with merger signatures at $0.5 < z < 1.5$, at least some of this drop may be real.

Secular evolutions are believed to be triggered and maintained by bars and spiral structures (Kormendy & Kennicutt 2004). At least after $z = 1.5$, secular evolutions could play a part in the growth of the star-forming galaxies bulges. However, considering the fact that the majority of these massive galaxies are destined to turn into local massive ellipticals, the possible secular evolution may be in effect for only a few Gyr.

An edge-on view of galaxies can reveal another indisputable signature of prominent stellar disks. Figure 4.12 confirms that at least a fraction of massive galaxies at higher redshifts have a thin disk. This further confirms the existence of cold disks among the massive galaxies at higher redshifts. Table 5 shows that the fraction of edge-on galaxies at $z < 1.0$ drops considerably, while it is about 10% at other redshift bins.

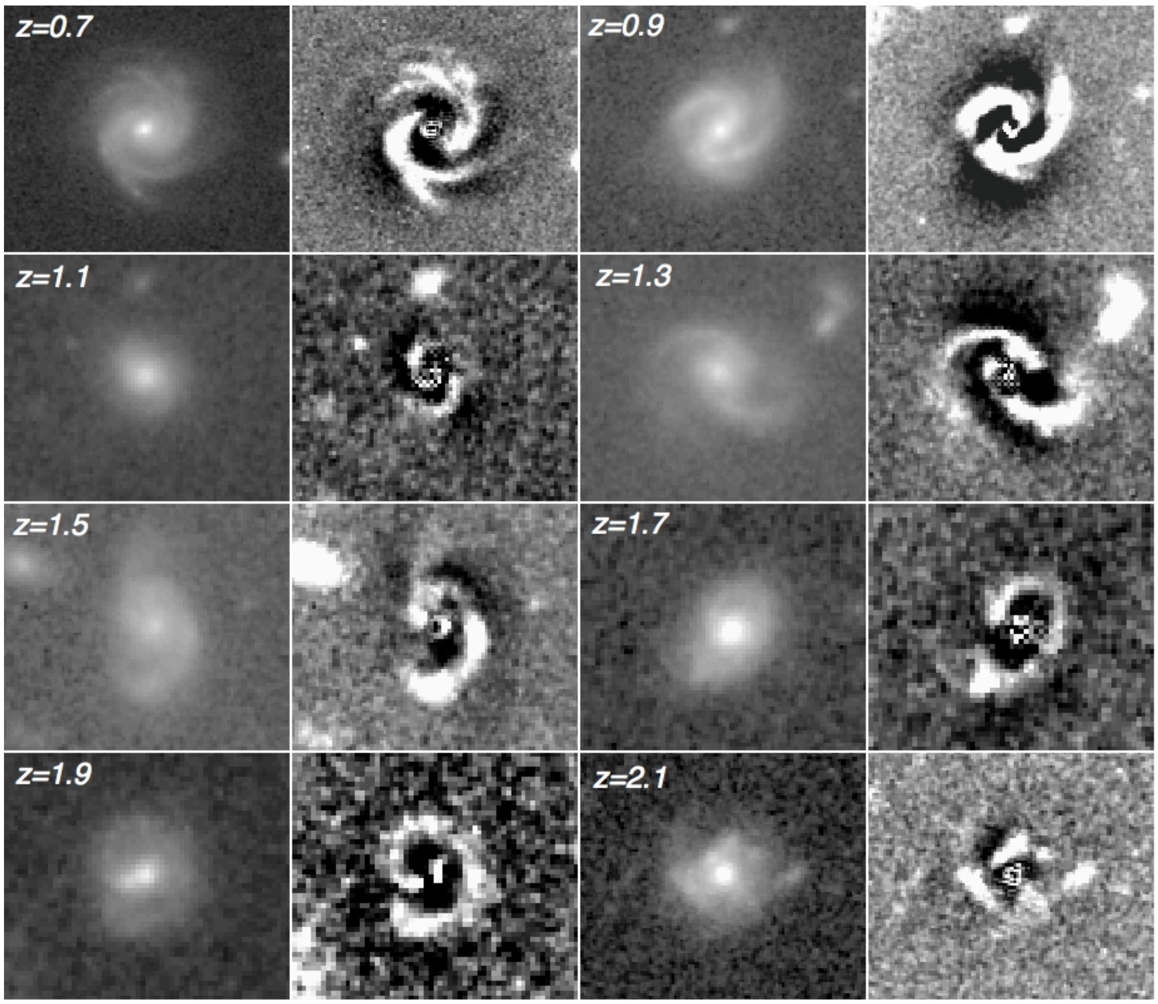

Figure 4.11: Examples of galaxies which seemingly have spiral structures, at different redshifts. Galaxies and their accompanied residual images show that after the removal of bulge+disk model from the galaxy image can reveal the spiral structures which could be harder to detect otherwise.

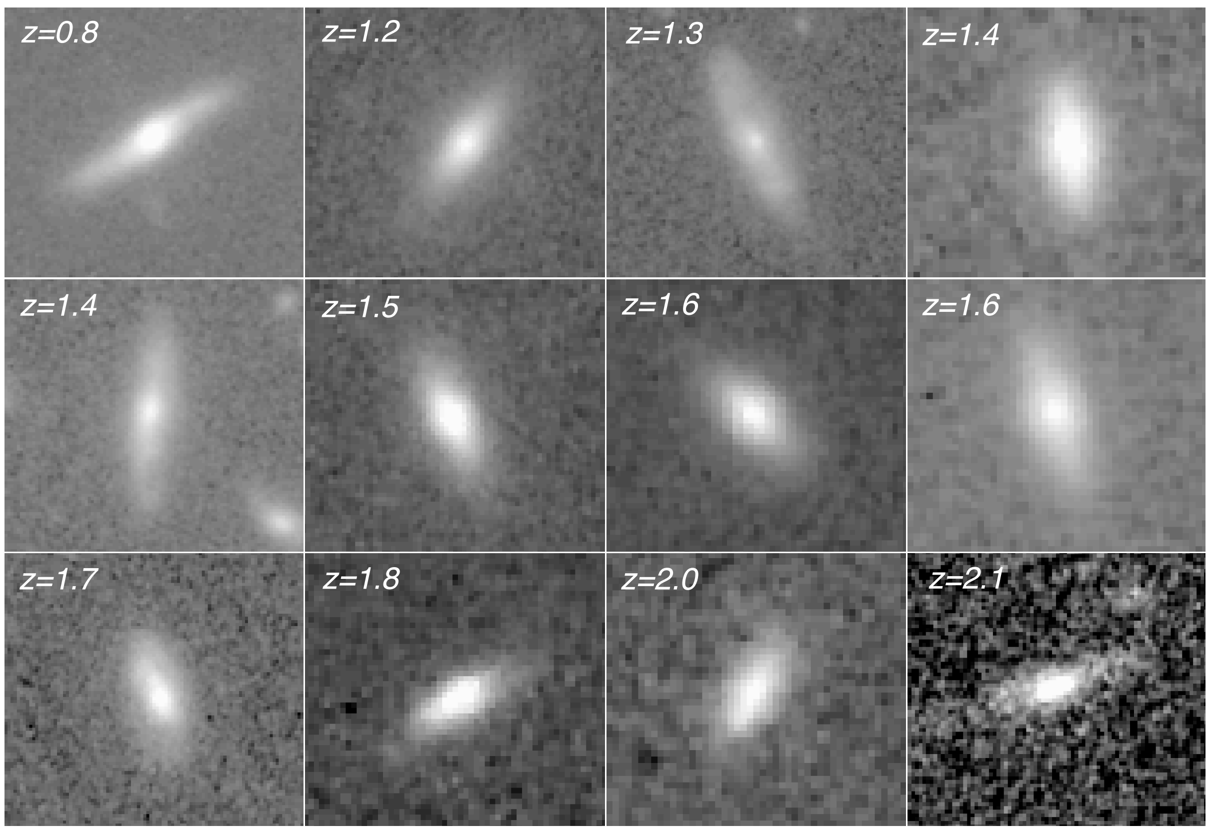

Figure 4.12: Examples of massive galaxies with a thin disk at different redshifts.

The prevalence of prominent stellar disks at higher redshifts raises the possibility that some of these bulge+disk massive galaxies may have survived in the last 10 billion years and are present in the local universe. Wellons et al. (2015), using Illustris (Vogelsberger et al. 2014; Genel et al. 2014) cosmological hydrodynamical simulation, trace the evolution of 35 massive compact galaxies from $z = 2$. Interestingly, they find that about 30% of their galaxies survive undisturbed, while the rest are either have experienced the inside-out growth or have been destroyed via major mergers.

4.6 Summary

The discovery of massive compact galaxies at high redshift, specially red nuggets, has opened a new door for examining our understanding of galaxy formation and evolution. These massive galaxies have major differences with their local counterparts (i.e., massive ellipticals). They are found to be compact and possess a stellar disk, which in turn, needs to be destroyed. We quantify the evolution of these massive galaxies between $0.5 < z < 2.5$, by performing comprehensive morphological analysis. This includes single Sérsic fittings and bulge+disk decompositions using GALFIT. We use CANDELS images as they have high resolution, high 5σ limiting magnitudes, and coverage of the five most studied fields (COSMOS, UDS, EGS, GOODS-South and GOODS-North). A total of about 250 massive galaxies are selected using a fixed number density selection. UVJ color-color diagram is employed for separating the quiescent from the star-forming galaxies. Diagnostic plots are employed to examine the goodness of the fits, which led to more than 240 galaxies robustly modeled.

We conclude:

- The fraction of quiescent massive galaxies is higher at lower redshifts.
- Both star-forming and quiescent galaxies have increased their sizes significantly within $0 < z < 2.5$. The size increase has taken place via the inside-out growth.

- The global Sérsic index of quiescent galaxies has increased over time (from $n \approx 2.5$ to $n > 4$), while for star-forming galaxies, it stays about the same ($n \approx 2.5$).

- Based on their B/T, both star-forming and quiescent galaxies have a significant stellar disk at higher redshifts. By $z \approx 0.5$, massive quiescent galaxies (with $B/T \approx 0.8$) begin to resemble the local elliptical galaxies. Star-forming galaxies have a lower median B/T at each redshift bin.

- A considerable fraction of our sample have visually detectable spiral structures or a thin disk, which further confirms that high-z massive galaxies have a prominent stellar disk.

- While minor dry mergers are the favored candidates for explaining the inside-out growth, major mergers are needed for destroying the stellar disk between redshift 2.5 and the present time.

- Bulges of star-forming and quiescent galaxies follow different evolutionary trajectories while their disks evolve similarly. The size increase of quiescent galaxies bulges is more significant and their n and axial ratios are, on average, higher than their star-forming counterparts.

Bibliography

Baldry, I. K., Driver, S. P., Loveday, J., et al. 2012, MNRAS, 421, 621

Barden, M., Rix, H.-W., Somerville, R. S., et al. 2005, ApJ, 635, 959

Barnes, J. E. 2002, MNRAS, 333, 481

Barnes, J. E., & Hernquist, L. 1992, Annual Reviews of Astronomy and Astrophysics, 30, 705

Barro, G., Faber, S. M., Pérez-González, P. G., et al. 2013, ApJ, 765, 104

Bell, E. F., Wolf, C., Meisenheimer, K., et al. 2004, ApJ, 608, 752

Bernardi, M., Roche, N., Shankar, F., & Sheth, R. K. 2011, MNRAS, 412, L6

Bezanson, R., van Dokkum, P. G., Tal, T., et al. 2009, ApJ, 697, 1290

Blanton, M. R., Hogg, D. W., Bahcall, N. A., et al. 2003, ApJ, 592, 819

Bournaud, F., & Elmegreen, B. G. 2009, ApJl, 694, L158

Bournaud, F., Elmegreen, B. G., & Elmegreen, D. M. 2007, ApJ, 670, 237

Brammer, G. B., van Dokkum, P. G., & Coppi, P. 2008, ApJ, 686, 1503

Brammer, G. B., Whitaker, K. E., van Dokkum, P. G., et al. 2011, ApJ, 739, 24

Bruce, V. A., Dunlop, J. S., Cirasuolo, M., et al. 2012, MNRAS, 427, 1666

Bruce, V. A., Dunlop, J. S., McLure, R. J., et al. 2014, MNRAS, 444, 1660

Buitrago, F., Trujillo, I., Conselice, C. J., et al. 2008, ApJl, 687, L61

Carilli, C. L., & Walter, F. 2013, Annual Reviews of Astronomy and Astrophysics, 51, 105

Cassata, P., Giavalisco, M., Guo, Y., et al. 2010, ApJl, 714, L79

Cassata, P., Giavalisco, M., Guo, Y., et al. 2011, ApJ, 743, 96

Chang, Y.-Y., van der Wel, A., Rix, H.-W., et al. 2013, ApJ, 762, 83

Chapman, S. C., Ivison, R. J., Roseboom, I. G., et al. 2010, MNRAS, 409, L13

Cimatti, A., Cassata, P., Pozzetti, L., et al. 2008, Astronomy and Astrophysics, 482, 21

Ciotti, L. 1991, Astronomy and Astrophysics, 249, 99

Conselice, C. J., Blackburne, J. A., & Papovich, C. 2005, ApJ, 620, 564

Conselice, C. J., Bluck, A. F. L., Ravindranath, S., et al. 2011, MNRAS, 417, 2770

Coppin, K. E. K., Swinbank, A. M., Neri, R., et al. 2008, MNRAS, 389, 45

Daddi, E., Renzini, A., Pirzkal, N., et al. 2005, ApJl, 626, 680

Dahlen, T., Mobasher, B., Faber, S. M., et al. 2013, ApJ, 775, 93

Damjanov, I., McCarthy, P. J., Abraham, R. G., et al. 2009, ApJ, 695, 101

Davari, R., Ho, L. C., Peng, C. Y., & Huang, S. 2014, ApJ, 787, 69

Davis, M., Guhathakurta, P., Konidaris, N. P., et al. 2007, ApJl, 660, L1

de Vaucouleurs, G. 1948, Annales d'Astrophysique, 11, 247

Dobbs, C., & Baba, J. 2014, Publications of the Astronomical Society of Australia, 31, 35

Driver, S. P., GAMA Team, Baldry, I. K., et al. 2009, in IAU Symposium, Vol. 254, IAU Symposium, ed. J. Andersen, Nordströara, B. m, & J. Bland-Hawthorn, 469–474

Fathi, K., & Peletier, R. F. 2003, Astronomy and Astrophysics, 407, 61

Fisher, D. B., & Drory, N. 2008, The Astronomical Journal, 136, 773

Franx, M., van Dokkum, P. G., Schreiber, N. M. F., et al. 2008, ApJ, 688, 770

Frayer, D. T., Ivison, R. J., Smail, I., Yun, M. S., & Armus, L. 1999, The Astronomical Journal, 118, 139

Freeman, K. C. 1970, ApJ, 160, 811

Genel, S., Vogelsberger, M., Springel, V., et al. 2014, MNRAS, 445, 175

Genzel, R., Tacconi, L. J., Eisenhauer, F., et al. 2006, Nature, 442, 786

Giavalisco, M., Ferguson, H. C., Koekemoer, A. M., et al. 2004, ApJl, 600, L93

Graham, A. W., & Worley, C. C. 2008, MNRAS, 388, 1708

Greve, T. R., Bertoldi, F., Smail, I., et al. 2005, MNRAS, 359, 1165

Grogin, N. A., Kocevski, D. D., Faber, S. M., et al. 2011, ApJl Supp., 197, 35

Hilz, M., Naab, T., & Ostriker, J. P. 2013, MNRAS, 429, 2924

Hogg, D. W., Blanton, M. R., Brinchmann, J., et al. 2004, ApJl, 601, L29

Hopkins, P. F., Bundy, K., Murray, N., et al. 2009, MNRAS, 398, 898

Hopkins, P. F., Somerville, R. S., Hernquist, L., et al. 2006, ApJ, 652, 864

Hopkins, P. F., Bundy, K., Croton, D., et al. 2010, ApJ, 715, 202

Huang, S., Ho, L. C., Peng, C. Y., Li, Z.-Y., & Barth, A. J. 2013, ApJl, 768, L28

Ichikawa, T., Kajisawa, M., & Akhlaghi, M. 2012, MNRAS, 422, 1014

Ivison, R. J., Swinbank, A. M., Smail, I., et al. 2013, ApJ, 772, 137

Janowiecki, S., Mihos, J. C., Harding, P., et al. 2010, ApJ, 715, 972

Jedrzejewski, R. I. 1987, MNRAS, 226, 747

Kneib, J.-P., Neri, R., Smail, I., et al. 2005, Astronomy and Astrophysics, 434, 819

Koekemoer, A. M., Faber, S. M., Ferguson, H. C., et al. 2011, ApJl Supp., 197, 36

Kormendy, J., & Kennicutt, Jr., R. C. 2004, Annual Reviews of Astronomy and Astrophysics, 42, 603

Kovács, A., Chapman, S. C., Dowell, C. D., et al. 2006, ApJ, 650, 592

Krist, J. E., Hook, R. N., & Stoehr, F. 2011, in Society of Photo-Optical Instrumentation Engineers (SPIE) Conference Series, Vol. 8127

Labbé, I., Bouwens, R., Illingworth, G. D., & Franx, M. 2006, ApJl, 649, L67

Laidler, V. G., Papovich, C., Grogin, N. A., et al. 2007, Publications of the Astronomical Society of the Pacific, 119, 1325

Lang, P., Wuyts, S., Somerville, R. S., et al. 2014, ApJ, 788, 11

Law, D. R., Steidel, C. C., Erb, D. K., et al. 2007, ApJ, 669, 929

Law, D. R., Steidel, C. C., Erb, D. K., et al. 2009, ApJ, 697, 2057

Lawrence, A., Warren, S. J., Almaini, O., et al. 2007, MNRAS, 379, 1599

Leja, J., van Dokkum, P., & Franx, M. 2013, ApJ, 766, 33

Lemson, G., & Virgo Consortium, t. 2006, ArXiv Astrophysics e-prints, astro-ph/0608019

Lintott, C., Schawinski, K., Bamford, S., et al. 2011, MNRAS, 410, 166

Liske, J., Baldry, I. K., Driver, S. P., et al. 2015, MNRAS, 452, 2087

Magnelli, B., Lutz, D., Berta, S., et al. 2010a, Astronomy and Astrophysics, 518, L28

Magnelli, B., Lutz, D., Berta, S., et al. 2010b, Astronomy and Astrophysics, 518, L28

Mancini, C., Daddi, E., Renzini, A., et al. 2010, MNRAS, 401, 933

McIntosh, D. H., Bell, E. F., Rix, H.-W., et al. 2005, ApJ, 632, 191

Michałowski, M., Hjorth, J., & Watson, D. 2010, Astronomy and Astrophysics, 514, A67

Michałowski, M. J., Dunlop, J. S., Cirasuolo, M., et al. 2012, Astronomy and Astrophysics, 541, A85

Mobasher, B., Dahlen, T., Ferguson, H. C., et al. 2015, ApJ, 808, 101

Morishita, T., Ichikawa, T., & Kajisawa, M. 2014, ApJ, 785, 18

Mosleh, M., Williams, R. J., & Franx, M. 2013, ApJ, 777, 117

Mundy, C. J., Conselice, C. J., & Ownsworth, J. R. 2015, MNRAS, 450, 3696

Muzzin, A., Marchesini, D., Stefanon, M., et al. 2013, ApJl Supp., 206, 8

Naab, T., Johansson, P. H., & Ostriker, J. P. 2009, ApJl, 699, L178

Naab, T., Johansson, P. H., Ostriker, J. P., & Efstathiou, G. 2007, ApJ, 658, 710

Naoz, S., & Barkana, R. 2007, MNRAS, 377, 667

Neri, R., Genzel, R., Ivison, R. J., et al. 2003, ApJl, 597, L113

Newman, A. B., Ellis, R. S., Bundy, K., & Treu, T. 2012, ApJ, 746, 162

Oser, L., Naab, T., Ostriker, J. P., & Johansson, P. H. 2012, ApJ, 744, 63

Papovich, C., Finkelstein, S. L., Ferguson, H. C., Lotz, J. M., & Giavalisco, M. 2011, MNRAS, 412, 1123

Patel, S. G., van Dokkum, P. G., Franx, M., et al. 2013, ApJ, 766, 15

Peng, C. Y., Ho, L. C., Impey, C. D., & Rix, H.-W. 2010, The Astronomical Journal, 139, 2097

Poggianti, B. M., Calvi, R., Bindoni, D., et al. 2013, ApJ, 762, 77

Ravindranath, S., Ferguson, H. C., Conselice, C., et al. 2004, ApJl, 604, L9

Riechers, D. A., Carilli, L. C., Walter, F., et al. 2011, ApJl, 733, L11

Robertson, B., Bullock, J. S., Cox, T. J., et al. 2006, ApJ, 645, 986

Robertson, B. E., & Bullock, J. S. 2008, ApJl, 685, L27

Sanders, D. B., Soifer, B. T., Elias, J. H., Neugebauer, G., & Matthews, K. 1988, ApJl, 328, L35

Santini, P., Ferguson, H. C., Fontana, A., et al. 2015, ApJ, 801, 97

Saracco, P., Longhetti, M., & Gargiulo, A. 2010, MNRAS, 408, L21

Schulz, J., Fritze-v. Alvensleben, U., & Fricke, K. J. 2003, Astronomy and Astrophysics, 398, 89

Scoville, N., Abraham, R. G., Aussel, H., et al. 2007a, ApJl Supp., 172, 38

Scoville, N., Aussel, H., Brusa, M., et al. 2007b, ApJl Supp., 172, 1

Shen, S., Mo, H. J., White, S. D. M., et al. 2003, MNRAS, 343, 978

Sheth, K., Blain, A. W., Kneib, J.-P., et al. 2004, ApJl, 614, L5

Skelton, R. E., Whitaker, K. E., Momcheva, I. G., et al. 2014, ApJl Supp., 214, 24

Springel, V., & Hernquist, L. 2005, ApJl, 622, L9

Springel, V., White, S. D. M., Jenkins, A., et al. 2005, Nature, 435, 629

Szomoru, D., Franx, M., Bouwens, R. J., et al. 2011, ApJl, 735, L22

Szomoru, D., Franx, M., & van Dokkum, P. G. 2012, ApJ, 749, 121

Tacconi, L. J., Neri, R., Chapman, S. C., et al. 2006, ApJ, 640, 228

Tal, T., van Dokkum, P. G., Nelan, J., & Bezanson, R. 2009, The Astronomical Journal, 138, 1417

Targett, T. A., Dunlop, J. S., Cirasuolo, M., et al. 2013, MNRAS, 432, 2012

Taylor, E. N., Franx, M., Glazebrook, K., et al. 2010, ApJ, 720, 723

Thomas, D., Maraston, C., Bender, R., & Mendes de Oliveira, C. 2005, ApJ, 621, 673

Toft, S., van Dokkum, P., Franx, M., et al. 2007, ApJ, 671, 285

Toft, S., Smolčić, V., Magnelli, B., et al. 2014, ApJ, 782, 68

Toomre, A. 1964, ApJ, 139, 1217

Toomre, A. 1977, Annual Reviews of Astronomy and Astrophysics, 15, 437

Trujillo, I., Cenarro, A. J., de Lorenzo-Cáceres, A., et al. 2009, ApJl, 692, L118

Trujillo, I., Conselice, C. J., Bundy, K., et al. 2007, MNRAS, 382, 109

Ueda, J., Iono, D., Yun, M. S., et al. 2014, ApJl Supp., 214, 1

Valentinuzzi, T., Fritz, J., Poggianti, B. M., et al. 2010, ApJ, 712, 226

van der Wel, A., Holden, B. P., Zirm, A. W., et al. 2008, ApJ, 688, 48

van der Wel, A., Rix, H.-W., Holden, B. P., Bell, E. F., & Robaina, A. R. 2009, ApJl, 706, L120

van der Wel, A., Rix, H.-W., Wuyts, S., et al. 2011, ApJ, 730, 38

van der Wel, A., Bell, E. F., Häussler, B., et al. 2012, ApJl Supp., 203, 24 van Dokkum, P. G. 2005, The Astronomical Journal, 130, 2647

van Dokkum, P. G., Franx, M., Kriek, M., et al. 2008, ApJl, 677, L5

van Dokkum, P. G., Whitaker, K. E., Brammer, G., et al. 2010, ApJ, 709, 1018

van Dokkum, P. G., Nelson, E. J., Franx, M., et al. 2015, ArXiv e-prints, arXiv:1506.03085

Vogelsberger, M., Genel, S., Springel, V., et al. 2014, MNRAS, 444, 1518

Welker, C., Dubois, Y., Devriendt, J., et al. 2015, ArXiv e-prints, arXiv:1502.05053

Wellons, S., Torrey, P., Ma, C.-P., et al. 2015, MNRAS, 449, 361

Whitaker, K. E., Labbé, I., van Dokkum, P. G., et al. 2011, ApJ, 735, 86

Willett, K. W., Lintott, C. J., Bamford, S. P., et al. 2013, MNRAS, 435, 2835

Williams, C. C., Giavalisco, M., Cassata, P., et al. 2014, ApJ, 780, 1

Williams, R. J., Quadri, R. F., Franx, M., van Dokkum, P., & Labbé, I. 2009, ApJ, 691, 1879

Wuyts, S., Cox, T. J., Hayward, C. C., et al. 2010, ApJ, 722, 1666

Wuyts, S., Labbé, I., Franx, M., et al. 2007, ApJ, 655, 51

Zirm, A. W., van der Wel, A., Franx, M., et al. 2007, ApJ, 656, 66